FCT
Fundação para a Ciência e a Tecnologia
MINISTÉRIO DA EDUCAÇÃO E CIÊNCIA

POPH
QUALIFICAR É CRESCER.

QREN
QUADRO DE REFERÊNCIA ESTRATÉGICO NACIONAL
PORTUGAL 2007.2013

Governo da República Portuguesa

UNIÃO EUROPEIA
Fundo Social Europeu

Bond behaviour of NSM FRP systems in concrete
Mário Rui Freitas Coelho

UMinho | 2016

Universidade do Minho
Escola de Engenharia

Mário Rui Freitas Coelho

Bond behaviour of NSM FRP systems in concrete

October 2016

Universidade do Minho
Escola de Engenharia

Mário Rui Freitas Coelho

Bond behaviour of NSM FRP systems in concrete

Doctorate Thesis in Civil Engineering

Work conducted under supervision of
Professor Doctor José Manuel de Sena Cruz
Professor Doctor Luís Armando Canhoto Neves

October 2016

DECLARATION

Name	Mário Rui Freitas Coelho
E-mail	mcoelho@civil.uminho.pt
Doctoral thesis title	Bond behaviour of NSM FRP systems in concrete
Supervisors	José Manuel de Sena Cruz
	Luís Armando Canhoto Neves
Year of conclusion	2016
Field of knowledge	Civil Engineering

University of Minho, October 2016

STATEMENT OF INTEGRITY

I hereby declare having conducted my thesis with integrity. I have not used plagiarism or any form of falsification of results in the process of the thesis elaboration. I further declare that I have fully acknowledge the Code of Ethical Conduct of the University of Minho.

University of Minho, October 2016

To Filipa and Júlia

Acknowledgements

If a PhD was a movie, mine would certainly be one of James Bond's saga. Not only because of the obvious Bond name issue but rather due its nature. Let's see: I play 007 (just for comparison purposes), there is a sophisticated supporting team (I got not one, but two Q – my supervisors), the action takes place in different countries (Portugal, Argentina and England), there are always some kind of informers/friends/helpers which make the mission easier (Antonio Caggiano, António Matos, Joaquim Tinoco, Marta Pereira, Paulo Cortez, Pedro Fernandes, Ricardo Cruz, Tiago Miranda), unfortunately the mission never ends without losses to regret (Tiago Teixeira) and finally, there is always a pretty Bond girl (again, I was lucky enough to got two: my lovely wife and daughter) which makes it all worth it.

The names referred above correspond to those that directly contributed to this thesis success. Many others made an indirect contribution which must also be aknowledge. My mission would not have been successfully completed without the contribution of you all. Thank you all very much!

Finally, I should also acknowledge the financial support provided by FEDER funds through the Operational Program for Competitiveness Factors – COMPETE and by national funds through Portuguese Foundation for Science and Technology – FCT within the scope of projects CutInDur FCOMP-01-0124-FEDER-014811 and POCI-01-0145-FEDER-007633, and also the PhD grant SFRH/BD/87443/2012. The mobility grant provided by the "EnCoRe" Project (FP7-PEOPLE-2011-IRSES nº 295283; www.encore-fp7.unisa.it) funded by the European Union within the Seventh Framework Programme, is also gratefully acknowledged.

This page was left blank intentionally.

Abstract

In the context of strengthening concrete structures, the Near-Surface Mounted (NSM) technique using Fibre Reinforced Polymers (FRP) has been shown as a sound solution. This technique consists on inserting the FRP into grooves opened on the concrete elements to be strengthened. Epoxy adhesives are the most commonly used binders. The crucial aspect regarding the NSM FRP technique is related with the way the stresses are transferred from the existing concrete to the added FRP, i.e. the bond behaviour. This thesis principal objective was to add a contribution to the existing knowledge on the bond behaviour of NSM FRP systems in concrete.

Considering that the bond behaviour is studied through bond tests, those were the basis of the entire research presented in this document. Hence, a bibliographic survey was conducted in order to obtain a database with the majority of the existing experimental works on bond tests. Whenever available there were also collected the analytical bond laws and the numerical strategies adopted by the authors to simulate their tests. With all this information, three different tasks were defined, each addressing one important and complementary aspect regarding the bond behaviour of NSM FRP systems in concrete: an analytical, an experimental and a numerical task.

The analytical task was composed by the following three steps: (i) assess the accuracy of the existing bond laws, calibrate them and/or propose improvements; (ii) introduce data mining algorithms as alternative bond laws; (iii) calibrate the necessary safety factors in order to allow using the bond laws in the design of NSM FRP systems in concrete.

In the experimental task, a campaign of direct pullout tests was defined in order to allow, in the near future, the establishment of a standard direct pullout test. In addition, parameters which were not yet used for studying the bond behaviour were included in

this experimental campaign.

Finally, the numerical task consisted on the development of an interface constitutive model based on the plasticity theory to allow 3D numerical simulations of NSM FRP systems. This constitutive model was implemented in FEMIX software and validated using pullout test's results.

Resumo

No âmbito do reforço de estruturas de betão, a técnica de NSM com recurso a polímeros reforçados com fibras (FRP) tem-se revelado uma boa solução. Esta técnica consiste em inserir FRP em entalhes abertos nos elementos de betão a reforçar. Adesivos epóxi são os ligantes mais frequentemente utilizados. O aspeto crucial da técnica NSM FRP está relacionado com a forma como as tensões são transferidas do betão existente para o FRP adicionado, i.e., o comportamento da ligação. O principal objetivo desta tese foi contribuir para o conhecimento sobre o comportamento da ligação em sistemas NSM FRP no betão.

Considerando que o comportamento da ligação é estudado através de ensaios de arranque, estes foram a base de toda a pesquisa apresentada neste documento. Assim, foi realizada uma pesquisa bibliográfica de modo a obter uma base de dados com a maioria dos trabalhos experimentais existentes sobre ensaios de arranque. Sempre que existissem, também foram coletadas as leis analíticas de aderência e as estratégicas numéricas adotadas pelos autores para simular os seus ensaios. Com toda esta informação, três tarefas diferentes foram definidas, cada uma abordando um aspeto importante e complementar sobre o comportamento da ligação de sistemas NSM FRP no betão: uma tarefa analítica, uma experimental e uma numérica.

A tarefa analítica era composta pelas seguintes três etapas: (i) avaliar a precisão das leis de aderência existentes, calibrá-las e/ou propor melhorias; (ii) introduzir os algoritmos de data mining como leis de aderência alternativas; (iii) calibrar os fatores de segurança necessários de modo a permitir o uso das leis de aderência no dimensionamento de sistemas NSM FRP no betão.

Na tarefa experimental, foi definida uma campanha de ensaios de arranque de modo a permitir, num futuro próximo, o estabelecimento de um ensaio de arranque direto

standard. Adicionalmente, foram adicionados nesta campanha experimental parâmetros que ainda não foram utilizados no estudo do comportamento da ligação.

Finalmente, a tarefa numérica consistiu no desenvolvimento de uma lei constitutiva de interface baseada na teoria da plasticidade para permitir simulações numéricas 3D de sistemas NSM FRP. Esta lei constitutiva foi implementada no software FEMIX e validada usando resultados de ensaios de arranque.

Contents

Acknowledgements **vii**

Abstract **ix**

Resumo **xi**

List of Figures **xvii**

List of Tables **xix**

Symbols **xxi**

Acronyms **xxiii**

1 Introduction **1**

1.1 Motivation 3

1.2 Objectives and research methodology 4

1.3 Outline of the thesis 5

2 A review on the bond behaviour of NSM FRP systems in concrete **7**

2.1 Failure modes at structural level 7

2.2 Failure modes at mesoscale 9

2.3 NSM bond tests 10

2.4 NSM guidelines 11

2.4.1 American Concrete Institute formulation 13

2.4.2 Standards Australia formulation . . . 13
2.4.3 Construction details . . . 14
2.5 Databases of bond tests . . . 15
2.5.1 Web-based tool . . . 16
2.5.2 Analysis of the databases . . . 18
2.5.2.1 Bonded length . . . 19
2.5.2.2 FRP fibre type and external surface . . . 19
2.5.2.3 Groove surface . . . 20
2.5.2.4 FRP axial stiffness . . . 20
2.5.2.5 FRP cross-section geometry . . . 20
2.5.2.6 Groove's geometry . . . 21
2.5.2.7 Shape ratio . . . 22
2.5.2.8 Cover of the FRP . . . 22
2.5.2.9 Concrete strength . . . 22
2.5.2.10 Bond test type . . . 23
2.5.2.11 Failure modes . . . 25
2.6 Unsolved issues . . . 27

3 Bond strength of NSM FRP systems in concrete: mechanical models 29
3.1 Analytical mechanical models analysis . . . 29
3.1.1 ACI guideline . . . 30
3.1.2 SA guideline . . . 33
3.2 Data mining mechanical models analysis . . . 36
3.2.1 Data mining models . . . 36
3.2.1.1 Artificial Neural Networks . . . 37
3.2.1.2 Support Vector Machines . . . 39
3.2.1.3 Rminer tool . . . 40
3.2.2 Data mining analyses . . . 41
3.2.2.1 Results and analysis . . . 42
3.2.2.2 Using data mining models . . . 46
3.3 Conclusions . . . 50

4 Bond strength of NSM FRP systems in concrete: design models 55
4.1 Partial safety factors method . . . 56
4.2 Data and models . . . 58
4.2.1 Material probabilistic models . . . 59
4.2.2 Probabilistic uncertainty for mechanical bond strength models . . . 60

4.3 Safety factors calibration . . . 62
4.4 Results analysis . . . 64
4.4.1 Specimens separated by guidelines' failure mode detection . . . 65
4.4.2 Specimens separated by experimental failure mode . . . 66
4.4.3 Bond strength according to the theoretical resistance models . . . 67
4.4.4 Partial safety factor for CFRP (γ_f) . . . 68
4.4.5 ACI debonding safety factor (τ_d) . . . 69
4.4.6 SA global safety factors (η_c and η_b) . . . 69
4.4.7 Bond strength in the theoretical resistance models with reliability parameters . . . 70
4.4.8 Probability models adopted for CFRP parameters . . . 71
4.4.9 Influence of the mechanical model . . . 72
4.5 Reliability based design with soft computing models . . . 73
4.6 Conclusions . . . 74

5 Experimental program of bond with NSM FRP systems in concrete 77
5.1 Tests configurations and specimen's preparation . . . 80
5.2 Material characterization . . . 83
5.3 Results obtained . . . 84
5.4 Results analysis . . . 90
5.4.1 Influence of test type . . . 90
5.4.2 Influence of casting direction . . . 95
5.4.3 Influence of initial stress state level . . . 96
5.4.4 Influence of test velocity . . . 96
5.5 Conclusions . . . 97

6 Fracture-based interface model for NSM FRP systems in concrete 99
6.1 Formulation of the interface constitutive model . . . 101
6.2 Model validation: simulation details . . . 108
6.2.1 FEM model with interface L2D elements . . . 110
6.2.2 FEM model with interface S elements . . . 110
6.2.3 Parameters of each interface constitutive model . . . 111
6.3 Model validation: numerical results . . . 113
6.3.1 Experimental *versus* numerical results . . . 113
6.3.2 CM II *versus* CM I/II results . . . 115
6.3.3 L2D *versus* S FEM models results . . . 117
6.3.4 Experimental *versus* numerical FRP axial strain . . . 119

6.4 Conclusions 120

7 Conclusions and future developments **121**
7.1 Main conclusions 122
7.1.1 Experimental component 122
7.1.2 Analytical component 123
7.1.3 Numerical component 124
7.2 Future developments 125
7.2.1 Experimental component 126
7.2.2 Analytical component 126
7.2.3 Numerical component 127

Bibliography **129**

A FRPBonData website **139**

B Interface constitutive model detailed formulation **145**
B.1 Constitutive model II 145
B.2 Constitutive model I/II_2D 145
B.3 Constitutive model I/II_3D 146

List of Figures

1.1 Amount of publications on the NSM technique 3
1.2 Thesis workflow 5

2.1 Principal debonding failure modes in flexure 9
2.2 Four possible failure modes associated with debonding 9
2.3 Bond-slip laws for NSM FRP systems 12
2.4 Website homepage 17
2.5 Influence of EA_f in ε_{fmax} 21
2.6 Summary of DPT configurations used in the works collected 24
2.7 Summary of failure modes for the specimens in DPT database 27

3.1 Results for the analyses with ACI standard in DPT database 31
3.2 Results for the analyses with ACI standard in BPT database 32
3.3 Results for the analyses with SA standard in DPT database 34
3.4 Results for the analyses with SA standard in BPT database 35
3.5 Example of Artificial Neural Networks 38
3.6 Example of Support Vector Machines 39
3.7 Variables involved in the Data Mining analyses 43
3.8 Relative importance of each input variable in the analyses Type B 47
3.9 Maximum pullout force prediction calculated in the website 48
3.10 Results for the analyses with *fit* function in both databases 50
3.11 Variation of *fit* results with the bonded length in both databases 51
3.12 VEC curves for L_b using both databases 52

4.1 FORM design point and reliability index in the normalized space 56
4.2 PDF of limit state theoretical resistance functions errors 61
4.3 Failure modes obtained experimentally and using the guidelines 65
4.4 Pullout force obtained experimentally and using the guidelines 66
4.5 Histograms of the guidelines predictions errors 68
4.6 Histograms of data mining models predictions errors 75

5.1 Geometry and test setup of direct pullout tests 81
5.2 Preparation of the DPT specimens 82
5.3 Identification of the strengthened sides in each cube 83
5.4 DPT pullout force *versus* loaded end slip 85
5.5 DPT pullout force *versus* loaded end slip (cont.) 86
5.6 Failure modes obtained in the direct pullout tests 88
5.7 Location of some series specimens in the cubes 89
5.8 Pullout force *versus* loaded end slip obtained in DPT tests 91
5.9 FEM simulations conducted to validate the experimental results 93
5.10 Results of the numerical simulations to validate the LVDT readings 94

6.1 Fracture modes associated with NSM FRP systems in concrete 102
6.2 Interface elements available in FEMIX 103
6.3 Local return-mapping algorithm 105
6.4 CaReCo direct pullout test details 111
6.5 GlRoTe direct pullout test details 112
6.6 Tangential slip *versus* pullout force relationship in FEM analyses 114
6.7 Interface behaviour in CaReCo FEM simulations using CM II 115
6.8 Interface behaviour in CaReCo FEM simulations using CM I/II 116
6.9 Interface contour plots of CaReCo FEM simulations 118
6.10 GFRP strains obtained in GlRoTe test and FEM simulation 119

A.1 FRPBonData website homepage 139
A.2 FRPBonData website list of papers page 140
A.3 FRPBonData website list of specimens page 140
A.4 FRPBonData website specimen details page 141
A.5 FRPBonData website database predefined charts page 142
A.6 FRPBonData website user defined charts page 143
A.7 FRPBonData website predictions page 143
A.8 FRPBonData website registering new specimens page 144
A.9 FRPBonData website about page 144

List of Tables

2.1 Recommended construction details for NSM FRP systems 15
2.2 Summary of the main variables included in the gathered databases 16

3.1 Error metrics obtained in all the analyses with ACI standard 32
3.2 Error metrics obtained in all the analyses with SA standard 35
3.3 Summary of the Data Mining analyses performed 41
3.4 Error metrics after *mining* analyses in DPT database 44
3.5 Error metrics after *mining* analyses in BPT database 44
3.6 Error metrics after *fit* analyses in both databases 49

4.1 Results obtained in the partial safety factors method 63
4.2 Results obtained in the reliability analyses of SA guideline 64
4.3 Error metrics of all theoretical models with reliability parameters 74

5.1 Direct pullout test campaign 80
5.2 Direct pullout tests main results 84

6.1 Details of the three modules composing the constitutive model 104
6.2 Parameters required in each constitutive model 108

This page was left blank intentionally.

Symbols

Subscripts

a	Adhesive
b	Bond
c	Concrete
f	FRP
g	Groove

Superscripts

e	Elastic
g	Global
l	Local
p	Plastic

Roman lower case letters

a_e	Edge distance
a_g	Groove spacing
b_c	Concrete block width
b_f	FRP thickness
b_g	Groove width
c	Shear strength
d_f	FRP width or diameter in quadrangular or round bars, respectively
d_g	Groove depth
f	Yield function
f_{ac}, f_{at}	Adhesive compressive and tensile strength, respectively
f_c, f_{ck}, f_{ct}	Concrete compressive, characteristic compressive and tensile strength, respectively
f_{fd}, f_{fk}, f_{fu}	FRP design, characteristic and ultimate tensile strength, respectively
g	Plastic potential
k_b, k_d	Groove to FRP width and depth ratio, respectively

$\underline{m}$	Plastic flow direction
$\underline{n}$	Yield surface gradient
p_f, p_g	FRP and groove perimeter, respectively
s_{lmax}	Loaded end slip corresponding to F_{fmax}

Roman upper case letters

A_c	Concrete block cross-section area
A_f	FRP bar cross-section area
$\underline{\underline{D}}$	Constitutive matrix
E_f	FRP bar modulus of elasticity
E_c	Concrete modulus of elasticity
F_{fmax}	Maximum pullout force installed in the FRP
$\underline{\underline{J}}$	Jacobian matrix
L_{arm}	Vertical distance from the centroid of the center hinge to FRP centroid
L_b	Bonded length
L_c	Concrete block length
L_d	Development length
L_{per}	SA failure plane perimeter
R, R_d, R_e, R_t	Probabilistic, design, experimental and theoretical resistance function, respectively

Greek lower case letters

γ_c	Concrete compressive strength partial safety factor
γ_f	FRP tensile strength partial safety factor
δ_b, δ_{max}	Bond slip and maximum bond slip, respectively
ε_{fmax}	Strain in the FRP corresponding to F_{fmax}
ε_{fu}	FRP ultimate strain
κ	Hardening parameter
σ_{dil}	Dilation stress
τ_{avg}	Average bond strength
$\tau_{avg,F/A}$	Average bond strength at FRP/adhesive interface
τ_b, τ_d, τ_{max}	Bond strength and its design and maximum values, respectively
$\tan\phi$	Friction angle
φ_{per}	SA failure perimeter ratio
χ	Tensile strength

Greek upper case letters

$\Delta\underline{s}$	Incremental slip vector
$\Delta\underline{s}^e$	Incremental elastic slip vector
$\Delta\underline{s}^p$	Incremental plastic slip vector
$\Delta\lambda$	Plastic multiplier
$\Delta\kappa$	Hardening law
$\Delta\underline{\sigma}$	Incremental stress vector
$\underline{\Phi}$	Hardening variables vector
$\underline{\Psi}$	Plastic potential variables vector

Acronyms

ACI American Concrete Institute.

ANN Artificial Neural Networks.

BPT Beam Pullout Tests.

CM Constitutive Model.

DM Data Mining.

DPT Direct Pullout Tests.

EBR Externally Bonded Reinforcement.

EC Eurocode.

FEM Finite Element Method.

FRP Fibre Reinforced Polymer: (B) basalt, (C) Carbon, (G) Glass.

MAE Mean Absolute Error.

NSM Near-Surface Mounted.

R^2 Squared Correlation Coefficient.

RC Reinforced Concrete.

RMSE Root Mean Squared Error.

SA Standards Australia.

SVM Support Vector Machines.

CHAPTER 1

Introduction

The Near-Surface Mounted (NSM) technique is one of the most effective techniques to strengthen concrete structures, mainly in flexure and shear (De Lorenzis and Teng, 2007). It consists on inserting the reinforcement material in the concrete cover of the element to be strengthened. The use of Fibre Reinforced Polymers (FRP) as reinforcing material in the context of the NSM technique has been intensively studied in the last 15 years due to their several advantages when compared with steel (Bakis et al., 2002).

The methods for application of NSM FRP systems depend on the FRP cross-section geometry. Nevertheless, the main steps are common to all FRP systems, as follows:

(i) execution of grooves on the face of the element to be strengthened;

(ii) cleaning of grooves with compressed air or water under pressure (in the end the grooves' surfaces should be dry and without any bond-inhibiting substances);

(iii) preparation of the FRP (cutting with the desired length and cleaning);

(iv) preparation of the adhesive (groove filler) according to its technical specifications;

(v) application of the adhesive in the grooves;

(vi) insertion of the FRP into the grooves under slight pressure to force the adhesive to flow between the FRP and the groove borders. This phase requires special care in order to assure that the grooves are completely filled with adhesive. When this is not the case, the formation of voids might occur;

(vii) removal of excess adhesive and groove external surface leveling.

When compared with the Externally Bonded Reinforcement (EBR) technique, NSM has the following key advantages (El-Hacha and Rizkalla, 2004; Parretti and Nanni, 2004; Seracino et al., 2007a):

(i) reduced amount of preparation work, requiring only the opening of the grooves avoiding removal of degraded surface and regularization of remaining surface;

(ii) less prone to premature debonding because the bonded area is larger, allowing a more efficient use of the reinforcement material (in some cases, FRP failure can be achieved);

(iii) ease in extending the reinforcement to adjacent elements;

(iv) greater protection of the FRP against external aggressive agents or acts of vandalism;

(v) smaller visual impact.

In terms of FRP cross-section, rectangular, square or round bars are commonly used. As the grooves have vertical and parallel sides, square and rectangular bars explore better this grooves' geometry since a more uniform adhesive thickness is achieved. Moreover, with the use of round bars, split of the groove filling cover may occur due to the existing stresses perpendicular to the FRP (De Lorenzis and Teng, 2007). In the case of square and rectangular bars this normal stress component acts mainly towards the groove lateral concrete.

Comparing square and rectangular bars, the latter maximize the ratio of surface to cross-section area, minimizing the bond stresses for the same tensile force in the FRP. Other advantage of using rectangular bars is related with the simplicity of opening the grooves: a single saw cut is normally enough for obtaining the groove while with round/square bars two saw cuts and removal of the concrete in between are usually required. The main disadvantage of rectangular bars is the need for a deeper groove to provide the same reinforcement area.

In terms of the adhesives used to bind FRP bars to concrete, epoxy adhesives are the most common, even though some researchers have used cement mortar (De Lorenzis, 2002; Macedo et al., 2008). In general, cement based adhesives have lower mechanical strength and higher curing time, when compared with epoxy adhesives. On the other hand, cement based adhesives present better performance when subjected to high temperatures.

1.1 Motivation

Despite the intensive research (see Figure 1.1) that has been devoted to the NSM FRP technique there are still many challenges to overcome. In particular, the characterization of the transfer of stresses between the FRP and the surrounding concrete, i.e. the bond behaviour of NSM FRP system, is not yet completely understood.

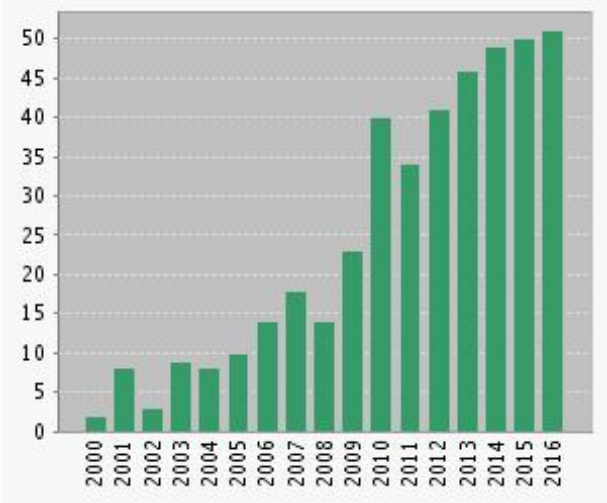

Figure 1.1: Amount of publications per year on the NSM technique (obtained in 18/10/2016 from ISI Web of Knowledge using the keywords "near-surface mounted concrete").

The bond behaviour has been studied through Direct Pullout Tests (DPT) and/or Beam Pullout Tests (BPT). While the later present a single configuration (with minor differences between authors), the former have been performed in a manifold of configurations (Coelho et al., 2015). This makes it very difficult to analyse and compare the DPT results obtained from different authors worldwide. On the other hand, trying to propose bond laws considering results obtained using different test configurations is quite challenging.

Nevertheless, in the past a few guidelines for NSM FRP systems in concrete have been proposed using the bond tests results available at that time, which were much lower than today. Hence, those guidelines need to be validated using more recent bond tests results. Also, the knowledge gained since those guidelines were developed needs to be incorporated to obtain newer and more robust guideline formulations.

The bond behaviour has been also theoretically studied, namely, through numerical analysis using the Finite Element Method (FEM). The main purpose of the numerical studies is to obtain FEM models that simultaneously allow deeper understanding the bond behaviour and predicting it. The difficulties in modelling the bond behaviour arise

from the high complexity of the NSM technique which involves three different materials (FRP, adhesive and concrete) and two different interfaces (FRP/adhesive and adhesive/concrete). While there are already available powerful constitutive models to simulate the behaviour of concrete, FRP and the adhesive binding them, the same cannot be said regarding the interfaces between the three materials. Hence, interface constitutive models need also to be developed.

1.2 Objectives and research methodology

The principal objective of this thesis was to add a contribution to the existing knowledge on the bond behaviour of NSM FRP systems in concrete. That contribution was materialized by the proposal of specific objectives, mainly:

- analytical bond laws to be used in the bond design of NSM FRP systems in concrete;
- a possible standard DPT to allow a more reliable direct comparison between experimental results from different origins;
- an interface constitutive model to allow the numerical simulation of the interfaces existing in NSM FRP systems.

Additionally, a website grouping all the collected works on pullout tests with NSM FRP systems in concrete was built. This was done with the purpose of providing to the scientific community a reference database which could ease the continuous update of the existing bond laws and also the validation of newer bond laws to be proposed in the future by other researchers. On the other hand, this website was built in order to allow anyone to gain access to the data mining based bond laws developed in this thesis.

To achieve the objectives referred above the research strategy depicted in Figure 1.2 was pursued. It consists of four major components:

(i) a first and basilar bibliographic component, in which a bibliographic survey on works with NSM FRP pullout tests was performed;

(ii) an analytical component, in which analytical bond laws were analysed;

(iii) an experimental component, consisting on a DPT campaign;

(iv) finally, in the numerical component, a three-dimensional interface constitutive model was developed to simulate the existing interfaces in NSM FRP systems in concrete.

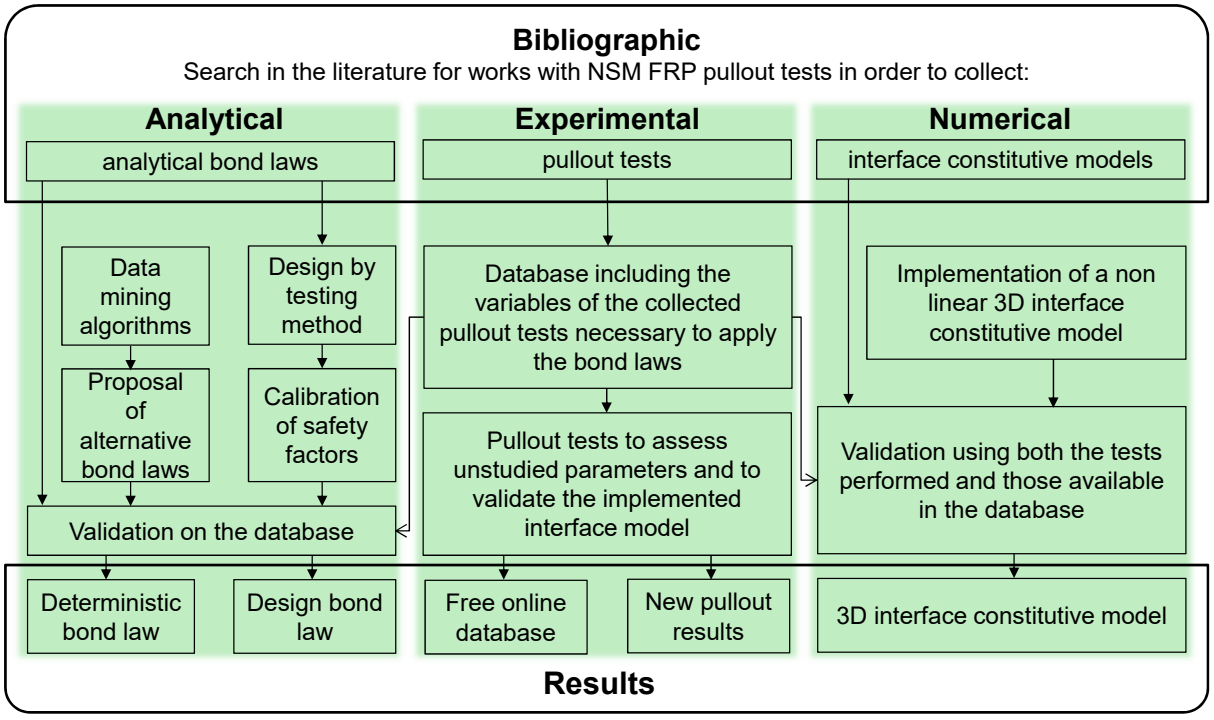

Figure 1.2: Thesis workflow.

1.3 Outline of the thesis

The work described in this thesis is organized in seven chapters. The content of each one is summarized in the following paragraphs.

Chapter 1 provides an introduction to the main subject of the present work. Motivation, objectives and research methodology pursued during the entire work are presented.

Chapter 2 presents a review of current knowledge on the bond behaviour of NSM FRP systems in concrete. In a first part, by analysing the physics of the phenomenon, the typical failure modes, the most common bond tests and two of the most important design guidelines for NSM FRP systems are introduced. In a second part, a database of bond tests composed by 431 records is presented and the most relevant parameters affecting the bond behaviour are discussed. A summary of the work described in this chapter can be found in the following publication: *Coelho, M.; Sena-Cruz, J.; Neves, L. (2015) "A review on the bond behavior of FRP NSM systems in concrete" Construction & Building Materials, 93: 1157–1169.*

Chapter 3 addresses two types of mechanical models for predicting the bond strength of NSM FRP systems in concrete. In a first part, the accuracy of the existing guidelines for NSM FRP systems is assessed and improvements to these guidelines are provided. In a second part, alternative mechanical models based on data mining algorithms are

introduced. The first part of this chapter was also included in the publication referred above. The second part, related with the mechanical models based on data mining algorithms, was published in: *Coelho, M.; Sena-Cruz, J.; Neves, L.; Pereira, M.; Cortez, P.; Miranda, T. (2016) "Using data mining algorithms to predict the bond strength of NSM FRP systems in concrete" Construction & Building Materials, 126: 484–495.*

Chapter 4 details a reliability analysis conducted in order to make the mechanical models analysed in Chapter 3 consistent with the Eurocodes philosophy. In the end, the partial safety factors necessary to allow designing bond in NSM FRP systems in concrete are provided for each mechanical model. The work described in this chapter is under revision in: *Coelho, M.; Neves, L.; Sena-Cruz, J. (2016) "Designing NSM FRP systems in concrete using partial safety factors" Submitted to Composites Part B.*

Chapter 5 describes an experimental campaign of direct pullout tests with NSM FRP systems in concrete. Several important and some unstudied parameters are tested and analysed. The obtained results aim at contribute to the development of a standard direct pullout test in the near future. The following paper summarizing the work described in this chapter is under preparation: *Coelho, M.; Sena-Cruz, J.; Neves, L.; Pereira, E. (2016) "Towards a standard direct pullout test for NSM FRP systems in concrete" to be submitted soon to Experimental Techniques.*

Chapter 6 presents a discontinuous-based three-dimensional constitutive model to simulate the existing interfaces in NSM FRP systems in concrete. The major details of its implementation and validation are described. Examples of direct pullout tests are simulated, including both tests extracted from the literature and tests performed by the author and described in Chapter 5. The work described in this chapter is summarized in: *Coelho, M.; Caggiano, A.; Sena-Cruz, J.; Neves, L. (2016) "Fracture-based interface model for NSM FRP systems in concrete" Composite Structures, 152: 816-828.*

Chapter 7 closes the present thesis with the most important conclusions that were obtained, as well as some suggestions for future developments on the research of bond behaviour of NSM FRP systems in concrete.

CHAPTER 2

A review on the bond behaviour of NSM FRP systems in concrete

The most recent comprehensive reviews on the Near-Surface Mounted (NSM) technique were published in 2007 (De Lorenzis and Teng, 2007) and, while this thesis was being developed, in 2015 (RILEM, 2015). These works address all aspects of NSM technique and, in order to provide a wider overview, do not focus on bond. Moreover, since then, a manifold of experimental works focusing on bond performance of NSM FRP systems have been developed. Hence, the scope of this chapter is to provide a review on the bond behaviour of NSM FRP systems in concrete. This review includes, in the first part, an introduction to the typical observed failure modes, the most commonly used bond tests and two of the most important design guidelines. In the second part of this chapter, two databases of bond tests are presented. Based on those databases, the most important parameters that influence the bond behaviour of NSM FRP systems in concrete are discussed.

2.1 Failure modes at structural level

Considering a Reinforced Concrete (RC) element strengthened in bending (and/or shear) with a Near-Surface Mounted (NSM) Fibre Reinforced Polymer (FRP) system, six failure modes combining different stress states on the three intervening materials (concrete, reinforcement steel and FRP) can occur.

Assuming firstly the failure of a single material, concrete crushing, FRP rupture or

FRP debonding are possible. These failure modes should be avoided since they lead to brittle failures. Concrete crushing may occur when longitudinal steel reinforcement ratio is too high and/or concrete strength is too low; if FRP reinforcement ratio is too low and its bonded length is high enough, FRP rupture can occur; finally, if the strengthening configuration does not allow the mobilization of the FRP system's full strength, FRP debonding may occur even before steel yielding.

When the NSM FRP system is properly designed, the expected failure modes are the combinations of concrete crushing and steel yielding, steel yielding and FRP rupture or steel yielding and FRP debonding. The internal cross-section equilibrium is achieved by the balance between concrete in compression and the contribution of both longitudinal steel and FRP in tension. Hence, the most efficient design solution will be the one which explores more efficiently the reinforcement materials (steel and FRP) thus conducting to concrete crushing after longitudinal steel yielding being the FRP safely close to failure. This leads to a ductile failure, with all materials being used up to their capacity.

The last two failure modes (steel yielding with FRP either in rupture or debonding) are the most difficult to predict because the existing bond strength prediction models are not robust enough yet. As a result, there is significant uncertainty regarding the definition of the critical failure mode, hindering the quality of strength predictions even for concrete crushing failures. In fact, if it was possible to predict the highest load that the FRP can attain without debonding, then it would be possible to design the FRP system not to fail in tension. Then, it would also be possible to check, by the internal cross-section equilibrium, whether or not the concrete strength allows full load transfer.

In order to better understand the failure by debonding of the FRP, Figure 2.1 presents a general example of a RC beam strengthened in bending with a NSM FRP system. This figure indicates the regions where the three major debonding failure modes can occur (ACI, 2008; SA, 2008). End debonding is associated with the concentration of stresses near the ends of the FRP and starts from its extremity to the centre of the beam, causing the failure of the strengthening system. Debonding caused by diagonal shear cracks, usually designated critical diagonal crack debonding, is associated with the development of a dominant shear crack. As soon as the crack reaches the FRP, it can propagate horizontally along the NSM FRP system towards the closest extremity, causing the failure of the strengthening system. Debonding caused by flexural cracks, commonly designated intermediate crack debonding, is in a manner similar to shear crack debonding phenomenon, but initiated by a flexural crack.

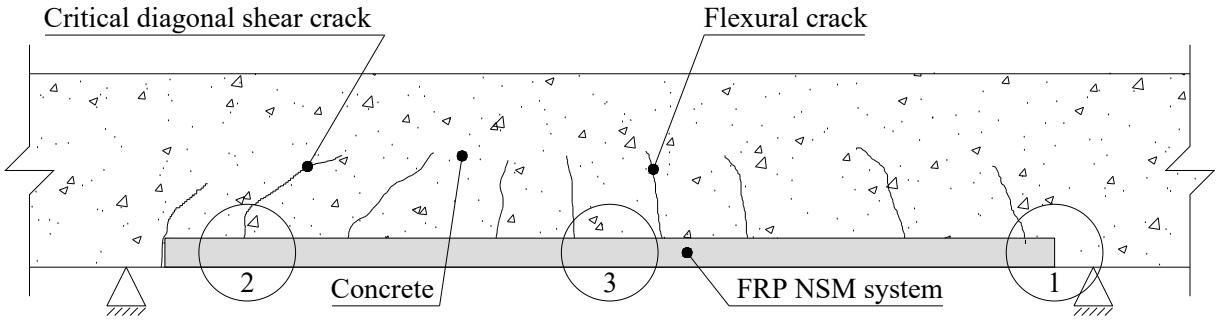

1 – End debonding; 2 – Debonding caused by diagonal shear cracks; 3 – Debonding caused by flexural cracks

Figure 2.1: Principal debonding failure modes in a RC beam strengthened in flexure with a NSM FRP system.

2.2 Failure modes at mesoscale

Each of the three debonding failure modes presented before can be in turn separated in four different local failure modes taking into account, not only the failure of the three materials involved in the NSM FRP system (concrete, FRP and adhesive) but also the existing interfaces (FRP/adhesive and adhesive/concrete). Figure 2.2 presents those failure modes for an example of a NSM FRP system with a rectangular bar.

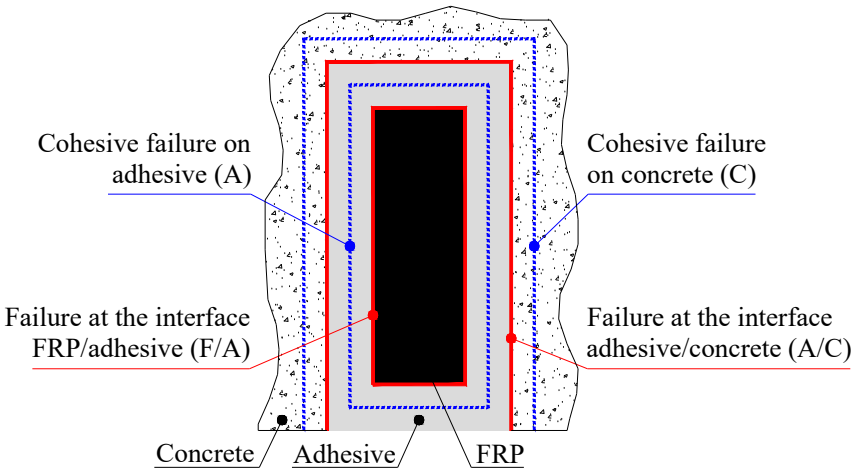

Figure 2.2: Four possible failure modes associated with debonding phenomenon.

To better explain these four failure modes, consider that the load is transferred from the FRP to concrete. Hence, it is expected that the first critical region where failure can take place will be the interface between FRP and adhesive (F/A). The resistance to this failure mode depends essentially on the degree of transverse confinement, bond length and adhesion mechanisms between FRP and adhesive.

Failure within the adhesive (A) depends also on the degree of transverse confinement

and on the mechanical properties of the adhesive (mainly shear resistance).

Failure at the interface between adhesive and concrete (A/C) depends on the same factors as the failure at the interface between FRP and adhesive, considering that the relevant adhesion mechanism is now between adhesive and concrete.

Finally, cohesive failure within the concrete (C) depends also on the degree of transverse confinement and on the mechanical properties of concrete.

Another aspect that should be stressed is that the interfacial failure modes have a similar physical appearance (i.e. the elements will become simply unconnected), while in the case of cohesive failure modes (in adhesive or concrete) several variations can be found, e.g. crushed, spalled, splitted or in a state resulting from a combination of these types of failures.

Summarizing, FRP debonding can occur at one of the three zones indicated in Figure 2.1 along one of the four regions indicated in Figure 2.2. Although debonding can occur simultaneously in more than one zone (see Figure 2.1) and along more than one region (see Figure 2.2) in the same RC element, at each level (structural and mesoscale) one of the failure modes will be determinant.

2.3 NSM bond tests

The bond behaviour of NSM FRP systems has been experimentally studied using the so-called bond tests. Several bond test configurations have been proposed for analysing in detail the debonding phenomena introduced in Section 2.1. These configurations can be grouped in Direct Pullout Tests (DPT) and Beam Pullout Tests (BPT). The DPT are more representative of end debonding and critical diagonal crack while BPT are recommended to study intermediate crack debonding.

DPT for NSM FRP systems were derived from the existing ones for reinforcement steel (RILEM, 1983). In the later, a concrete block is cast with a bar of steel in its centre with a predefined bond length. The test consists on pulling the steel bar out from the concrete block. The applied force and the corresponding slip (i.e., the relative displacement between the bar and the concrete block) are registered during the entire test. This relation between force and slip allows the definition of the usually nominated local bond-slip law, which is used to characterize the bond.

When DPT is used to study NSM FRP systems, the FRP is eccentrically located in the concrete block in order to be representative of NSM systems. A wide range of adaptations of the original setup has been proposed to study NSM FRP systems. Different setups lead to different stress states in concrete, which will be suitable to model different aspects

of NSM FRP systems. A detailed description of the different test setups found in the literature and the corresponding critical appraisal is provided in Section 2.5.

BPT for NSM FRP systems were also adapted from the BPT for reinforcement steel (RILEM, 1982). In this case, two identical concrete blocks are connected by a hinge system at the top and by a steel bar near the bottom. When the BPT is applied to NSM FRP systems, besides the use of FRP instead of steel, different bonded lengths between FRP and concrete are commonly used for each block composing the system. In one block, the FRP is fixed along its entire length, while in the other it is fixed in a smaller predefined length in order to localize the study of the debonding process.

Ideally, both types of tests should be used to fully characterize the bond behaviour of a NSM FRP system. In spite of that, as will be seen in the following sections, DPT are available in larger numbers due to the main advantages of this configuration in terms of practical use: DPT tests are easier, faster and less expensive than BPT ones. Moreover, the information given by the DPT is more important, since end debonding and critical diagonal crack occur for lower bond strengths.

2.4 NSM guidelines

In the past, several researchers have proposed formulations regarding the bond strength prediction of NSM FRP systems in concrete (De Lorenzis and Teng, 2007; Lee and Cheng, 2013). The calibration of those formulations is normally limited by the reduced number of tests performed, as well as, by the type of failure modes observed in the experimental programs. More recently, some of the existing formulations were tested using experimental results available in the literature and some modifications were also proposed (Lee and Cheng, 2013; Bilotta et al., 2014).

In this work, the focus was given to the existing guidelines for the use and design of NSM FRP systems in concrete. At least four guidelines were identified, namely the CAN/CSA S6-06 from Canadian Standards Association (CSA, 2006), the ACI 4402R-08 from American Concrete Institute (ACI, 2008), the HB 305–2008 from Standards Australia (SA, 2008) and the draft version of the new annex of Eurocode 2: Part 1-1 (CEN, 2004) by the TC250-SC2-WG1-TG1-N17 from the Comité Européen de Normalisation (CEN, 2013).

Regarding CAN/CSA S6-06 guideline, it was not considered in this study mainly because it does not propose a closed-form solution for the evaluation of the bond strength of NSM FRP systems. In fact, it refers that the bond strength should be obtained either by testing the NSM FRP system to be used, or it should be provided by the manufacturer.

The new annex of Eurocode 2 was also not considered in this study, since it is only applicable to FRP bars with rectangular cross-section (FRP strips). In addition, its formulation require some adhesive properties, such as tensile and compressive strengths, which are not often provided by the authors of the published experimental works, resulting in a marginal amount of specimens suitable to be analysed. Additionally, the expression proposed by this guideline to estimate the bond strength depends on some coefficients which shall be provided by the manufacturer for each NSM FRP system, or adjusted by testing.

Therefore, the remaining two guidelines were analysed and are presented in the following paragraphs: (i) the "Guide for the design and construction of externally bonded FRP systems for strengthening concrete structures" from the American Concrete Institute (ACI, 2008) referred as ACI; and (ii) the "Design handbook for reinforced concrete structures retrofitted with FRP and metal plates: beams and slabs" from the Standards Australia (SA, 2008), referred herein as SA. The formulation of both guidelines is based on the assumption that a certain bonded length (L_b) is required to develop the entire bond strength of the NSM FRP system, designated as development length (L_d). If $L_b \geq L_d$ the maximum bond force is achieved. Otherwise, it will be linearly reduced according to the ratio L_b/L_d.

To simplify the comparison between ACI and SA guidelines, Figure 2.3 presents their bond-slip laws while the following paragraphs describe each guideline formulation. This figure also shows two idealized bond-slip models assumed as representative of the real behaviour in NSM FRP systems in concrete (De Lorenzis and Teng, 2007): in general, a linear branch can be assumed for the pre-peak branch; depending on the friction degree, a horizontal plateau can exist or not in the softening phase.

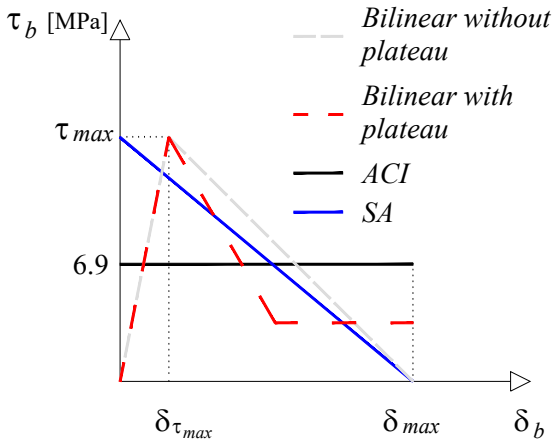

Figure 2.3: Bond-slip laws for NSM FRP systems.

2.4.1 American Concrete Institute formulation

In the American Concrete Institute (ACI) formulation, the key parameter is the maximum bond strength (τ_{max}) for the entire system (FRP/adhesive/concrete). If the bonded length (L_b) is greater or equal than the development length (L_d), the idealized bilinear shear stress distribution along the bond length can be approximated to a rectangular distribution. Hence, an average bond strength (τ_{avg}), constant and equal to 6.9 MPa for all NSM FRP systems, is assumed.

By imposing this average bond strength limit to the system's maximum capacity, the L_d and the maximum pullout force installed in the FRP (F_{fmax}) can be estimated using Equations 2.1 and 2.2, respectively. According to this guideline if $L_b \geq L_d$ the failure will occur by FRP rupture. Otherwise it will occur by one of the four bond failure modes referred before (see Figure 2.2), namely failure at the interfaces FRP/adhesive or adhesive/concrete or cohesive failure at the adhesive or concrete. However, since all failure modes are addressed using a single expression, no indication exists about the critical one.

In this formulation, F_{fmax} is predicted using only four parameters: FRP perimeter (p_f), cross-section area (A_f) and design tensile strength (f_{fd}) and the bonded length (L_b).

$$L_d = \left(A_f f_{fd}\right) / \left(p_f \tau_{avg}\right) \tag{2.1}$$

$$F_{fmax} = \begin{cases} A_f f_{fd} & \text{if } L_b \geq L_d \\ A_f f_{fd} \dfrac{L_b}{L_d} & \text{if } L_b < L_d \end{cases} \tag{2.2}$$

2.4.2 Standards Australia formulation

The Standards Australia (SA) formulation is somehow more robust than ACI as it was developed by solving the fundamental second order differential equation governing the bond phenomenon of NSM FRP systems by assuming the theoretical bilinear bond stress slip relationship without plateau (see Figure 2.3). This bilinear law can be simplified to a single linear descending branch since the error associated to this simplification was found to be marginal (Seracino et al., 2007b). With this strategy, the values of L_d and F_{fmax} can be estimated using Equations 2.3 and 2.4, respectively. Besides the parameters defining the bond-slip law (τ_{max} and δ_{max}), these equations include the axial stiffness of the FRP bar ($E_f A_f$) and the perimeter of the failure surface (L_{per}). SA defines that this failure perimeter is located 1 mm apart the FRP bar perimeter. SA guideline also includes expressions for the estimation of the bond strength (τ_{max}) and corresponding slip (δ_{max}). The evaluation of these entities (see Equations 2.5 and 2.6) depends on the

concrete compressive strength (f_c) and on the ratio between the depth and the width of failure perimeter (φ_{per}).

$$L_d = \frac{\pi}{2\sqrt{\frac{\tau_{max} L_{per}}{\delta_{max} E_f A_f}}} \tag{2.3}$$

$$F_{fmax} = \begin{cases} \sqrt{\tau_{max}\delta_{max}L_{per}E_f A_f} \leq A_f f_{fd} & \text{if } L_b \geq L_d \\ \sqrt{\tau_{max}\delta_{max}L_{per}E_f A_f}\dfrac{L_b}{L_d} \leq A_f f_{fd} & \text{if } L_b < L_d \end{cases} \tag{2.4}$$

$$\tau_{max} = \left(0.8 + 0.078\varphi_{per}\right) f_c^{0.6} \tag{2.5}$$

$$\delta_{max} = \left(0.73\varphi_{per}^{0.5} f_c^{0.67}\right) / \tau_{max} \tag{2.6}$$

Although SA and ACI guidelines present similar strategies for assessing F_{fmax}, there are interesting differences between them. The most relevant is that, while ACI only accounts for two types of failure modes (either be FRP rupture or an unspecified out of the four premature bond failure modes), SA accounts for three (FRP rupture, concrete cohesive failure or an unspecified premature bond failure mode out of the remaining three, i.e. cohesive at the adhesive or at the interfaces).

While in ACI guideline, the first branch of F_{fmax} equation – see Equation 2.2 ($L_b \geq L_d$) – is associated with FRP rupture, in SA it is associated with concrete cohesive failure instead. SA second branch ($L_b < L_d$) is associated with the remaining three premature bond failure modes (again, not specifying which). Finally, the right-hand side of both branches introduces the FRP rupture failure mode by limiting the maximum pullout force to the tensile strength of the FRP.

The use of SA formulation requires the definition of the following parameters: FRP geometry (for the evaluation of L_{per} and φ_{per}), FRP design tensile strength (f_{fd}), modulus of elasticity (E_f) and cross-section area (A_f), bonded length (L_b) and concrete compressive strength (f_c).

Finally, it should be stressed that SA formulation was developed for rectangular FRP bars. However, in the scope of the present work, it was also extended to square and round FRP bars. The necessary adaptations will be detailed further.

2.4.3 Construction details

In addition to the evaluation of F_{fmax} and L_d, it is also necessary, from both regulatory and practical standpoints, to define a set of construction details. The guidelines presented before (ACI and SA) provide some of these construction details.

From the bibliographic survey performed (detailed in the next sections), a review on these construction details was made and is summarized in Table 2.1. In this table acceptable limits for the groove width (b_g), depth (d_g) and spacing (a_g), as well as edge distance (a_e) are defined. It should be referred that the values in this table were obtained from different studies, using different NSM FRP systems and test configurations.

Table 2.1: Recommended construction details for NSM FRP systems.

FRP bar cross-section	**Round**	**Quadrangular**
Groove width (b_g)	$\geq 1.5d_f$ [1]	$\geq b_f + 3.0$ [3] $\geq 3.0b_f$ [2]
Groove depth (d_g)	$\geq 2.0d_f$ [1]	$\geq d_f + 3.0$ [3] $\geq 3.0d_f$ [2]
Groove spacing (a_g)	$\geq 2.0d_f$ [4]	≥ 53.0 [5] $> 2.0d_g$ [2]
Edge distance (a_e)	$\geq 4.0d_f$ [4]	≥ 30.0 [3] $\geq$ aggregate size [3] $\geq 3.5d_f$ [5] $> 4.0d_g$ [2]

$\geq 1.5d_f$ [2] (Groove width, Groove depth)

≥ 40.0 [6] (Groove spacing, Edge distance)

Notes: All units are in millimetres; d_f – FRP round bar diameter or quadrangular bar width; b_f – FRP quadrangular bar thickness.
[1]De Lorenzis (2002); [2]ACI (2008); [3]Blaschko (2003); [4]Hassan and Rizkalla (2004); [5]Rashid et al. (2008); [6]Kang et al. (2005).

As can be seen, in terms of groove width, only a lower limit was found in the literature. This limit aims at avoiding adhesive splitting due to the radial stresses in the FRP. However, an upper limit should also be defined in order to prevent the cohesive shear failure of the adhesive (Seracino et al., 2007a). Regarding the groove depth, from the literature it is clear that the bond performance increases with the grooves' depth; however, this parameter is limited by concrete cover. A minimum value for the spacing between grooves (a_g) is proposed to avoid group effect between consecutive FRP reinforcements. Similarly, a minimum value for a_e is suggested to avoid the premature failure of the edge of the concrete element.

2.5 Databases of bond tests

In order to allow a deeper understanding on the bond behaviour between FRP and concrete in NSM FRP systems, two databases of existing experimental programs were gathered: one for Direct Pullout Tests (DPT) and another one for Beam Pullout Tests (BPT).

Regarding DPT, experimental results were gathered from a total of 26 documents (Yan et al., 1999; De Lorenzis, 2002; De Lorenzis et al., 2004; Shield et al., 2005; Lundqvist et al., 2005; Teng et al., 2006; Seracino et al., 2007a; Thorenfeldt, 2007; Macedo et al., 2008; Rashid et al., 2008; Novidis and Pantazopoulou, 2008b; Yun et al., 2008; Oehlers et al., 2008; Kalupahana, 2009; Wang et al., 2009; Mitchell, 2010; Barros and Costa, 2010; Bilotta et al., 2011a; Soliman et al., 2011; Al-Mahmoud et al., 2011; Bilotta et al., 2012; Palmieri et al., 2012a,b; Lee et al., 2012; Seo et al., 2013; Capozucca, 2013). From those documents, 363 specimens were collected.

Regarding BPT, only 6 documents (De Lorenzis, 2002; Sena-Cruz, 2004; Novidis and Pantazopoulou, 2008a; Kotynia, 2012; Martin et al., 2012; Merdas et al., 2012) were found in the literature from which 68 specimens were collected.

Table 2.2 presents a summary of the range of the most important parameters included in the referred databases. In the next section a website storing the referred databases is presented while the following ones summarize the main variables studied in the experimental programs collected, as well as the major conclusions that can be drawn by considering them all together.

Table 2.2: Summary of the main variables included in the gathered databases.

Variable		**DPT**	**BPT**
Number of tests by FRP fibre type	Carbon	308	54
	Glass	28	6
	Basalt	27	8
Number of tests by FRP cross-section type	Rectangular	175	33
	Square	35	0
	Round	153	35
Bond length, L_b [mm]		[30-510]	[40-305]
Concrete compressive strength, f_c [MPa]		[18.4-65.7]	[26.7-73.5]
FRP thickness, b_f [mm]		[1.2-10.0]	[1.4-2.5]
FRP width or diameter, d_f [mm]		[6-40]	[8-20]
FRP cross-section area, A_f [mm^2]		[12-201]	[13-143]
FRP modulus of elasticity, E_f [GPa]		[37-273]	[34-171]
FRP tensile strength, f_{fu} [MPa]		[512-3100]	[773-2833]
FRP maximum pullout force, F_{fmax} [kN]		[8.8-205.1]	[2.9-61.9]
FRP strain corresponding to F_{fmax}, ε_{fmax} [‰]		[0.7-27.9]	[1.1-27.8]

2.5.1 Web-based tool

In the context of the present work, it was decided to build a website to store the referred databases. To do that, the collaboration of Paulo Cortez and Marta Pereira, respectively

a professor and a masters student from the Department of Information Systems of the University of Minho, was crucial. In fact, the majority of the website programming was performed by Marta Pereira.

Figure 2.4 presents the website's homepage while in appendix A some of the most important pages of the website are depicted.

It is believed that providing the scientific community free access to the vast majority of pullout tests available in the literature makes the process of continuously improving the existing prediction models faster and easier. It is expected that, with the contribution of all the researchers working in this field, this website will be continuously updated.

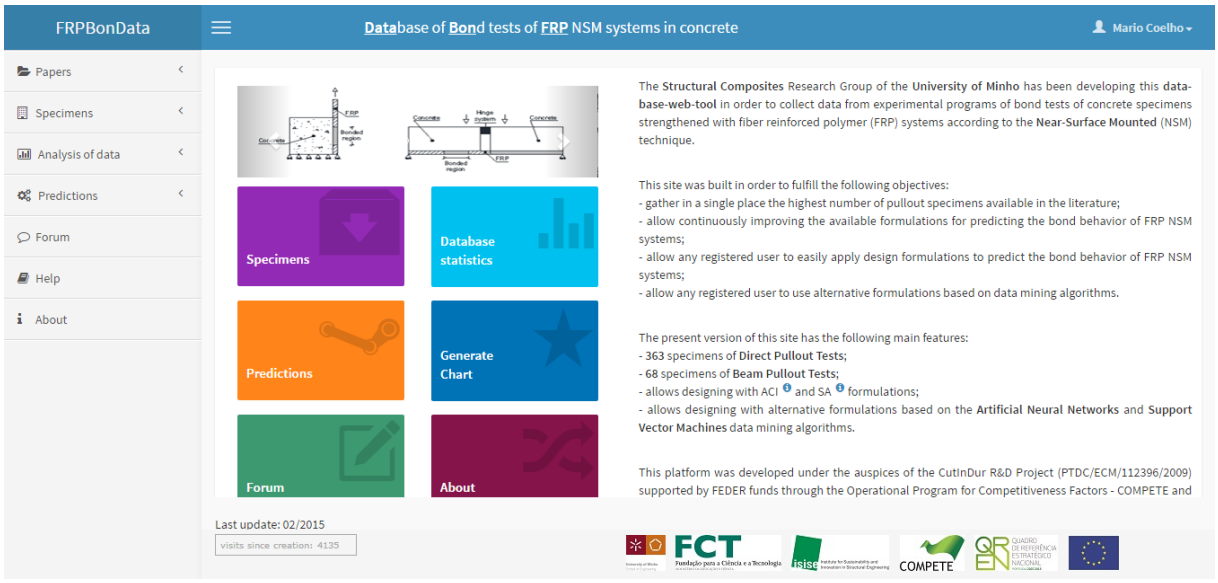

Figure 2.4: Homepage of the website developed to store the databases.

Due to the amount of specimens available in the database (363 DPT and 68 BPT), the present document do not contain the detailed information collected for each one. Alternatively, the reader should refer to the website in order to access the detailed information (www.frpbondata.civil.uminho.pt).

That detailed information is constituted for more than 60 parameters that were assessed for each specimen. Those are organized, for both types of tests (DPT and BPT), in the following six blocks of information:

(i) *General identification* – information necessary to identify each specimen and the document from which the data was collected;

(ii) *Concrete block geometry* – information related with the geometry of the concrete element;

(iii) *NSM configuration* – description of the NSM system configuration;

(iv) *Material properties* – divided in four sub-blocks, according to the four materials involved, namely, concrete, FRP, adhesive and steel (in those cases where reinforced concrete specimens were used instead of plain concrete specimens);

(v) *Results* – divided in two sub-blocks: one with the main results obtained from the experimental test and other with the results obtained by applying some design formulations (further detailed in this section);

(vi) *Analysis* – parameters obtained for the analysis of each specimen. It is divided in two parts: one related with geometric parameters and other related with strength parameters.

The referred website includes, besides the databases (with the six blocks of information detailed above), a page to perform predictions of the maximum pullout force (F_{fmax}) using different formulations. The user just needs to provide the required input variables and results obtained using all the prediction formulations described in this work will be readily available. This includes ACI and SA guidelines, already presented in Section 2.4, as well as alternative formulations based on data mining algorithms (introduced in Section 3.2.1).

Even though the formulations based on data mining algorithms are further discussed in this work, it is important to emphasize at this point that they are probably unknown by those interested this work. Besides, they are not straightforward to apply, since they require a computational environment to be used. Hence, the website also has the function of providing the computational environment to apply the data mining models developed in this work. It is believed that, by providing in the website an easy way of using and testing the referred data mining models, the acceptance and use of such powerful tools will increase.

To help the community in the development of improved prediction models for NSM bond behaviour a detailed and comprehensive data visualization tool is also included in the website. In addition, a forum is also available to ease the interaction between all the researchers contributing for the website.

2.5.2 Analysis of the databases

The following sections present the results of the analysis of both DPT and BPT databases. The analysis was divided in order to address some of the parameters which are considered the most important to better understand the bond behaviour.

2.5.2.1 Bonded length

In general, increasing the bonded length (L_b) leads to an increase in terms of the FRP maximum pullout force (F_{fmax}) and the corresponding strain (ε_{fmax}). Contrarily, the average tangential stresses at both interfaces (FRP/adhesive and adhesive/concrete) decrease due to the higher contact area between the FRP and surrounding materials and the non-uniform distribution of bond stresses along the bond length. These findings are valid both for DPT (De Lorenzis, 2002; Teng et al., 2006; Seracino et al., 2007a; Thorenfeldt, 2007; Kalupahana, 2009; Capozucca, 2013) and BPT (De Lorenzis, 2002; Sena-Cruz, 2004; Lundqvist et al., 2005; Novidis and Pantazopoulou, 2008a; Martin et al., 2012; Merdas et al., 2012) specimens.

Regarding DPT only, since there are specimens with very small values of L_b, it was found that the average bond stresses at the interfaces increase with the increase of L_b up to a threshold (L_d), after which it decreases. The L_b value was found to be equal to $5d_f$ (Novidis et al., 2007; Novidis and Pantazopoulou, 2008b) and $9.1d_f$ (Yan et al., 1999) for CFRP round bars. Taking into account that those values depend on the discrete values of L_b that were tested, a global threshold of 100 mm can be defined. For both CFRP rectangular bars (Seracino et al., 2007a) and GFRP round bars (Wang et al., 2009) this limit is suggested to be equal to 200 mm.

Even though the parameters that influence the definition of this limit (L_d) are not yet clearly identified, its existence has been proved experimentally. In fact, a minimum L_b is required to allow the mobilization of the entire bond-slip law. If a L_b larger than L_d is available, as the region near the loaded extremity becomes unbonded, the bond stresses migrate to the "extra" L_b. However, the maximum tangential stress value would not change since it is assumed that the bond-slip law is a mechanical characteristic of the strengthening system.

2.5.2.2 FRP fibre type and external surface

The type of FRP as well as the external surface play an important role in the bond response of NSM FRP systems. In identical DPT specimens and NSM FRP system configurations, it was found that F_{fmax} increases when moving from basalt (BFRP) to glass (GFRP) and from GFRP to carbon (CFRP) bars (Bilotta et al., 2011a; Soliman et al., 2011; Palmieri et al., 2012a,b). This is a consequence of the observed increasing stiffness from basalt to carbon.

As expected, smooth surfaces are more prone to failure in the FRP/adhesive interface. On the other hand, such failure modes are less sudden than the ones observed in roughened surface bars (Palmieri et al., 2012a,b).

Comparing FRP bars with different external surfaces it was found that F_{fmax} increases from manually roughened to sand coated to ribbed surfaces (Lee et al., 2012). This behaviour is related with the increase of the mechanical interlocking between the adhesive and the FRP surface provided by each type of external surface.

For BPT specimens it was verified that ribbed bars were more efficient than sand-blasted ones (De Lorenzis, 2002). This observation is in agreement with the results observed in DPT.

2.5.2.3 Groove surface

In the context of strengthening reinforced concrete structures, grooves are opened on the existing concrete cover. In spite of that, there are some studies in the literature associated with pre-molded grooves (De Lorenzis et al., 2002). Rough grooves (as a result of opening grooves in cured concrete) behaved much better than smooth ones (associated with pre-molded grooves) since the latter are more prone to failure at adhesive/concrete interface (De Lorenzis, 2002).

2.5.2.4 FRP axial stiffness

For the case of DPT, F_{fmax} increases with FRP axial stiffness ($E_f A_f$) up to the value of 8000 kN, from which no further load increase was observed (Bilotta et al., 2011a). To confirm the existence of such limit, Figure 2.5a presents the relationship between $E_f A_f$ and ε_{fmax}. For round FRP bars, ε_{fmax} decreases with $E_f A_f$ (lognormal trend with $R^2 = 0.79$). In the other cases (i.e. rectangular and square bars), since the dispersion of values is low nothing can be concluded, even though the trend in rectangular bars seems to be identical to the one observed in round bars.

Similar conclusions can be pointed out for the case of BPT specimens (see Figure 2.5b). The major differences are that: (i) no square specimens exist; (ii) the trend lines in rectangular and round FRP cross-section now are almost the same.

2.5.2.5 FRP cross-section geometry

Literature has confirmed that the FRP cross-section geometry also influences the bond performance. In fact, when the diameter (or the width for the case of rectangular cross-sections) of the FRP (d_f) increases, F_{fmax} and ε_{fmax} also increase and the tangential stress at FRP/adhesive interface ($\tau_{avg,F/A}$) decreases due to the greater contact area between the FRP bar and the adhesive (De Lorenzis, 2002; Thorenfeldt, 2007; Macedo et al., 2008).

For the case of CFRP round bars, the influence of d_f seems to be also dependent on the groove size. F_{fmax} increases with d_f if the ratio groove depth to bar diameter (d_g /

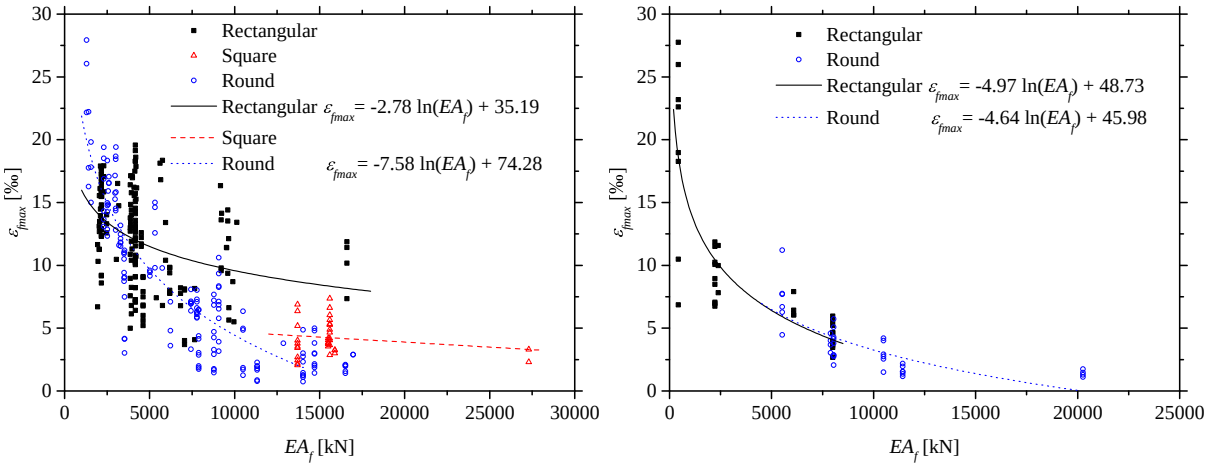

Figure 2.5: Influence of EA_f in ε_{fmax}: (a) DPT database; (b) BPT database.

d_f) is kept almost constant (Kalupahana, 2009), i.e. if the groove geometry (assuming that the width is equal to the depth) also increase at the same rate. But if the groove geometry is kept equal when d_f increases, then F_{fmax} decreases (Soliman et al., 2011), due to the reduction on the adhesive thickness. As explained in Section 2.4.3, there is a minimum adhesive thickness required to prevent the cohesive failure at the adhesive. In (Soliman et al., 2011), the reduction on the groove size changed the failure mode from cohesive at concrete to cohesive at the adhesive.

For the case of CFRP rectangular bars, increasing the FRP bar thickness (b_f) increases F_{fmax} mainly due to the larger cross-sectional area of the FRP (Seracino et al., 2007a; Oehlers et al., 2008).

Comparing directly specimens with FRP bars with different cross-sections, it is also confirmed that rectangular bars are more efficient, in terms of exploring the FRP capacity, than round bars (Merdas et al., 2012), since, as previously referred, rectangular bars maximize the surface to cross-section area ratio.

2.5.2.6 Groove's geometry

The influence of the groove's geometry was assessed by testing identical specimens where only the groove dimensions were changed. When both groove dimensions increase at the same proportion, F_{fmax} increases (Kalupahana, 2009). If the failure mode is cohesive at the adhesive then the average strength at the interface FRP/adhesive increases with groove size (keeping constant the ratio width to depth) (De Lorenzis, 2002). If the failure mode is at the interface adhesive/concrete, the average strength at the interface FRP/adhesive was found to decrease in De Lorenzis (2002) and to increase in Novidis

et al. (2007) and Novidis and Pantazopoulou (2008b). From the results reported by the authors it was not possible to understand these apparently contradictory results.

When increasing separately each groove dimension, it seems that depth has positive effect on F_{fmax}, due to the increase in terms of confinement provided by surrounding concrete, while the width has negative effect (Al-Mahmoud et al., 2011). This emphasizes the need for an upper limit to groove's width as referred in Section 2.4.3. Finally, if the failure mode is cohesive in concrete (Soliman et al., 2011) or at the interface FRP/adhesive (De Lorenzis, 2002), increasing the groove dimensions had no influence on F_{fmax}.

2.5.2.7 Shape ratio

Two different shape ratios were considered in this work: one for the width, $k_b = b_g/b_f$; and other for the depth, $k_d = d_g/d_f$. In these expressions b_f and d_f are the thickness and width in quadrangular FRP bars, respectively, d_f can also be the diameter for round FRP bars, while b_g and d_g are groove width and depth, respectively. If both shape ratios k_b and k_d are greater than 1.5 no splitting occurred at the epoxy adhesive in Bilotta et al. (2011a) while it was observed in Palmieri et al. (2012a,b). This suggests that these limit geometry ratios are not enough to avoid adhesive splitting. Additionally, other parameters (or relations) may be required to control the adhesive splitting, for instance making these ratios dependent on the external FRP surface.

2.5.2.8 Cover of the FRP

From the results gathered, the effect of the FRP cover was only studied for CFRP rectangular bars. It was found that F_{fmax} and the average bond strength at the two interfaces (FRP/adhesive and adhesive/concrete) increase with the increase of the cover (Macedo et al., 2008). It was also found that, when the CFRP is inserted in deeper grooves but without cover (the adhesive only exists in the interior part of the groove and up to the outer surface of the CFRP), the reduction in terms of strength and post-peak behaviour of the pullout force versus slip relationship is small (Oehlers et al., 2008). In any case, it should be kept in mind that in this case the failure mode was the same for both specimens with and without cover (cohesive within the concrete).

2.5.2.9 Concrete strength

As for the Externally Bonded Reinforcement (EBR) technique, concrete plays a critical role on the performance of the NSM strengthening technique. By default the maximum pullout force (F_{fmax}) increases with the increase of concrete compressive strength (f_c) up to a threshold value (Seracino et al., 2007a). This threshold value corresponds to

the change of the failure mode type from cohesive within concrete to another mode. As expected, when the failure mode is not cohesive within concrete, f_c had no effect in F_{fmax} (Sena-Cruz and Barros, 2004; Al-Mahmoud et al., 2011).

For the case of specimens where failure occurred in the concrete, a reasonably constant value was obtained for the ratio between F_{fmax} and the square root of f_c, implying that the ultimate load is directly related to the concrete tensile strength (Seracino et al., 2007a).

In Kalupahana (2009) the effect of f_c on F_{fmax} seemed to be dependent of the FRP bar surface configuration and on the bonded length (L_b). Different surface configurations result in different adhesion mechanisms which, as referred in Section 2.2, have a major influence in the obtained failure mode. Regarding L_b, it was found that the influence of f_c is greater in specimens with lower L_b, which is corroborated by the results presented in Merdas et al. (2012).

2.5.2.10 Bond test type

One critical aspect in the analysis of bond in NSM systems is the non-existence of a standard configuration for both direct (DPT) and beam (BPT) pullout tests. In fact, in the DPT experimental works studied, four different configurations were used to study the bond behaviour in NSM FRP systems. Figure 2.6 summarizes those configurations which have been separated by the number of test sides (single or double-shear) and the concrete stress state during the tests (compression or tension).

In general researchers use single-shear test configuration. Variations can be found in terms of concrete block shape, which can be cubic, prismatic or even C-shaped, in spite of the prismatic being the most used. Comparing single with double-shear tests, the first ones present the following advantages: (i) simpler preparation procedures since only one face of concrete block is used; and (ii) simpler control of testing procedure and results analysis since the test region is more localized. Comparing compression and tension single-shear tests, it would be expected that F_{fmax} would be higher in compression tests, as a consequence of the confinement provided by the support conditions. However, there are results of identical specimens from compression (Seracino et al., 2007a) and tension (Bilotta et al., 2011a) tests, where F_{fmax} is quite similar, even though concrete presented lower mechanical properties in the case of tension tests. The main reason that can be pointed out for such similarity is related to an unbonded length that was left between the bonded region and the top of the concrete element. This can have induced a compressive strength in the top of the concrete block, limiting the difference between compression and tension tests. In fact, the effect of leaving such unbonded length was assessed in compression tests and it was verified to achieve F_{fmax} identical to specimens

where no unbonded length was left (Seracino et al., 2007a). In any case, this must be verified experimentally since there are other parameters which may be influencing these conclusions.

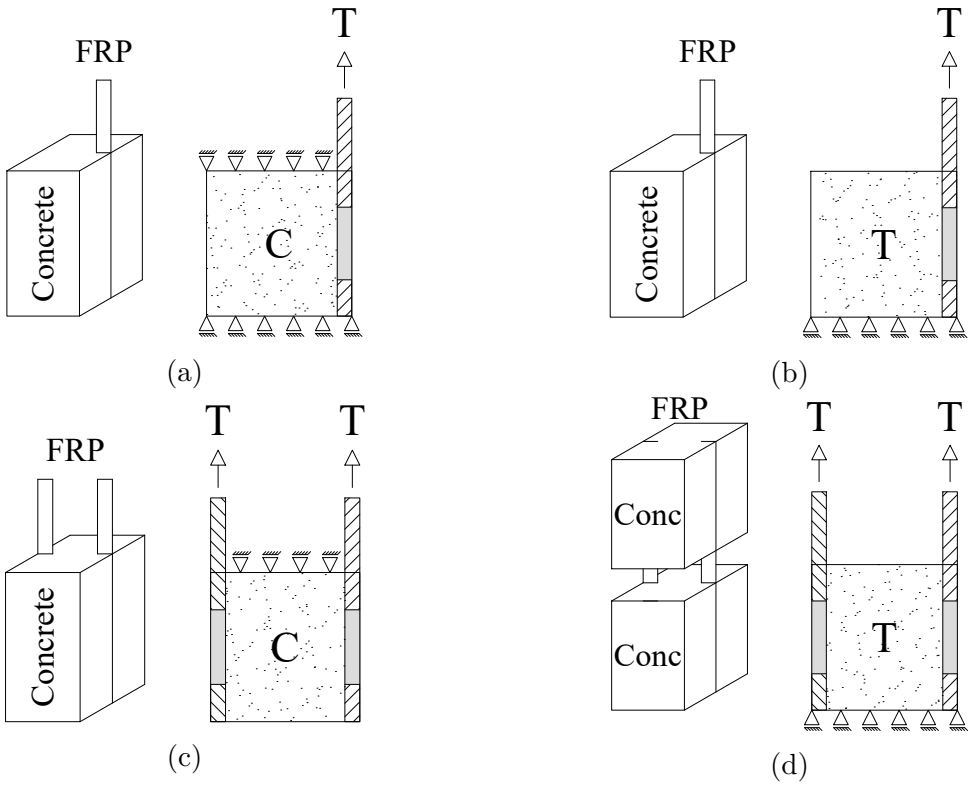

Figure 2.6: Summary of DPT configurations used in the works collected: single-shear compression (a) and tension (b) test; double-shear compression (c) and tension (d) test. NOTE: C – compression; T – tension.

The greater differences observed in the compression or tension pullout test setups can be found when the failure occurs within concrete. In compression tests, a concrete cohesive failure is generally observed, characterized by a concrete layer attached to the composite element (FRP/adhesive) after failure (e.g., Seracino et al., 2007a). For the case of tension tests, the concrete cohesive failure is characterized by a wedge of concrete starting from the free end of the bonded region to its loaded end (extremity closer to the loading point). Additionally, this wedge of concrete is limited by the location of the steel bars that reinforced the pullout specimen (e.g., Bilotta et al., 2011a). Taking into account the type of debonding phenomena that DPT are intended to represent, namely, end debonding and critical diagonal crack (see Figure 2.1), it can be seen that tension tests are more representative than compression tests.

Unlike the case of DPT, almost all BPT tests analysed used a common test configuration (c.f. Section 2.3).

Comparing DPT and BPT databases, it is interesting to note that larger bonded lengths are used in DPT test. In fact, the BPT configuration requires larger concrete blocks to study longer bonded lengths, making BPT more expensive, as referred in Section 2.3.

2.5.2.11 Failure modes

As referred in Section 2.2, there are five distinct failure modes that can occur in a pullout test, i.e. FRP rupture or one of the four premature bond failure modes (see Figure 2.2). However, the authors of the experimental works analysed tend to report more than one failure mode for the same specimen. Sometimes this happens due to the occurrence of a sudden failure during the tests, hiding the possibility of detecting the critical failure mode. Additionally, in the case of BPT specimens, the test configuration itself could lead to erroneous identification of failure modes. In fact, the BPT are performed with testing region (face where the FRP is applied) downwards, being more difficult to observe the development of the failure mechanism.

In order to have a homogeneous interpretation for the variety of failure modes that sometimes authors report, in the present work, those failure modes were grouped taking into account the most probable weakest component in the connection (concrete, FRP or interfaces). With this assumption, several different specific failure modes can be grouped under one of the five major failure modes' designations since in all of them the weak link is the same. The following paragraphs describe the reasoning used in the failure modes' grouping.

From all failure modes, failure of the FRP material is the simpler to recognize and is usually clearly reported by authors. Interfacial failure modes, FRP/adhesive and adhesive/concrete, are relatively simple to identify, even though sometimes they are referred associated to other failure mechanisms (e.g. adhesive splitting or concrete spalling). The strategy used in this work for those cases was to check, whenever photos of FRP and groove's surfaces after the test are provided. Interfacial failure modes will result in clean FRP surface without adhesive attached or in clean adhesive surface without concrete attached. Sometimes in the end of the test concrete or adhesive had split and those failure mechanisms are referred in addition to one of the interfacial failure modes but, after visual inspection, it was decided to classify those failures as interfacial. The shearing off of the FRP ribs, sometimes reported when round bars are used, was also classified as a failure at FRP/adhesive interface. In fact, mechanical interlocking between the adhesive and the ribs is part of the adherence mechanism in those types of FRP bars, in addition to chemical adhesion and friction between adhesive and FRP.

Cohesive failures, within concrete or adhesive, are mainly due to the normal stresses that develop together with longitudinal stresses during the pullout test. At some point, the normal stresses can reach concrete or adhesive tensile strength leading to its rupture. When there were doubts because both cohesive failures are reported, the specimen was classified according to its final appearance. If the groove remained almost intact (the corners might be slightly damaged) failure was classified as adhesive, otherwise as concrete failure. In fact, if failure occurs in the adhesive layer, concrete would not be damaged. If damage in concrete exists, adhesive could still have been destroyed as a consequence of the explosive type of failure that characterizes both cohesive failures.

The proposed approach is consistent with the literature. For example, Soliman et al. (2011) reported specimens where failure was cohesive at the concrete even though cracks in the adhesive were found after the test. Oehlers et al. (2008) also found similar behaviour in specimens without adhesive cover, where the reduction in the resistance due to the lack of cover is relatively small and concrete failure can be achieved. This corroborates the assumption that even if adhesive cover splitting occurs, the connection can still resist until concrete failure is reached due to the lateral confinement. Hence, adhesive splitting itself can sometimes be a consequence of other failure mechanism rather than be the mechanism responsible for bond loss.

The classification approach presented above was used whenever authors report more than one failure mode. Unfortunately, in the majority of the specimens available in BPT database, the failure mode reported is a combination of several mechanisms. Hence, only for the case of DPT an overview of the failure modes can be provided, as illustrated in Figure 2.7. This figure shows that all five failure modes referred before are relevant since they all can frequently occur. This highlights the complexity of this technique when compared to the Externally Bonded Reinforcement (EBR) technique where, in terms of premature bond failure, only detachment of concrete is relevant.

Additionally, it should be stressed that the evolution of the critical regions of failure suggested in Section 2.2 is experimentally confirmed. It was hypothesized that, for identical specimens where only bonded length is successively increased, interfacial failure modes would be the first to appear (firstly at FRP/adhesive interface, then at adhesive/concrete), followed by one of the cohesive failure modes and the last to occur would be the FRP rupture. That trend is verified, for example, in the specimens of Seracino et al. (2007a) and Bilotta et al. (2011a) where, for identical specimens, the maximum pullout force is lower when failure at FRP/adhesive interface occurred, then when failure at adhesive/concrete interface occurred and finally the higher pullout forces are registered for specimens where concrete cohesive failure occurred. Identical trend was also found by

Soliman et al. (2011) where it also can be seen that in some cases FRP rupture is attained for bonded lengths higher than those that originated the cohesive failure of concrete.

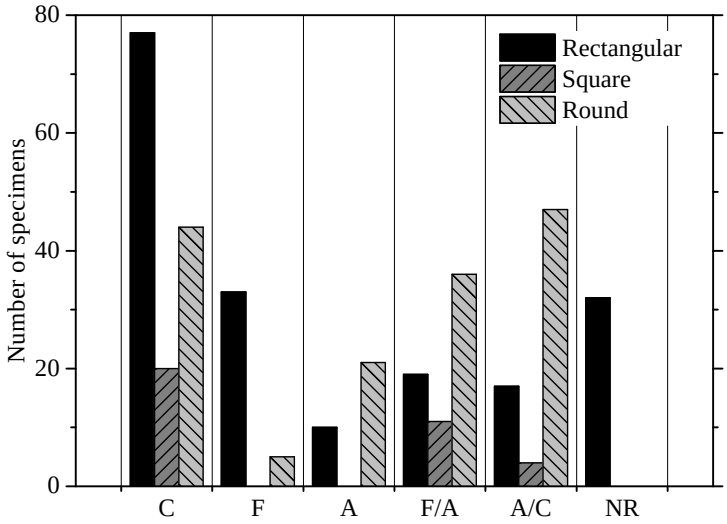

Figure 2.7: Summary of failure modes for the specimens in DPT database. NOTE: C – concrete cohesive failure; F – FRP rupture; A – adhesive cohesive failure; F/A – failure at FRP/adhesive interface; A/C – failure at adhesive/concrete interface; NR – not reported.

2.6 Unsolved issues

In the present chapter a review on the bond behaviour of NSM FRP systems in concrete was presented. In order to gradually introduce the subject of this work, the review began from the interpretation of the structural behaviour. Then, the mesoscale behaviour of such strengthening systems was analysed. The theoretical part of the review continued with the presentation of the bond tests used to assess the bond behaviour of NSM FRP systems in concrete and finished with an overview of the most relevant guidelines on this technique available worldwide.

The second part of the review consisted on the analysis of two databases of pullout tests with concrete elements strengthened with NSM FRP systems, one with DPT and other with BPT specimens. An attempt was made to jointly analyse the large number of experimental works existing in the databases. From the analysis of those databases, the following major conclusions can be drawn:

- the great majority of the experimental works' authors tend to present several failure modes since they look essentially to the final appearance of the specimens. However, as referred in the previous sections, it would be preferable to indicate only the critical

failure mode. Further research is thus necessary to establish a standard method to define and describe the failure modes observed;

- regarding the definition of standard pullout tests, BPT identical to those from steel are a consensual option. Once a standard geometry is chosen, this type of test will be defined. In the case of DPT, further experimental work shall be carried out to choose between compression or tension single shear tests. In fact, as it was verified in the previous sections, the final proposal of a standard DPT for NSM FRP systems would be one of these two;

- considering the amount of parameters which can influence the bond behaviour of NSM FRP systems, it can be said that the proposal of a holistic model for predicting their strength will be very difficult to obtain. However, considering that the number of different NSM FRP systems found in the experimental works collected is quite small, it could perhaps be better to consider NSM FRP systems' certification instead of trying to certify the NSM technique itself regardless to the reinforcement system being used.

CHAPTER 3

Bond strength of NSM FRP systems in concrete: mechanical models

The mechanical models to estimate the bond strength of NSM FRP systems in concrete included in ACI (ACI, 2008) and SA (SA, 2008) guidelines were published in 2008. They were developed using the experimental data available at that time. Since then, the amount of experimental data available increased. Thus, it is important to evaluate whether the new data confirms the adequacy of those mechanical models.

The following sections present the analyses carried out in order to assess the accuracy of both ACI and SA mechanical models. In addition, alternative models based on soft-computing techniques are also presented.

3.1 Analytical mechanical models analysis

The accuracy of both ACI and SA mechanical models was assessed applying them to the databases of direct (DPT) and beam (BPT) pullout tests introduced in Section 2.5. Three different analysis were conducted with each mechanical model, being the differences between the total six analyses conducted discussed in the following sections.

Regardless to the mechanical model being analysed, in all the six analysis referred above, the maximum pullout force was selected as the comparison variable. Furthermore, all the six analyses were performed using two distinct approaches: (i) data separated by the type of FRP cross-section; and, (ii) considering all the specimens together. The main purpose of using this two approaches was to assess the impact of having a single

formulation for all FRP cross-sections, since the NSM FRP system behaviour was found to be cross-section dependent, as shown in the previous chapter.

For all the analyses performed two error metrics were calculated, namely, the Mean Absolute Error (MAE) and the Root Mean Squared Error (RMSE). Those are defined in Equations 3.1 and 3.2, respectively. In these equations, the error e_i for the i^{th} specimen of the total N, is the difference between the maximum pullout force numerical prediction ($F_{fmax,Num}$) and its experimental value ($F_{fmax,Exp}$), as illustrated in Equation 3.3.

$$MAE = \sum_{i=1}^{N} \frac{|e_i|}{N} \tag{3.1}$$

$$RMSE = \sqrt{\sum_{i=1}^{N} \frac{e_i^2}{N}} \tag{3.2}$$

$$e_i = (F_{fmax,Num})_i - (F_{fmax,Exp})_i \tag{3.3}$$

3.1.1 ACI guideline

As referred in section 2.4.1, ACI formulation adopts a single value for the average bond strength (τ_{avg}), regardless to the type of FRP bar. In order to assess the impact of such assumption, in this section, three different analyses are presented differing on the value of τ_{avg}.

In a first analysis (A1), the value of 6.9 MPa suggested by ACI for τ_{avg} was considered. This analysis was used as reference and allowed assessing the accuracy of ACI formulation.

In a second analysis (A2), a recalibration of τ_{avg} was tested. This new value was obtained by minimizing the sum of the predictions' errors.

Finally, in the third analysis (A3), a new expression for τ_{avg} was proposed as a function of the geometrical ratio defined in Equation 3.4. In fact, it does not seem reasonable to have a constant value for τ_{avg}. In the present study the relation presented in Equation 3.4 was proposed as an alternative, where parameters a and b were calibrated based on the results available in the databases.

$$\tau_{avg} = a \left(\frac{A_f}{p_f L_b} \right)^b \tag{3.4}$$

In the case of Direct Pullout Tests (DPT) database, the number of specimens used in all the three analyses, divided by FRP cross-section type, was: 175 rectangular, 35 square and 153 round. Figure 3.1 presents the results obtained in the three analyses in terms of relationship between experimental and predicted pullout force. As it can be seen in all charts, the accuracy of the predictions improved from analysis A1 to A2 and from A2 to

A3, confirming that τ_{avg} is cross-section dependent. This conclusion is also corroborated by the error metrics shown in Table 3.1, which decrease from analysis A1 to A3.

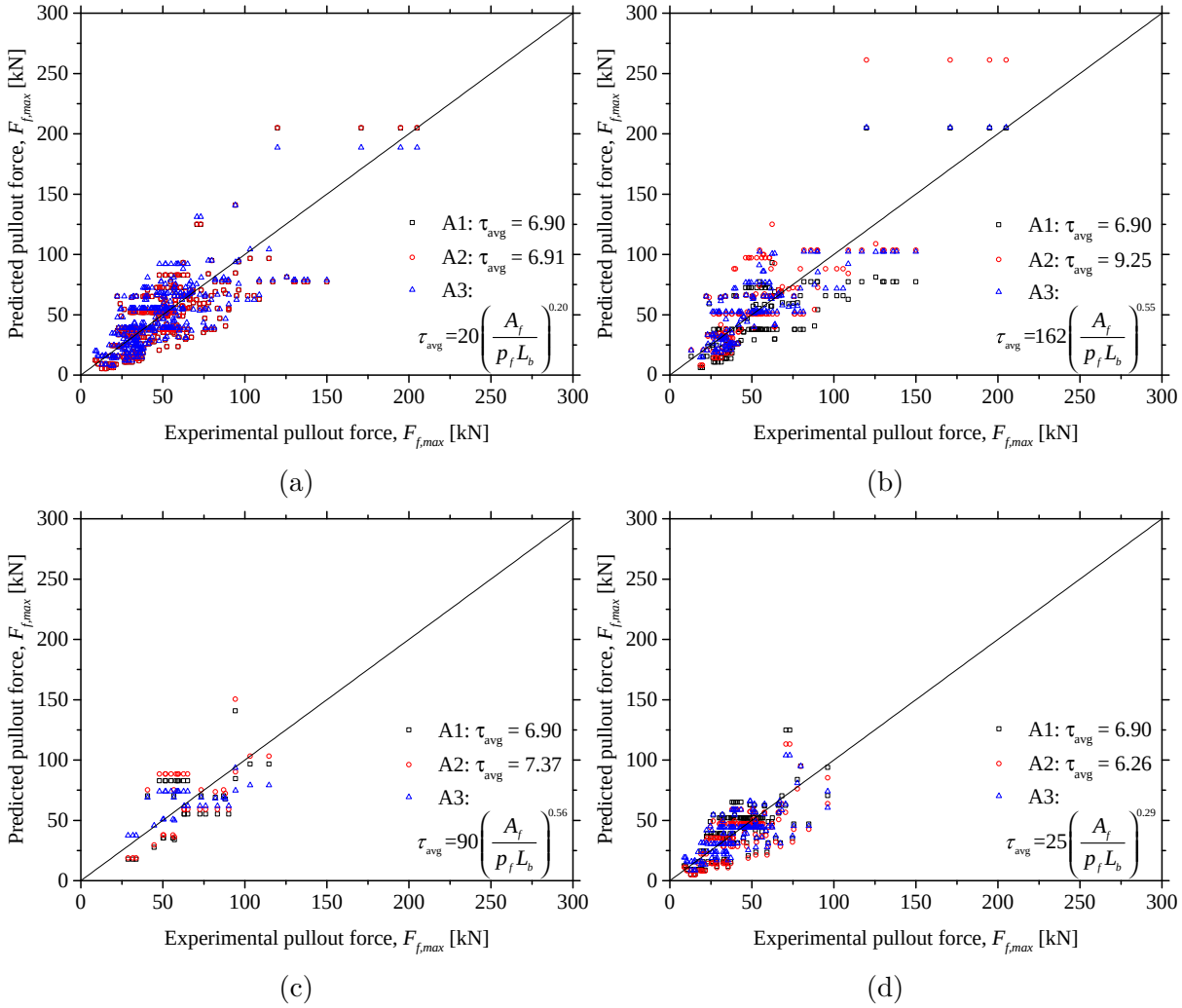

Figure 3.1: Results for the analyses with ACI standard (DPT database): (a) all 363 specimens; (b) 175 rectangular specimens only; (c) 35 square specimens only; (d) 153 round specimens only. (Note: τ_{avg} in MPa; A_f in mm^2; p_f and L_b in mm)

It was also interesting to find that, when all specimens are considered together, the value of 6.91 MPa for τ_{avg} was obtained in the analysis A2, which is practically the value recommended by ACI. This suggests that ACI's proposal is adequate if a single value of τ_{avg} is to be used for all geometries.

In the case of BPT database, the number of specimens used in all the three analyses, divided by FRP cross-section type, was: 33 rectangular and 35 round. Figure 3.2 and Table 3.1 present the results obtained in the three analyses using BPT database, where it can be seen that the same conclusions drawn before for DPT remain valid in BPT, i.e. from A1 to A3 analyses the results were successively better.

Table 3.1: Error metrics obtained in all the analyses with ACI standard.

Database	FRP cross-section	Rectangular		Square		Round		All	
	Analysis	MAE [kN]	RMSE [kN]	MAE [kN]	RMSE [kN]	MAE [kN]	RMSE [kN]	MAE [kN]	RMSE [kN]
DPT	**A1**	16.53	21.81	19.69	21.73	11.83	15.34	14.85	19.34
	A2	16.01	24.10	19.42	23.13	11.25	14.78	14.85	19.34
	A3	13.19	18.17	13.03	16.01	9.89	13.21	14.43	19.12
BPT	**A1**	8.25	9.21	-	-	12.92	16.66	10.65	13.56
	A2	7.08	8.39	-	-	11.53	14.23	10.61	12.98
	A3	7.29	9.03	-	-	9.57	12.67	9.76	12.32

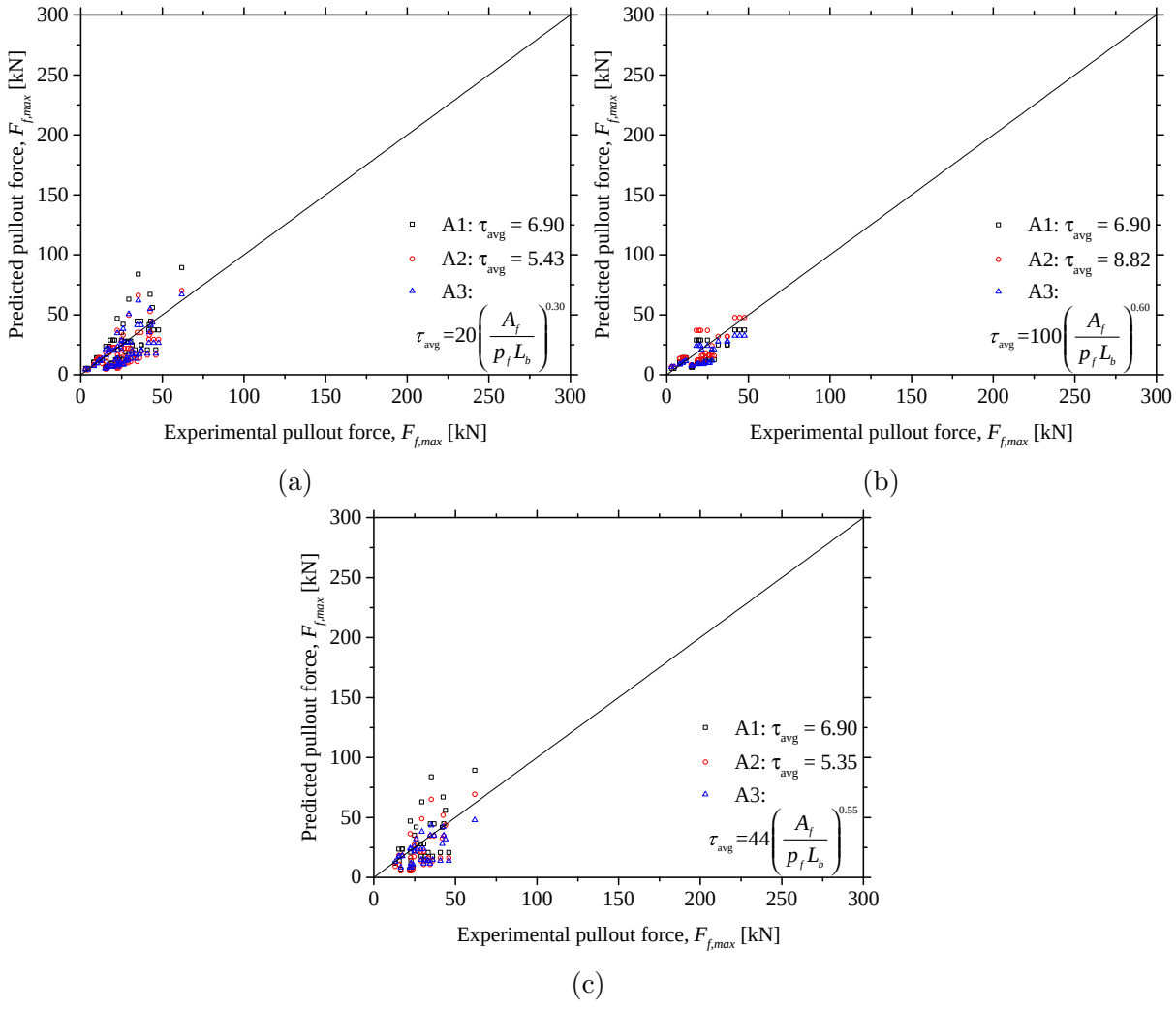

Figure 3.2: Results for the analyses with ACI standard (BPT database): (a) all 68 specimens; (b) 33 rectangular specimens only; (c) 35 round specimens only. (Note: τ_{avg} in MPa; A_f in mm^2; p_f and L_b in mm)

3.1.2 SA guideline

As referred in Section 2.4.2, the formulation included in the SA was developed for rectangular FRP bars and assumes that the failure perimeter is located 1 mm apart from the FRP bar perimeter.

In order to assess the possibility of extending this formulation to square and round FRP bar cross-sections, two different analyses were conducted differing in terms of the failure perimeter location. The first analysis (A1) coincides with that foreseen in SA formulation, thus the failure perimeter was assumed to be located 1 mm from the FRP bar perimeter, being the FRP located in the middle of the groove. Special care was taken to consider the different FRP cross-sections available in both databases. This failure perimeter was nominated $L_{per,f}$ since it is related with the FRP geometry.

To make the failure perimeter independent from the FRP cross-section, a second scenario was considered in which the failure perimeter was assumed to be located 1 mm from the groove perimeter. In this second analysis (A2) the failure perimeter was designated $L_{per,g}$ since it is related with the groove geometry.

After applying SA formulation with these two different failure perimeters, it was found that the second scenario (i.e. $L_{per,g}$) resulted in lower prediction errors, for both DPT and BPT databases. This conclusion is quite interesting since it allows having a single formulation for both types of tests in addition to be FRP cross-section's independent.

Having the failure perimeter location defined 1 mm apart the groove perimeter ($L_{per,g}$), a third analysis (A3) was then carried out. In this third analysis, the parameters of SA formulation that were obtained through experimental calibration, were recalibrated using the databases presented herein and a strategy identical to that used by SA authors (Seracino et al., 2007b). This strategy consists on, based on the experimental results, calibrating the coefficients included in Equations 2.5 and 2.6.

Identically to what was made earlier for ACI analyses, Figures 3.3 and 3.4 present the relationship between experimental and predicted pullout force for the three analyses with SA formulation using DPT and BPT databases, respectively, while Table 3.2 presents the error metrics for all the analyses with SA standard.

Since the first two analyses to choose the failure perimeter location (A1 and A2), depend on different parameters and considering that those were not always provided by the experimental works' authors, the number of specimens used in each one varies. Hence, the legend of the first two analyses also includes the number of specimens used (presented in parentheses).

In the case of the third analysis (A3), the legend of each figure includes only the final recalibrated expressions. Since the failure perimeter considered is the same of A2 analysis

(i.e. $L_{per,g}$), the number of specimens is also the same, thus was not repeated.

Both Figures 3.3 and 3.4 show the better performance of analysis A2 (using $L_{per,g}$) when compared with analysis A1 (using $L_{per,f}$), as referred before. Regarding the re-calibration analysis (A3), it can be seen that the predictions improved when compared with analysis A2, which uses also $L_{per,g}$ but the original SA expressions as presented in Equations 2.5 and 2.6. This was already expected since the number of specimens used in this work is larger than that used by SA's authors and an adjustment in the coefficients of those expressions would probably be necessary. Additionally, it can be seen that SA formulation presents better results for FRP rectangular bars than for round bars. This is related with the fact that SA formulation was derived for rectangular bars, thus not accounting for the specific bond behaviour of FRP round bars.

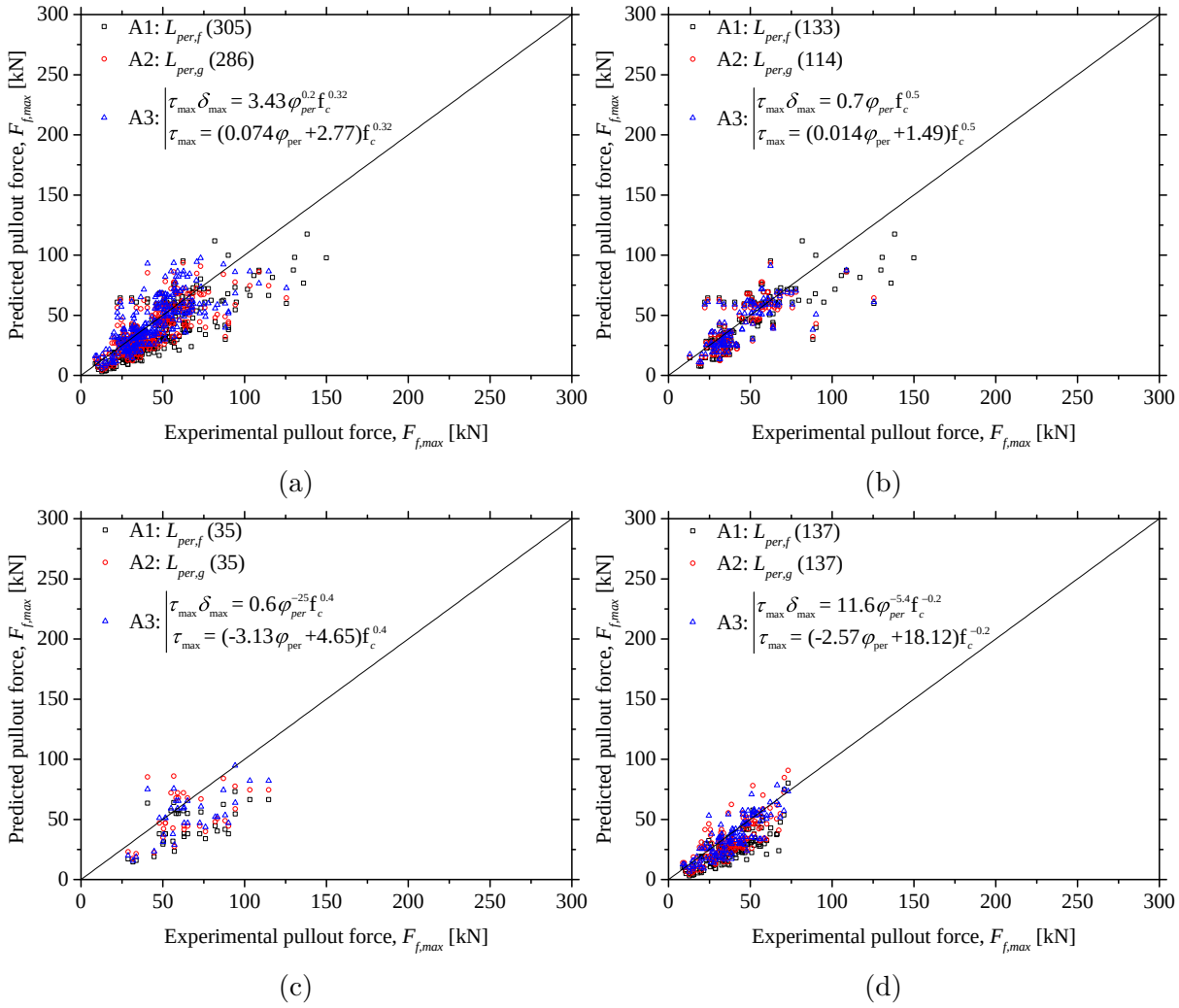

Figure 3.3: Results for the analyses with SA standard (DPT database): (a) all specimens; (b) rectangular specimens only; (c) square specimens only; (d) round specimens only. (Note: f_c and τ_{max} in MPa; δ_{max} in mm)

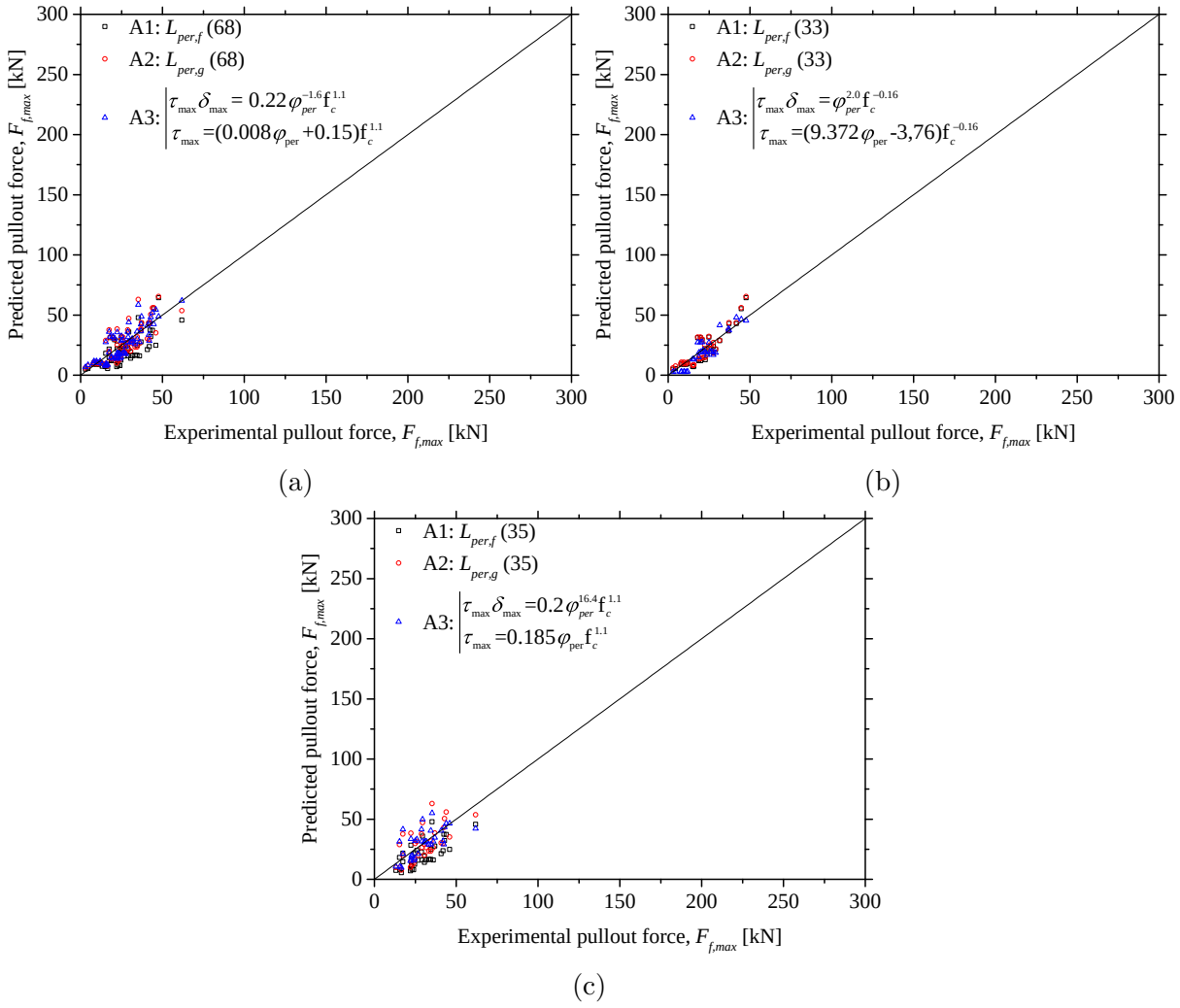

Figure 3.4: Results for the analyses with SA standard (BPT database): (a) all specimens; (b) rectangular specimens only; (c) round specimens only. (Note: f_c and τ_{max} in MPa; δ_{max} in mm)

Table 3.2: Error metrics obtained in all the analyses with SA standard.

Database	FRP cross-section	Rectangular		Square		Round		All	
	Analysis	MAE [kN]	RMSE [kN]	MAE [kN]	RMSE [kN]	MAE [kN]	RMSE [kN]	MAE [kN]	RMSE [kN]
DPT	**A1**	13.61	18.62	23.53	27.36	14.06	16.26	14.95	18.87
	A2	10.71	15.14	20.04	23.84	10.11	11.99	11.56	15.16
	A3	9.73	14.13	16.85	20.75	7.42	9.70	10.59	14.14
BPT	A1	5.61	6.94	-	-	11.13	12.39	8.45	10.12
	A2	5.24	6.71	-	-	9.00	10.57	7.18	8.90
	A3	4.81	5.84	-	-	7.14	9.51	6.23	7.68

3.2 Data mining mechanical models analysis

As shown in the previous sections, both ACI and SA guidelines formulations require improvements in order to become more accurate. In an attempt to provide an alternative to ACI and SA formulations, this section introduces the use of bond strength prediction models based on Data Mining (DM) algorithms.

In order to provide some insights on the use of DM in structural engineering, the following sections present a brief overview on DM, focusing on its use in the context of this work. However, contrarily to what is common in the literature, no theoretical or mathematical formulations will be provided herein. Alternatively, basic concepts will be presented since it is believed that, once the fundamental concepts are perceived, the acceptance of the mathematical formulations will be straightforward. The mathematical formulations can be obtained in the extensive existing literature on the mathematical background and implementation of these algorithms. Some examples will be provided latter.

In the end of this section, a comparison between the accuracy of ACI and SA formulations (presented in the previous section) and that of DM models is presented.

3.2.1 Data mining models

Traditionally, the procedure adopted to achieve any mechanical model is fundamentally empirical and ends up being a trial and error process. Three generic main steps can be outlined: (i) identify the problem, define an initial hypothesis and a method for testing it; (ii) run the test; (iii) analyse the test results and try to infer them to identical situations. In the present work the problem to be studied is the estimation of bond strength between FRP and concrete, which is believed to be assessable by bond tests. The traditional procedure is to perform a large set of bond tests, analyse the results and extrapolate them to identical situations. For instance, ACI and SA guidelines were developed in this way.

Regarding the third step, the most common procedure is a trial and error fitting of a mathematical expression (normally chosen in order to have physical significance in that context) to the results obtained in the tests using a set of previously chosen input parameters and regression analysis. If the tests are representative of the phenomenon being studied and if the obtained expression fits well the tests results, then it would be possible to use that expression in identical scenarios. All these steps are iteratively run until an acceptable solution is found for the model describing the phenomenon being studied.

Data Mining (DM) (Fayyad et al., 1996a), which aims at the semi-automatic extraction of useful knowledge from raw data, is an interesting alternative tool to ease and speed up the last step of the process described above. In fact, one of the several tasks that DM algorithms are capable of performing is regression, i.e. finding a data-driven model that is capable of predicting the real value of some (dependent) variable when some (independent) input variable(s) is(are) provided. The main drawback of using DM compared to traditional data analysis procedure is that the former, depending on the algorithm used, might not allow obtaining a closed form expression for the prediction model. Instead, several DM models are based in terms of complex mathematical functions or rules, thus the user can only see the input and output variables, in what is often termed as "black-box" models (Cortez and Embrechts, 2013). As an advantage, the DM approach simplifies the data analysis process (Fayyad et al., 1996b). In effect, DM models tend to be more flexible, being capable of predicting complex non-linear mappings and dealing with large amounts of data or noise. Such model learning flexibility often leads to higher predictive performances when compared with classical statistical models (e.g., multiple regression).

DM algorithms have been successfully used in regression tasks in many areas, including Civil Engineering (e.g. Tinoco et al., 2011; Martins and Miranda, 2012; Garzón-Roca et al., 2013; Chojaczyk et al., 2015). More specifically, in the field of concrete structures strengthened with FRP systems there are examples where DM algorithms have been used to predict the lateral confinement coefficient for reinforced concrete columns wrapped with CFRP (Doran et al., 2015), the strength of FRP confined concrete cylinders (Çevik, 2011) or the shear strength of reinforced concrete beams reinforced with FRP systems (Lee and Lee, 2014). According to the author's best knowledge, only one work of his authorship is available where DM algorithms were applied to predict the bond strength of NSM FRP systems in concrete (Coelho et al., 2013).

In this work, two DM algorithms were used: the Artificial Neural Networks (ANN) and the Support Vector Machines (SVM). These DM algorithms are briefly presented in the following sections.

3.2.1.1 Artificial Neural Networks

The Artificial Neural Networks (ANN) is an algorithm that is inspired in the behaviour of the human central nervous system. Hence, the learning ANN algorithm aims at finding the best connection weights in which a set of artificial neurons should communicate with each other in order to attain a certain target (Haykin, 2009).

Figure 3.5 presents two ANN examples: (i) Figure 3.5a corresponds to a multiple linear regression, which is a widely known and commonly accepted type of regression

model. This is an example of the simplest ANN, without hidden nodes; (ii) Figure 3.5b corresponds to a more complex ANN with one hidden layer and two hidden neurons (HN). As it can be seen, the only difference between them is the existence or not of an intermediate layer of hidden neurons.

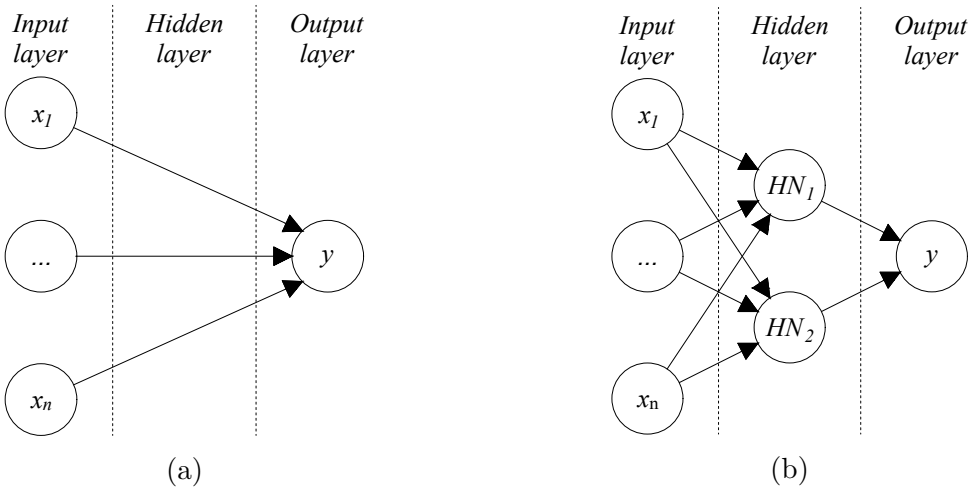

Figure 3.5: Example of ANN: (a) without hidden layers; (b) with one hidden layer.

In the multiple linear regression, several input variables (x) affected by different weights are combined and an output variable (y) is obtained. In the ANN with one hidden layer intermediary weights are also introduced thus a non-linear relation between x and y can be obtained. The number of hidden layers and neurons can be different from this example and, by increasing them, the degree of non-linearity increases.

If the value of y is known *a priori*, then the multiple linear regression model is an expression identical to Equation 3.5, where the only unknown is the set of weights (w) that make the equality true. In the case of ANN with hidden layers, such an expression is no longer straightforward to obtain. However, a similar procedure, minimizing the difference between the predicted and observed values can be used to find the optimal weights, in a process called training.

$$y = w_0 + \sum_{i=1}^{n} w_i x_i \tag{3.5}$$

The type of ANN adopted in this work uses only one hidden layer since this is the simplest non-linear ANN and was found to attain good results. The number of hidden neurons was determined during the analysis by comparing the quality of fit with increasing number of neurons (between 0 and 9) and selecting the one which presents lower prediction errors (when considering training data).

3.2.1.2 Support Vector Machines

Support Vector Machines (SVM) can be seen as an upgrade to ANN and were initially developed for classification tasks (Cortes and Vapnik, 1995). Considering the classification purpose, the basic concept of SVM is finding an optimal hyperplane for linearly separate patterns, i.e., finding the plane which maximizes the separation between the different patterns that exist in the analysed data.

To ease the understanding of SVM functioning in a classification task, Figure 3.6 presents an example of a database with two input variables (x_1 and x_2) divided in two patterns (circles and squares). In the database real space (middle chart in Figure 3.6) those patterns can only be separated using a curved line. However, it can be found a function ϕ_1 which, applied to the original data, can transform it into a new high dimensional space where the two patterns can actually be separated by a straight line. SVM algorithm optimizes the position of that single line such that it maximizes the separation of the two patterns.

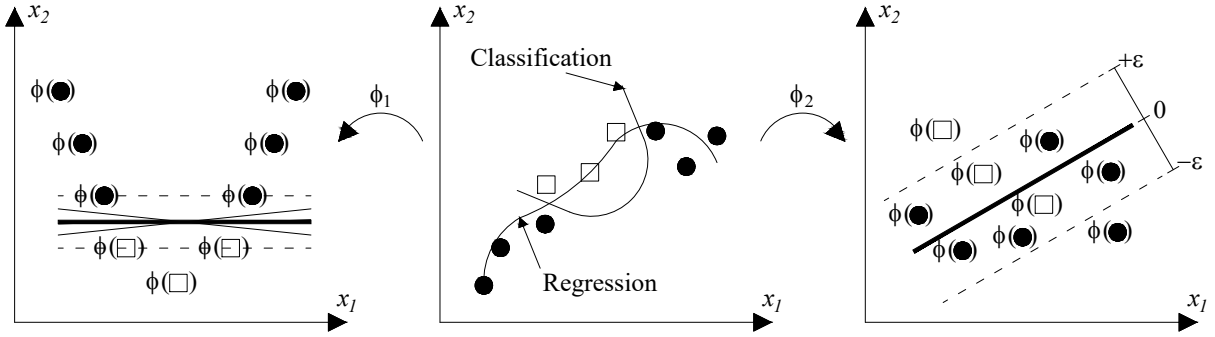

Figure 3.6: Example of SVM classification (left) and regression (right) of non-linear data (middle).

Several division lines can exist and are represented as full lines in the left side of Figure 3.6. However, in this case, the line that maximizes the separation of the patterns is the thicker one represented in that figure. Note that, in more complex examples (with several variables), the lines would actually be hyperplanes. In the end, since the optimal hyperplane is known, the relative position of all the data points, especially those passed by the dashed lines (designated by support vectors) is also known. Hence, a model traducing the separation of the patterns can be defined which corresponds to the classification model that was sought in the beginning.

SVM were latter extended to also perform regression tasks, which are the objective of the present work, being its functioning similar to the classification case. However, in regression, another function ϕ_2 will transform the original data in order to find a line that passes through all data points (right chart in Figure 3.6). That line is the regression

function which allows predict the value of each data point. Since finding such a line is quite complex, there are two new important parameters in the SVM for regression, namely the regularization parameter (C) and a loss function that in this work is the ε-insensitive (ε). The first defines the trade-off between complexity and accuracy of the model to be found, while the second defines the width of a region in which the data points inside it are assumed to be on the regression line, thus an insensitive region. The data points outside this region are the support vectors in the regression SVM.

Besides these two parameters, the success of SVM for regression tasks is influenced by a kernel function. In this work, the Gaussian radial basis kernel function was adopted (3.6). This has only one hyper-parameter, γ, which was adjusted using a greedy search (between 2^{-15} and 2^{3}). Similar procedure was also adopted for parameter ε, while parameter C was considered equal to 3 (Cortez, 2010).

$$K(x, x') = exp(-\gamma \|x - x'\|^2), \gamma > 0 \tag{3.6}$$

3.2.1.3 Rminer tool

Nowadays, there are several tools that allow an easy application of DM algorithms with a limited knowledge of the mathematical background required for its implementation. In this work, the rminer library (Cortez, 2010) of the R Statistical Environment (R, 2012) was adopted, since it is particularly suited for generating ANN and SVM data-driven models.

Among the several features included in rminer, in this work the functions *mining*, *fit* and *predict* were used. For simplicity, the functions will be described using a parallel with a simple regression model.

The function *fit* allows finding an analytical expression in the form $y = mx + b$ with m and b adjusted to the database in analysis.

Having the expression calibrated, *predict* gives the results (y) for new values of the independent variable (x) by replacing it in the expression found by *fit*.

The function *mining* is a more sophisticated one. It performs several runs (i.e., sequences of *fit* and *predict* executions) under a user selected validation method. It is important to emphasize that, while *fit* uses the entire database to adjust a model, *mining* only uses part of it, being the fitted model tested in unseen data (i.e., test set). This aspect is very important since it allows evaluating the performance of the adjusted model when applied to new data (depending on the validation method), thus measuring the true generalization capacity of the DM model. In this work, a holdout split validation method was adopted, in which 2/3 of the data entries were randomly selected as training data

and the remaining 1/3 samples were used as test data.

Another important difference is that only *fit* function allows storing a model that can be then used, like an analytical expression, to perform new predictions. In fact, depending on the chosen division of sets and number of runs, for example, *mining* function can produce a huge number of models. For practical reasons, the rminer library does not store any of these models.

3.2.2 Data mining analyses

A total of eight DM analyses were performed for each database, as shown in Table 3.3. Firstly, two types of analyses, denoted A and B, were considered. In Type A analysis, the input variables were defined based on the formulations of ACI and SA guidelines. In Type B analysis the input variables were estimated during the analysis by an automatic selection process (RM) or by combining that with expert judgement (USER). This resulted in 4 sets of input variables. For each set of input variables, models using both ANN and SVM algorithms were generated. The next paragraphs detail each of these analyses.

Table 3.3: Summary of the DM analyses performed.

Database	**Type A (Input variables known *a priori*)**		**Type B (Input variables unknown *a priori*)**	
	Input variables	**DM algorithm**	**Input variables**	**DM algorithm**
DPT	ACI	ANN SVM	RM	ANN SVM
	SA	ANN SVM	USER	ANN SVM
BPT	ACI	ANN SVM	RM	ANN SVM
	SA	ANN SVM	USER	ANN SVM

Analyses Type A were conducted assuming for DM models the same input variables as used by the guidelines' models. Hence, one analysis used the input variables considered by ACI (L_b, p_f, A_f, f_{fu}) while the other used those from SA (L_b, A_f, f_{fu}, d_g, b_g, E_f, f_c). This allowed the direct comparison between the performance of DM and guidelines' models.

Each analysis of Type A consisted on running *mining* function over each database. A total of 20 runs were imposed being the database divided in four random sets of equal size (3 for training and 1 for testing). Then the prediction error metrics fluctuation was

analysed in order to check generalization capacity of each DM algorithm. To this purpose, the 95% t-Student confidence interval was adopted. Finally, the error metrics obtained in all the 20 runs were averaged to allow comparisons between model's accuracy.

In analyses Type B, it was assumed that the input variables were not known *a priori*. Hence, besides the four and seven variables used by ACI and SA, respectively, all the numeric variables present in more than 2/3 of the records in each database were also included. This resulted in more than 20 input variables available on each database at the beginning of the calibration process.

The same procedure used in the analyses Type A was used for these new and larger databases. In the end of the *mining* sequence, a sensitivity analysis was performed in order to identify the most important variables in a backward selection procedure. After identifying the most important variables, the procedure was repeated with the limited input variables. This process was carried out several times, being the number of input variables successively reduced. In the end, a final set of input variables could be proposed as well as the DM models using those input variables.

Since this sensitivity analysis is influenced by the representativeness of each variable in the database, in some cases the final set of variables was found to be meaningless for design purposes. Hence, a different type of models was generated, taking into account the evolution of the variable's importance in the sensitivity analysis and also including all the variables thought meaningful for design.

Since in the first case the variables were chosen taking into account only the rminer sensitivity analysis, these were designated by RM. In the second case, since the choice was made by the user, the designation USER was adopted instead.

Finally, it should be emphasized that all the analyses carried out used the maximum pullout force (F_{fmax}) as the only output variable. Also, in all the analyses, variables normalization was considered using a zero mean and one standard deviation transformation for all input and output variables (-1 to 1 scale). Then, the inverse procedure was performed for the output variable in order to export it in its original scale.

3.2.2.1 Results and analysis

For each analysis three error metrics were calculated, namely, the Mean Absolute Error (MAE), the Root Mean Squared Error (RMSE) and the Squared Correlation Coefficient (R^2). Both MAE and RMSE were already introduced in Equations 3.1 and 3.2, respectively.

The R^2 is defined in Equation 3.7 in which the parameters with an upper bar, represent the average value of the corresponding parameter.

$$R^2 = \left[\frac{\sum_{i=1}^{N} \left[\left(F_{fmax,Exp}\right)_i - \overline{\left(F_{fmax,Exp}\right)_i} \right] \left[\left(F_{fmax,Num}\right)_i - \overline{\left(F_{fmax,Num}\right)_i} \right]}{\sqrt{\sum_{i=1}^{N} \left[\left(F_{fmax,Exp}\right)_i - \overline{\left(F_{fmax,Exp}\right)_i} \right]^2 \sum_{i=1}^{N} \left[\left(F_{fmax,Num}\right)_i - \overline{\left(F_{fmax,Num}\right)_i} \right]^2}} \right]^2 \quad (3.7)$$

Analyses Type A

Tables 3.4 and 3.5 present the average error metrics (MAE, RMSE and R^2) obtained in the 20 runs of *mining* function performed for all the analyses with DPT and BPT databases, respectively. Those metrics include, in parenthesis, the correspondent 95% t-Student confidence intervals to allow verifying the stability of the predictions.

Figure 3.7 illustrates the geometrical variables included in the referred tables in order to ease interpretation of the results.

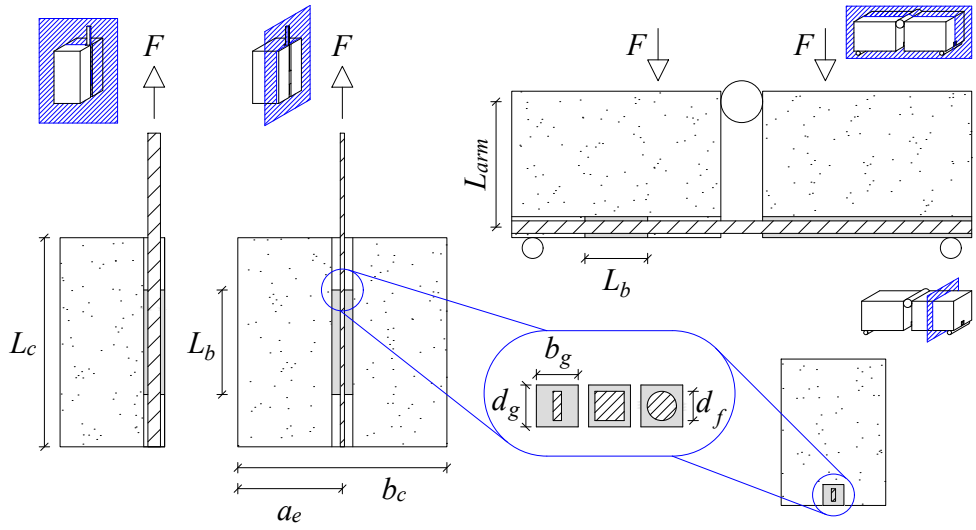

Figure 3.7: Variables of DPT (left) and BPT (right) involved in the DM analyses.

For all the analyses presented, it was found that they are quite stable and capable of being used in unseen data since they presented simultaneously low errors and low dispersion values along the 20 runs performed on different data sets as shown by the low values of 95% t-Student confidence intervals obtained.

Additionally, these tables also include the same error metrics obtained when applying to each database ACI and SA formulations, as defined in each guideline. Note that the number of specimens considered was not the same in all the analyses. This number depends on the input variables required in each analysis, which were not always available in the databases because the authors of the corresponding experimental tests did not provide them. Nevertheless, the analyses can still be compared since the same number of specimens was used for each group of analyses using the same input variables.

Table 3.4: Average error metrics obtained after 20 runs of *mining* function in the DPT database (best values in **bold**).

Inputs origin	**Type A**						**Type B**			
	ACI			**SA**			**RM**		**USER**	
Input variables	L_b, p_f, A_f, f_{fu}			L_b, A_f, f_{fu}, d_g, b_g, E_f, f_{cm}			L_b, A_f, b_c, L_c, d_g, ε_{fu}		L_b, p_f, f_{at}, ε_{fu}, p_g, a_e, f_{cm}	
Model	ACI[1]	ANN	SVM	SA[2]	ANN	SVM	ANN	SVM	ANN	SVM
MAE [kN]	14.85	10.10 (±0.14)	**9.82 (±0.12)**	11.56	7.92 (±0.16)	**7.07 (±0.11)**	**5.64**	5.75	6.14	**5.70**
RMSE [kN]	19.34	15.38 (±0.29)	**14.93 (±0.20)**	15.16	11.52 (±0.27)	**10.67 (±0.16)**	8.60	**8.17**	8.71	**8.22**
R^2 [-]	0.58	0.82 (±0.01)	**0.83 (±0.01)**	0.53	0.80 (±0.01)	**0.83 (±0.01)**	0.89	**0.90**	0.88	**0.89**
Specimens [-]		363			286				208	

Note: The values in parenthesis are the correspondent 95% t-Student confidence intervals.
[1] Analysis according to ACI guideline formulation (see Table 3.1).
[2] Analysis according to SA guideline formulation (see Table 3.2).

Table 3.5: Average error metrics obtained after 20 runs of *mining* function in the BPT database (best values in **bold**).

Inputs origin	**Type A**						**Type B**			
	ACI			**SA**			**RM**		**USER**	
Input variables	L_b, p_f, A_f, f_{fu}			L_b, A_f, f_{fu}, d_g, b_g, E_f, f_{cm}			L_b, ε_{fu}, L_{arm}, f_{ctm}, E_{cm}, E_f, d_f		L_b, ε_{fu}, L_{arm}, f_{ctm}, d_f, f_{ac}	
Model	ACI[1]	ANN	SVM	SA[2]	ANN	SVM	ANN	SVM	ANN	SVM
MAE [kN]	10.65	**3.98 (±0.17)**	4.63 (±0.31)	7.18	**3.18 (±0.26)**	3.62 (±0.16)	**3.62**	3.67	3.56	3.56
RMSE [kN]	13.56	**5.51 (±0.26)**	6.94 (±0.39)	8.90	**4.42 (±0.56)**	5.54 (±0.23)	**4.86**	5.10	**4.76**	4.97
R^2 [-]	0.43	**0.88 (±0.01)**	0.80 (±0.03)	0.62	**0.92 (±0.02)**	0.88 (±0.01)	0.88	0.88	**0.89**	0.88
Specimens [-]			68					56		

Note: The values in parenthesis are the correspondent 95% t-Student confidence intervals.
[1] Analysis according to ACI guideline formulation (see Table 3.1).
[2] Analysis according to SA guideline formulation (see Table 3.2).

Comparing the analyses Type A (using ACI and SA input variables) it can be seen that, for both databases, the worst results (higher MAE and RMSE and lower R^2) were obtained by the guidelines. As already verified in section 3.1, SA presents better performance than ACI even though its R^2 value is lower.

In terms of DM models, for both databases, using SA input variables attained better results than using ACI input variables.

Regarding DPT database, when ACI input variables are used, MAE and RMSE of both DM models (ANN and SVM) are at least 20% lower while R^2 is at least 40% bigger, when compared to the same metrics obtained using ACI guideline.

When SA input variables are used, MAE and RMSE of both DM models (ANN and SVM) are at least 24% lower while R^2 is at least 50% bigger, when compared to the same metrics obtained using SA guideline.

In the case of BPT database, the improvement in the results is even bigger. The major difference when compared with the results of DPT database, is the fact that the error metrics are almost the same in both analyses Type A and B. This means that the improvements achieved with the DM models obtained in analyses Type B were lower for BPT database.

Analyses Type B

For analyses Type B, the first result to be considered is the importance of each variable in the prediction of the bond strength. In Tables 3.4 and 3.5, these variables are presented by decreasing order of importance. Further discussion about this will be given in following paragraphs.

A common aspect for both databases is that all analyses Type B presented better results than those from the guidelines, being the best results obtained using SVM and ANN algorithms for DPT and BPT databases, respectively. When compared with ACI guideline results, the three metrics of all four DM models are at least 50% better. When compared with SA guideline results, the three metrics of all four DM models are at least 40% better. In both cases, better means that MAE and RMSE are lower while R^2 is higher.

In the case of DPT database, the RM input variable's selection, lead to the inclusion, as input variable, the concrete block length (L_c – see Figure 3.7). However L_c is not relevant from a design viewpoint. On the other hand, RM selection did not included any input variable related with concrete nor adhesive mechanical properties. Hence, USER selection process, which took into account both importance and relevance of each variable, proposes a different set of input variables where adhesive and concrete mechanical properties are

also represented. Analysing the error metrics, it can be seen that RM analyses are slightly better. However, taking into account that USER input variables are more reasonable to be used, the error metrics are still acceptable.

In the case of BPT database, the major difference between RM and USER input variables is related with the removal of FRP modulus of elasticity (E_f) and the inclusion of adhesive compressive strength (f_{ac}). The former was removed since there was already a more important variable related with FRP mechanical properties, namely, the FRP ultimate strain (ε_{fu}) as shown in Figure 3.8c. In order to have the adhesive mechanical properties represented f_{ac} was included. Regarding the error metrics, USER analyses attained better results.

The relative importance of each input variable obtained in all analyses Type B is summarized in Figure 3.8. Comparing the relative importance of each variable when the RM input variable's selection is used, the results differ between DPT and BPT databases. In DPT (Figure 3.8a), since the geometric variables appear in larger number, it seems that the geometry of specimen and the configuration of the strengthening have more impact in the predictions than the mechanical properties of the involved materials. In BPT (Figure 3.8c), both geometric and mechanical parameters appear in the same number.

Another interesting aspect is related with the variables' interaction that was found during the process of selecting the input variables. For example, considering the importance ranks depicted in Figure 3.8a and 3.8b it can be seen that, besides L_b, there is no other common variable in the two figures. However, as referred above, the only actions taken when moving from RM to USER analysis, were the removal of L_c and the addition of f_{at} and f_{cm}. But when the sensitivity analysis was re-run, using the new set of variables, it was found that p_f, p_g and a_e were more important than their equivalents in RM set, i.e. A_f, d_g and b_c, respectively a variable referring to FRP geometry, groove geometry and location of the NSM FRP system in the concrete element. This suggests that there is interaction between variables which is the reason why the final set of variables suggested by the USER (Figure 3.8b) is completely different from RM final set (Figure 3.8a).

3.2.2.2 Using data mining models

As referred before, the analyses carried out using *mining* function do not allow storing a prediction model. Hence, the final DM models to be proposed were obtained by running *fit* function over each entire database. Since those final models were intended to be made available in the website that stores the databases (see section 2.5.1), where also ACI and SA guideline formulations can be easily applied, only DM models using those guidelines input variables were generated. Hence, those willing to compare the maximum

pullout force (F_{fmax}) obtained in their pullout tests, just need to provide ACI and SA input variables and specify the type of test they are comparing with. Then, by clicking the "Calculate" button available in the website's page, six values of F_{fmax} prediction are obtained. The first two predictions correspond to the guidelines ACI and SA (the step-by-step calculation procedure can also be seen). The remaining four predictions correspond to those obtained by DM models. Two correspond to the two DM models based on ANN algorithm using either ACI or SA input variables. The last two predictions are identical to the former two, but are based on SVM algorithm instead.

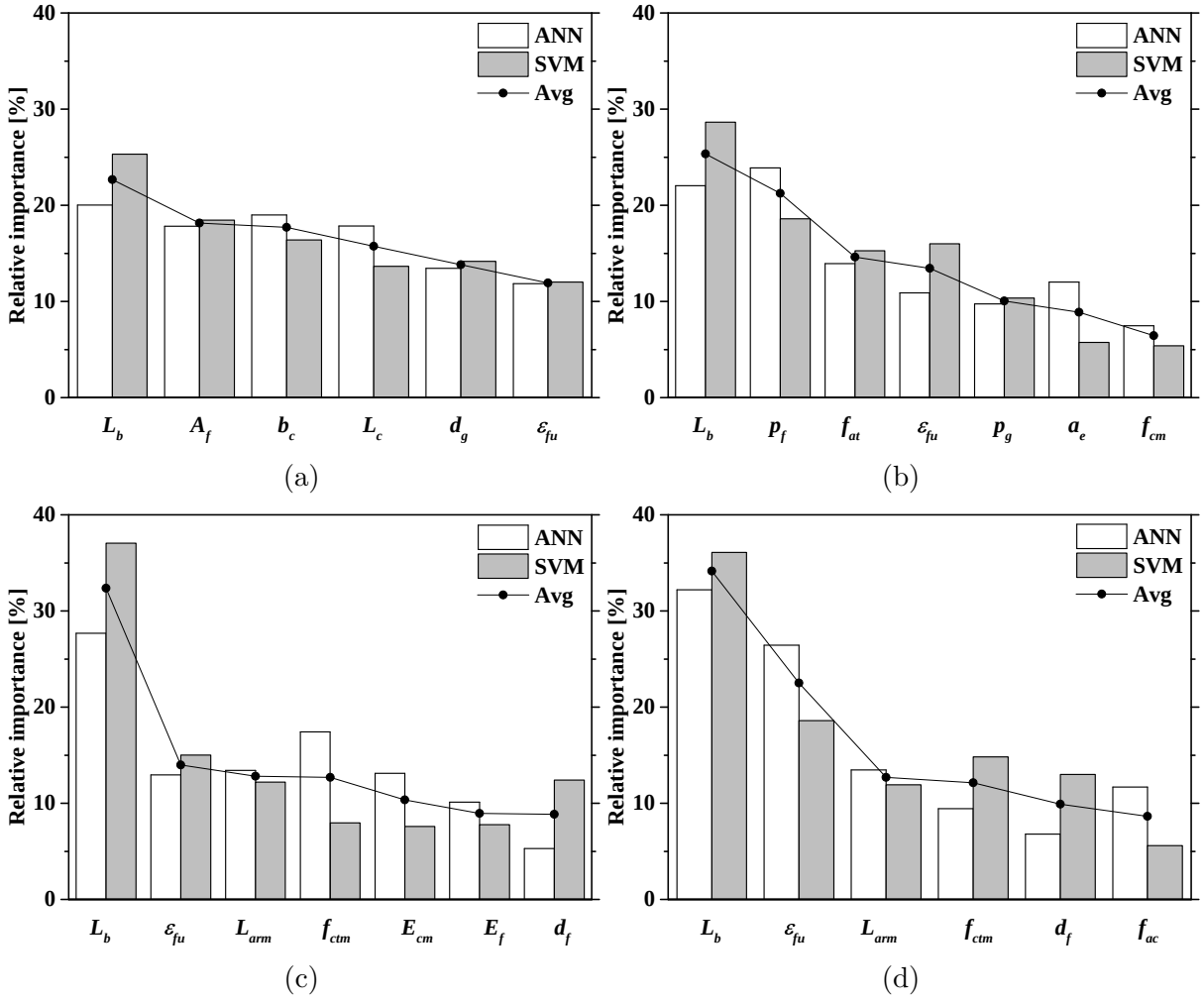

Figure 3.8: Relative importance of each input variable in the analyses Type B (database + input variables): (a) DPT + RM; (b) DPT + USER; (c) BPT + RM; (d) BPT + USER.

Figure 3.9 presents an example of a prediction run in the website. Note that the experimental value of that example was 20.4 kN. As can be seen, except for the DM model using ANN and ACI input variables, all the other three DM models presented

lower errors than those obtained by both ACI and SA guidelines formulations.

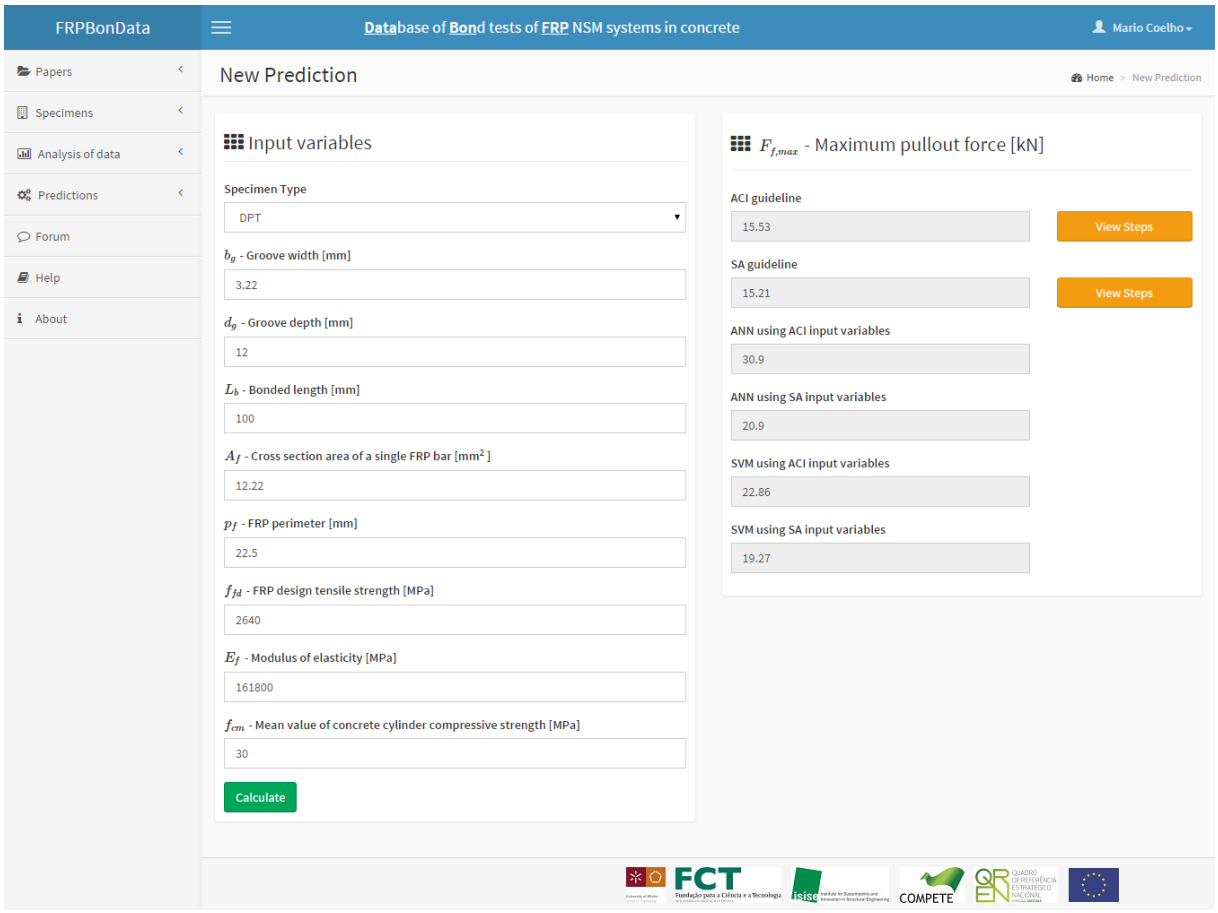

Figure 3.9: Maximum pullout force prediction calculated in the website developed.

Table 3.6 presents the error metrics for these final four models for both DPT and BPT databases. As it can be seen, the error metrics of these models are even lower than all the corresponding analyses presented so far. This is mainly related with the fact that *fit* function uses the entire database to adjust a model while in all the analyses with *mining* function only 3/4 of each database were being used for models adjustment.

To ease the comparison between ACI and SA guidelines and DM models prediction capability, Figure 3.10 presents the relationship between experimental and predicted pullout force obtained when each DM model (included in Table 3.6) and ACI and SA guidelines are applied. As it can be seen the clouds of points related with the use of the guidelines models are larger than those of the DM models, revealing higher dispersion of the predictions.

In the importance charts presented in Figure 3.8 the bonded length (L_b) was always found to be the most important variable in the prediction of the maximum pullout force. Hence, L_b was selected to assess the stability of the predictions obtained by each model.

Table 3.6: Error metrics for the final models obtained by fitting DM algorithms to each entire database (best values in **bold**).

Inputs origin	**ACI**				**SA**			
Input variables	L_b, p_f, A_f, f_{fu}				L_b, A_f, f_{fu}, d_g, b_g, E_f, f_{cm}			
Database	DPT		BPT		DPT		BPT	
Model	ANN	SVM	ANN	SVM	ANN	SVM	ANN	SVM
MAE [kN]	7.36	**6.93**	1.87	**1.53**	**3.78**	3.87	1.10	**0.62**
RMSE [kN]	10.77	**10.26**	2.50	**2.49**	**5.61**	5.77	1.48	**1.12**
R^2 [-]	0.84	**0.86**	0.95	0.95	**5.61**	0.91	0.98	**0.99**
Specimens [-]	363		68		286		68	

Figure 3.11 presents the relationship of the ratio between the quantities plotted in Figure 3.10, i.e. maximum pullout force predicted by each model ($F_{fmax,Num}$) and that obtained in the experimental tests ($F_{fmax,Exp}$), versus the bonded length. This figure allows to see that the guidelines' models performance is influenced by L_b, producing safe results for lower values of L_b and results successively more unsafe as L_b increases. Contrarily, this ratio for DM models is almost constant, revealing that the performance of DM models is not influenced by the variation of L_b.

In order to show the generalization capability of the proposed DM models, Figure 3.12 presents variable effect characteristic (VEC) curves (Cortez and Embrechts, 2013; Çevik et al., 2015) for bonded length, L_b. These curves reproduce the influence of L_b in the predictions, as it changes from its minimum to its maximum value in each database. The VEC curves were obtained by dividing, in each database, the range of L_b into several parts. Then, all the final DM models included in Table 3.6, as well as both ACI and SA guidelines, were applied using each value of L_b and the average values of all the remaining variables required by each model.

As can be seen, in terms of ACI and SA guidelines predictions, Figure 3.12b is just a zoom of Figure 3.12a, due to the smaller range of L_b values available in BPT database. If ACI and SA curves in both figures were overlapped, they will coincide, since the same variables were applied for both DPT and BPT databases. These curves show that using SA guideline the "average specimen" (fictitious specimen with all parameters on their average value) has a development length, L_d, of about 270 mm. Such threshold L_d was not predicted by ACI guideline.

Analysing DM models predictions, two main conclusions can be drawn. The first is that, except for the model SVM_ACI (using SVM algorithm and ACI input variables) in Figure 3.12a, all other DM models in both figures present either ACI or SA guidelines' trends. Secondly, for those DM models that captured L_d, for values of L_b greater than L_d,

the maximum pullout force (F_{fmax}) remained almost constant, as it should be. These two conclusions show that the DM models developed herein have the required generalization capacity.

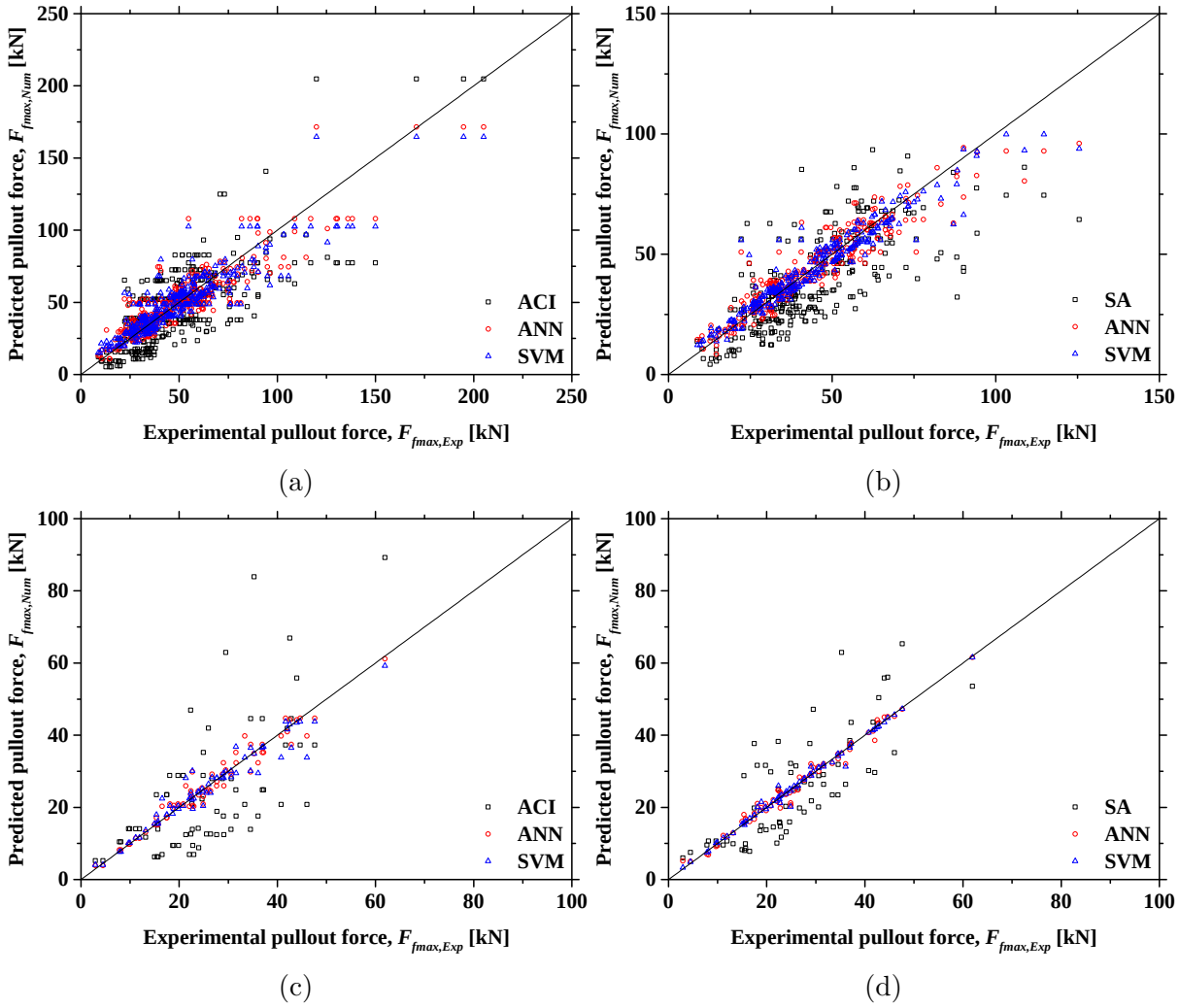

Figure 3.10: Experimental *versus* predicted pullout force for the final models obtained by fitting DM algorithms (database + input variables): (a) DPT + ACI; (b) DPT + SA; (c) BPT + ACI; (d) BPT + SA.

3.3 Conclusions

In the present chapter mechanical models to estimate bond strength of NSM FRP systems in concrete were analysed. This included the mechanical models proposed in ACI and SA guidelines, as well as alternative mechanical models based on DM algorithms.

The former were analysed with two main goals: (i) validate their accuracy using a database of pullout tests larger than that existing at the time they were developed; (ii)

propose improvements or at least recalibrate them using the referred larger database. From this analysis, the following major conclusions can be drawn:

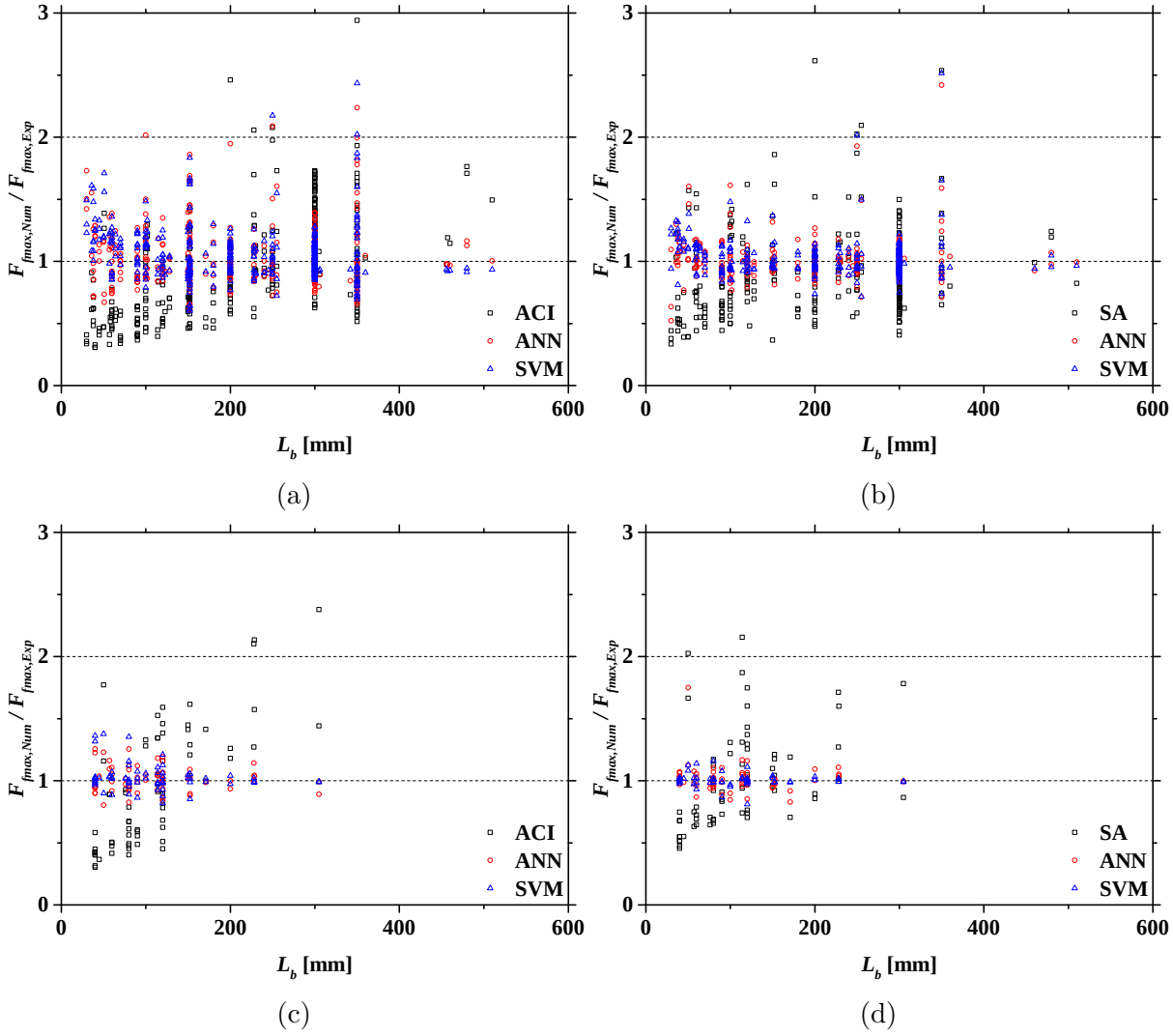

Figure 3.11: Variation of the ratio between experimental and predicted pullout force with the bonded length (database + input variables): (a) DPT + ACI; (b) DPT + SA; (c) BPT + ACI; (d) BPT + SA.

- the ACI and SA guidelines need to be upgraded with new features in order to become more accurate. In this chapter, a proposal considering different expressions for different FRP cross-sections seemed to improve the accuracy of ACI and SA. In fact, experimental results show that different FRP cross-sections behave differently, both in terms of stress transfer and failure modes. In addition, there are failure modes which are not explicitly accounted for in these two formulations. This gap should also be bridged in the future;

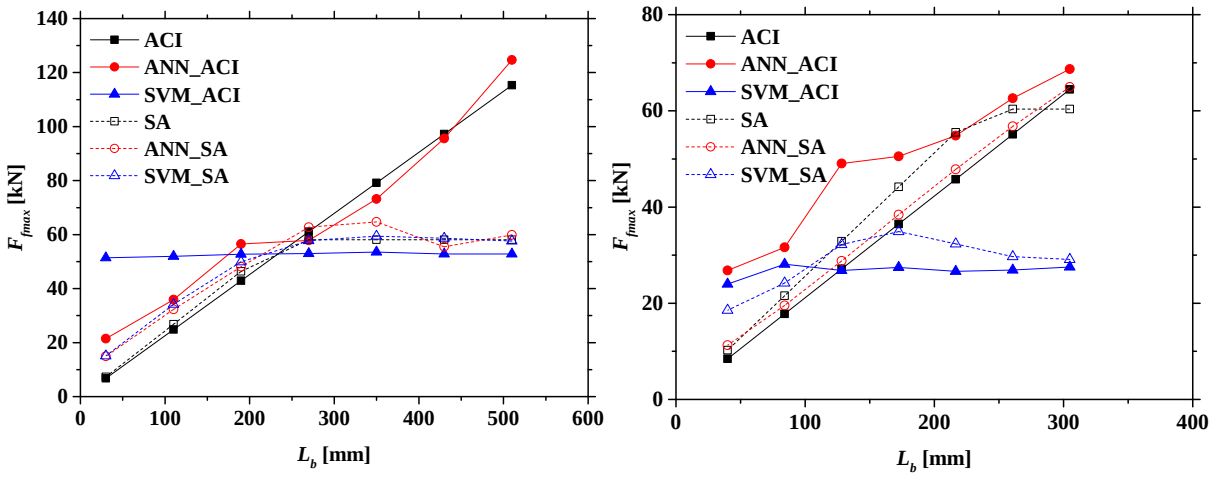

Figure 3.12: VEC curves for L_b considering (a) DPT or (b) BPT databases. Note: composite designations include the DM model and the type of input variables, as defined in Table 3.6.

- regarding SA formulation, it was verified that it can be extended to quadrangular and round bars by considering that the failure perimeter is 1 mm from the groove, rather than 1 mm from the FRP as SA establishes. However, further improvements are still necessary since the predictions for FRP rectangular bars are significantly better than those obtained for round bars;

- a common trend verified in the first analyses (A1) of both guidelines (ACI/SA) and both databases (DPT/BPT), i.e. the analyses according to each guideline, is that the amount of points below the 45 degree line in the charts is in general greater, i.e. the guidelines' predictions tend to be conservative. Contrarily, the remaining analyses tend to present a similar amount of predictions in both sides of that line. Even though this may indicate that the suggestions left in this work are less safe than the ones proposed by the guidelines, those are actually more correct. In fact, considering the philosophy presented in the Eurocodes (CEN, 2002), a prediction model should predict a phenomenon on its average being the model's safety provided by safety factors to obtain then. Hence, no safety features should be included in the prediction model. In this scenario, the amount of points in both sides of 45 degree line should be almost 50%.

In addition, alternative DM mechanical models were proposed. The development of those models also allowed to understand the influence of some important variables in the bond behaviour of NSM FRP systems in concrete. At the end, the following major

conclusions can be drawn:

- regarding analyses Type A (using the input variables suggested by ACI and SA guidelines), a direct comparison between the predictive capacity of guidelines models and DM models using the same input variables showed that all DM models performed better than the equivalent guidelines models;
- regarding analyses Type B (using sets of input variables suggested in this work), it was proved that the maximum pullout force in NSM FRP bond tests could be better predicted if a set of input variables different from those adopted by the guidelines is used;
- the sensitivity analyses conducted to choose the new input variables can lead to include variables that are not relevant for design, thus it was necessary to replace some input variables by other thought more significant. However, the impact in the predictive capacity of the DM models with this new set of input variables was quite low, thus there can be obtained DM models more suitable for design yet maintaining high accuracy;
- the guidelines models predictive capacity seems to be influenced by the value of the bonded length. Contrarily, the predictive capacity of the final DM models was found to be independent from this important variable;
- the generalization capacity of the proposed DM models was demonstrated. For this purpose, the bonded length was selected to conduct the parametric studies. These studies proved that the DM models are in agreement with the guidelines, thus they have the required generalization capacity;
- in order to spread and encourage the use of DM in this research field, the best DM models obtained herein were made available in an website built for that purpose. Only DM models using the same input variables as used in the analysed guidelines were considered.

This page was left blank intentionally.

CHAPTER 4

Bond strength of NSM FRP systems in concrete: design models

As shown in the previous chapters, despite the progress that has been made in the past years, design formulations to safely apply NSM FRP systems in the strengthening of concrete structures are still incipient. On one hand, there are no European guidelines for NSM FRP systems, even though the draft version of the new annex of EN 1992-1-1 (Eurocode 2: Part 1-1) (CEN, 2004) refers to NSM FRP systems. On the other hand, the formulations to estimate the bond strength of NSM FRP systems included in both ACI (ACI, 2008) and SA (SA, 2008) guidelines are not consistent with the partial safety factors framework (see Section 2.4).

Hence, this chapter presents a solution supported in the database of pullout tests presented in Section 2.5. It consists on a modification of ACI and SA formulations to, consistently with the partial safety factors methodology, yield designs with acceptable reliability indexes.

The philosophy behind the partial safety factors method recognizes that not all designers should be familiar with reliability concepts which, in any case, must be followed in order to have safe structures. In the partial safety factor method, both actions and resistances are considered by their nominal values multiplied and divided, respectively, by partial safety factors. The way those partial factors are derived is responsible for introducing the reliability component into design. This means that, even without knowing, designers are indeed considering reliability in their projects. This philosophy is transversal to all Eurocode (EC) thus, no matter what type of structure is being designed, the corre-

spondent EC includes a set of partial factors to take into account the required reliability for all the design situations, designated as limit states, foreseen in that EC.

The Eurocode 0 (EC0) (CEN, 2002) describes in detail the background to the calibration of partial safety factors and the reliability analysis and targets used. Those are summarized in the next section.

4.1 Partial safety factors method

The objective of the partial safety factors method is to design structures resulting in a safety level, quantified by the reliability index, acceptable for society and similar for all types of structures. In the Eurocodes, for structures with a normal class of consequences, the target reliability index is defined equal to 3.8 for a fifty years reference period.

The reliability index is given by Equation 4.1, where R is the resistance of the structure and E is the effect of actions. This probability can be computed using the first order reliability method (FORM). The reliability index is defined as the distance between the design point (i.e., the most likely failure point) and the origin in the normalized space, as shown in Figure 4.1.

$$\beta = -\Phi^{-1}(p_f) = -\Phi^{-1}(P(R - E < 0)) \tag{4.1}$$

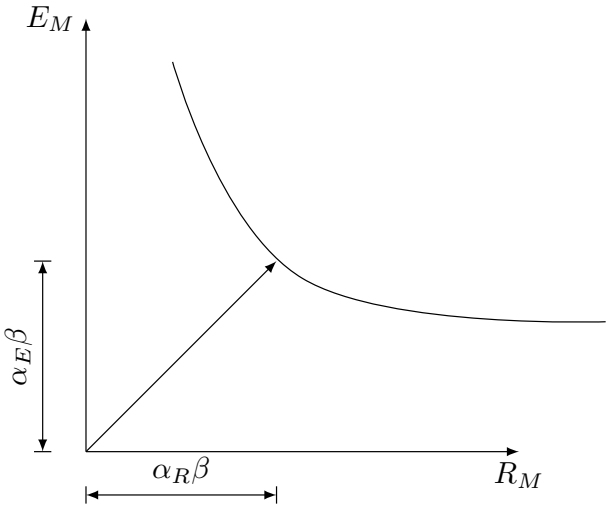

Figure 4.1: Design point and reliability index in the normalized space according to FORM.

For a design corresponding to the lowest admissible value of the reliability index, the design point has coordinates $(-\alpha_R\beta; -\alpha_E\beta)$ in the normalized space. The corresponding resistance in the original space is such that $P(R = R_d) = \Phi(-\alpha_R\beta)$.

Although the values of the cosines α vary from design to design, a value of $\alpha_R = 0.8$ usually leads to acceptable results. Consequently, the design value of the resistance, R_d, can be computed according Equation 4.2.

$$P\left(R = R_d\right) = \Phi\left(-\alpha_R \beta\right) = \Phi\left(-0.8 \times 3.8\right) \tag{4.2}$$

Once the probabilistic distribution of R is found, Equation 4.2 can be used directly to compute the design point and, afterwards, to define partial safety factors that result in this design strength.

In the context of the present work, the partial safety factors method was adopted to calibrate ACI and SA formulations for predicting NSM FRP systems bond strength, using the database of direct pullout tests introduced in Section 2.5. To do that, the following main tasks were conducted:

(i) classify the specimens according their observed experimental failure mode and apply the corresponding theoretical limit state resistance function (R_t) to each specimen;

(ii) for each specimen, estimate the error (δ) of the theoretical resistance function using Equation 4.3, where R_e is the experimental resistance value. Then, adjust a probabilistic distribution to the theoretical resistance function errors obtained for all specimens;

$$\delta = R_e / R_t \tag{4.3}$$

(iii) compute the distribution of the probabilistic resistance function (R) defined in Equation 4.4. If the only random variable in that function is the theoretical resistance function error, its probabilistic distribution can be estimated analytically. Otherwise, Monte Carlo simulation can be used to estimate the joint probabilistic distribution of all the random variables present in the probabilistic resistance function;

$$R = R_t \delta \tag{4.4}$$

(iv) compute the design value of the limit state resistance function (R_d). This should be obtained in order to have a probability of failure as defined in Equation 4.5. In Equation 4.5, α_R is the first order reliability method sensitivity factor for resistance and β is the reliability index. In this work those parameters were taken as 0.8 and 3.8, respectively, according to EC0 (CEN, 2002) suggestion;

$$P\left(R = R_t \delta \leq R_d\right) = \Phi\left(-\alpha_R \beta\right) \tag{4.5}$$

(v) rewrite the resistance function in its design form and define the safety factors to be included. This should be done taking into account that some variables are common to other applications foreseen in the EC and are expected to maintain the same partial safety factors throughout the EC;

(vi) replace (iv) in (v) and calibrate the values of the safety factors defined in the previous step.

The method explained above is similar to the generic approach of the design assisted by testing method, defined in the EC0 (CEN, 2002). The main difference between them is that the method presented herein uses the probabilistic models of all the random variables, which can be of any type, and Monte Carlo simulations to achieve the joint probabilistic distribution of the limit state resistance function in analysis. Contrarily, the design assisted by testing method defined in the EC0 is designed for resistance functions with normal and lognormal random variables which can be handled analytically.

The design assisted by testing method has already been successfully used in the context of the Externally Bonded Reinforcement (EBR) technique (Monti and Santini, 2002; Monti et al., 2009; Bilotta et al., 2011b, 2013). However, according to author's best knowledge, the present thesis presents the first attempt of applying it to calibrate the reliability parameters of the bond strength resistance functions suggested by ACI and SA, including the resistance models errors. In the following sections, the major details of the application and the obtained reliability parameters are presented.

4.2 Data and models

As previously mentioned in Section 2.5.2.11, even though not always clear, the authors of the Direct Pullout Tests (DPT) presented a single critical experimental failure mode. Contrarily, in Beam Pullout Tests (BPT), the authors normally provided several failure modes based on the final appearance of the tested specimen.

Since the failure mode needs to be clearly identified in the reliability analyses, only DPT were used in the following. Moreover, since the amount of tests using carbon FRP (CFRP) with rectangular cross-section is larger than the other types of FRP fibres/cross-sections, it was decided to conduct the reliability analysis considering rectangular CFRP bars only.

This resulted in a group of 128 specimens from the total 363 available on the DPT database. Despite the reduced amount of specimens used, all the possible five local failure modes were found: 32 specimens with FRP tensile rupture (F), 50 specimens with concrete

cohesive failure (C), 10 specimens with adhesive cohesive failure (A), 19 specimens with FRP/Adhesive interface failure (F/A) and 17 specimens with Adhesive/Concrete interface failure (A/C).

Besides the original ACI and SA guidelines' formulations (presented in Section 2.4), in the reliability analysis conducted, the improved versions of the guidelines formulations (presented in Section 3.1) were considered. Namely, for ACI two improvements were suggested that consist on replacing the constant value of 6.9 MPa for the average bond strength (τ_{avg}) with: (i) the calibrated constant value of 9.25 MPa (see analysis A2 in Figure 3.1b); and, (ii) the expression given by the ratio between FRP cross-section area (A_f) and the FRP to adhesive contact area (see analysis A3 in Figure 3.1b). This latter formulation, using τ_{avg} as an expression, will be designated as "ACI modified" in what follows.

Regarding SA, the suggested improvement resulted from recalibrating the expressions of its original formulation.

4.2.1 Material probabilistic models

In order to conduct a reliability analysis it is necessary to define the probability distribution of all random variables. Three different probability distributions were considered in this work, namely, normal (N), lognormal (LN) and Weibull (W); in what follows they are presented as N,LN(mean; standard deviation) and $W(\alpha;\beta)$, respectively. In Weibull distribution α is the scale parameter and β is the shape parameter.

It was considered that all the geometric parameters were deterministic, following the EC practice, while all mechanical parameters were considered as random variables. As shown in Section 2.4, ACI and SA formulations together require only three mechanical parameters, namely, FRP modulus of elasticity (E_f) and tensile strength (f_{fu}) and concrete compressive strength (f_c).

The probabilistic models for the first two parameters were obtained from the literature (Gomes et al., 2013). For both E_f and f_{fu} they consist of Weibull distributions as shown in equations 4.6 and 4.7, respectively.

$$E_f \sim W\,(26.2; 180.9)\ \text{GPa} \tag{4.6}$$

$$f_{fu} \sim W\,(15.9; 2777)\ \text{MPa} \tag{4.7}$$

Regarding f_c, the adopted probabilistic model consisted on a lognormal distribution with 6% coefficient of variation, adapted from JCSS (2001), as shown in Equation 4.8. This distribution depends on the concrete class, thus the analyses were conducted taking

into account the concrete mean compressive strength of each specimen according to the concrete classes defined in EC2 ($f_{cm,EC2}$) (CEN, 2004).

$$f_c \sim LN\left(f_{cm,EC2}; 0.06 f_{cm,EC2}\right) \text{MPa} \tag{4.8}$$

4.2.2 Probabilistic uncertainty for mechanical bond strength models

The uncertainty associated with the mechanical bond strength models, considered as a random variable, was defined by comparing the experimental maximum pullout force and the corresponding prediction according ACI and SA formulations.

Considering the mechanical bond models defined in Section 2.4, it can be seen that, for both ACI and SA guidelines, the theoretical limit state function associated with the FRP rupture (F) is defined by Equation 4.9. This function was applied to the 32 specimens available in the database which presented FRP rupture failure mode.

$$R_{F(ACI/SA)} = A_f f_{fu} \tag{4.9}$$

Regarding ACI formulation, the remaining failure modes are all grouped in the debonding limit state (B). To obtain its theoretical function, the second branch of ACI formulation was firstly re-written by replacing L_d and τ_{avg} in F_{fmax} expression (see Equation 2.2), resulting in Equation 4.10. This expression was applied to the remaining 96 specimens.

$$R_{B(ACI)} = 6.9 L_b p_f \tag{4.10}$$

Regarding SA formulation, the theoretical limit state functions associated with concrete cohesive failure (C) and debonding failures (B) were also obtained by re-writing the expressions presented in Section 2.4.2 yielding to Equations 4.11 and 4.12, respectively. According to the failure modes distribution referred before, these functions were applied to 35 and 39 specimens, respectively.

$$R_{C(SA)} = \sqrt{0.73 \varphi_{per}^{0.5} f_c^{0.67} L_{per} E_f A_f} \tag{4.11}$$

$$R_{B(SA)} = \frac{2L_b}{\pi}\left(0.8 + 0.078\varphi_{per}\right) L_{per} f_c^{0.6} \tag{4.12}$$

In addition to ACI and SA formulations, Equation 4.13, corresponding to the ACI modified formulation referred before, was also used. It was applied to the same 96 specimens as Equation 4.10.

$$R_{B(ACI\ modified)} = 162\left(\frac{A_f}{p_f L_b}\right)^{0.55} L_b p_f \tag{4.13}$$

The expressions presented above, were applied to the corresponding specimens and the prediction errors were estimated as the ratio between experimental ($F_{fmax,Exp}$) and numerical ($F_{fmax,Num}$) pullout forces. Then, a probability distribution was fitted to the errors associated with each limit state.

Figure 4.2 presents the probability distributions obtained for all limit state functions errors. The caption of each distribution includes also the corresponding probability parameters. It can be seen that, except for FRP rupture limit state, all other limit state errors were better fitted by lognormal distributions. This is due to the asymmetry of the frequencies observed and the need to guarantee a null probability of negative values for large coefficients of variation.

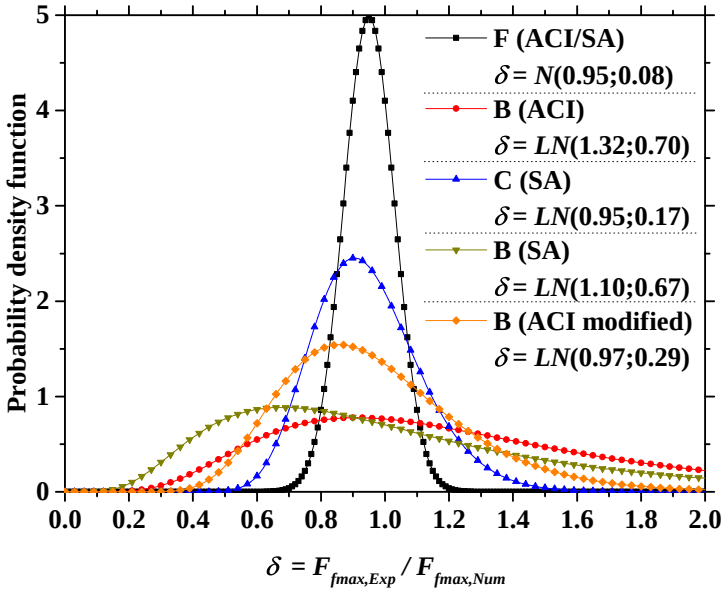

Figure 4.2: Probability density function of the error δ associated with each limit state theoretical resistance function.

The coefficients of variation associated with the errors probability distributions were 8%, 53%, 18%, 61% and 30% for the limit states defined in equations 4.9 to 4.13, respectively. Those are considerably high when compared with the coefficients of variation for the materials models which were 5%, 8% and 6%, for FRP modulus of elasticity and tensile strength and concrete compressive strength, respectively.

The results also show that ACI modified (Equation 4.13) results in a significantly lower uncertainty than the original expression proposed by ACI (Equation 4.10).

4.3 Safety factors calibration

Following the characterization of all random variables influencing the NSM FRP bond resistance, the partial safety factors were computed as described in Section 4.1.

Table 4.1 summarizes the results obtained after applying the partial safety factors method to each limit state function. In the following paragraphs some specific aspects of each limit state analysis are highlighted, while in Section 4.4 a critical analysis of the obtained results is presented.

Regarding the FRP rupture limit state, the expression to be used in design (R_d) is obtained from Equation 4.9 by replacing CFRP tensile strength by its characteristic value (f_{fk}) divided by the partial safety factor of CFRP tensile stress (γ_f). This characteristic value was obtained by computing the 5% quantile of Equation 4.7.

Regarding both ACI and modified ACI debonding limit states (which correspond to the same physical phenomenon), since only the average bond strength is not deterministic, in the sense that it is an assumed value, the reliability of the resistance function was applied to it.

Both concrete cohesive failure (C) and debonding (B) limit states of SA formulation depend on the concrete class. Hence, the results of these limit states were compiled in Table 4.2 per concrete class, considering all concrete classes available in the database used. Those concrete classes were estimated on the basis that the characteristic concrete strength could be obtained by subtracting 8 MPa to its mean value provided by the authors of the experimental studies for each specimen (CEN, 2004).

In both C and B limit states of SA formulation, the expression to be used in design is similar to their corresponding theoretical limit state functions. The only two differences are that concrete mean strength was replaced by its characteristic value (f_{ck}) divided by concrete's partial safety factor ($\gamma_c = 1.5$) (CEN, 2004) and that a new safety factor parameter was added in each expression. This parameter behaves as a global safety factor and was computed per concrete class. The obtained values were also presented in Table 4.2.

With the partial safety factors calibrated as described above, the expressions of ACI formulation presented in Section 2.4.1 should be replaced by Equations 4.14 and 4.15, in which $\gamma_f = 1.4$ and $\tau_d = 1.77$ MPa. Regarding the ACI modified formulation the only difference is that τ_d should be defined according to Equation 4.16.

$$L_d = \frac{A_f \frac{f_{fk}}{\gamma_f}}{p_f \tau_d} \tag{4.14}$$

Table 4.1: Results obtained in the partial safety factors method.

	Step in the partial safety factors method described in Section 4.1 [1]				
	(i)		**(iii)**	**(v)**	**(vi)**
Limit state	**Theoretical resistance function** (R_t)	**Random variables**	**Probabilistic resistance function distribution** (R)	**Design resistance function** (R_d)	**Safety factors**
F (ACI/SA)	Equation 4.9	f_{fu}	$\frac{R}{A_f} \sim N(2554.33; 298.18)^2$	$A_f \frac{f_{fk}}{\gamma_f}$	$\gamma_f = 1.4$
B (ACI)	Equation 4.10	-	$\frac{R}{6.9 L_b p_f} \sim LN(1.32; 0.70)^3$	$\tau_d L_b p_f$	$\tau_d = 1.77$
C (SA)	Equation 4.11	$E_f; f_c$	$\frac{R}{\sqrt{0.73 \varphi_{per}^{0.5} L_{per} A_f}} \sim^{2,4}$	$\eta_c \sqrt{0.73 \varphi_{per}^{0.5} (\frac{f_{ck}}{\gamma_c})^{0.67} L_{per} E_f A_f}$	[4]
B (SA)	Equation 4.12	f_c	$\frac{R}{\frac{2L_b}{\pi}(0.8+0.078\varphi_{per}) L_{per}} \sim^{2,4}$	$\eta_b \frac{2L_b}{\pi}(0.8 + 0.078\varphi_{per}) L_{per} (\frac{f_{ck}}{\gamma_c})^{0.6}$	[4]
B (ACI modified)	Equation 4.13	-	$\frac{R}{162(\frac{A_f}{p_f L_b})^{0.55} L_b p_f} \sim LN(0.97; 0.29)^3$	$\eta 162 \left(\frac{A_f}{p_f L_b}\right)^{0.55} L_b p_f$	$\eta = 0.38$

[1] step (ii) is depicted in Figure 4.2 while step (iv) was achieved by applying Equation 4.5 to each distribution of step (iii).
[2] joint probability obtained in 10^6 Monte Carlo simulations using the error δ and the existing random variables.
[3] equal to the error probability distribution (see Fig. 4.2) since that is the only random variable.
[4] see Table 4.2.

$$F_{fmax,d} = \begin{cases} A_f \frac{f_{fk}}{\gamma_f} \text{ if } L_b \geq L_d \\ A_f \frac{f_{fk}}{\gamma_f} \frac{L_b}{L_d} \text{ if } L_b < L_d \end{cases} \tag{4.15}$$

$$\tau_d = 61.6 \left(\frac{A_f}{p_f L_b} \right)^{0.55} \tag{4.16}$$

Similarly, SA formulation should be applied using Equations 4.17 to 4.19 to replace the corresponding ones in Section 2.4.2. In these equations $\gamma_f = 1.4$ and the parameters η_c and η_b should be taken from Table 4.2.

Table 4.2: Results obtained in the reliability analyses of SA limit states depending on the concrete class.

Concrete class	**C (SA)** $\frac{R}{\sqrt{0.73\varphi_{per}^{0.5} L_{per} A_f}} \sim$	η_c	**B (SA)** $\frac{R}{\frac{2L_b}{\pi}(0.8+0.078\varphi_{per})L_{per}} \sim$	η_b
C12/15	$LN(1088.39; 197.80)$	0.73	$LN(6.62; 4.06)$	0.29
C16/20	$LN(1156.37; 210.15)$	0.71	$LN(7.38; 4.54)$	0.27
C20/25	$LN(1217.96; 220.92)$	0.69	$LN(8.08; 4.96)$	0.26
C25/30	$LN(1287.07; 233.71)$	0.68	$LN(8.92; 5.48)$	0.25
C30/37	$LN(1348.87; 244.79)$	0.67	$LN(9.73; 5.98)$	0.25
C35/45	$LN(1406.82; 255.20)$	0.66	$LN(10.47; 6.44)$	0.24
C40/50	$LN(1458.9; 264.79)$	0.66	$LN(11.20; 6.89)$	0.24
C45/55	$LN(1507.47; 273.62)$	0.65	$LN(11.88; 7.29)$	0.24
C50/60	$LN(1553.57; 281.64)$	0.65	$LN(12.53; 7.71)$	0.23
C55/67	$LN(1597.68; 289.77)$	0.65	$LN(13.18; 8.12)$	0.23

$$\tau_d = \left(0.8 + 0.078\varphi_{per}\right) \left(\frac{f_{ck}}{\gamma_c} \right)^{0.6} \tag{4.17}$$

$$\delta_d = \left[0.73\varphi_{per}^{0.5} \left(\frac{f_{ck}}{\gamma_c} \right)^{0.67} \right] / \tau_d \tag{4.18}$$

$$F_{fmax,d} = \begin{cases} \eta_c \sqrt{\tau_d \delta_d L_{per} E_f A_f} \leq A_f \frac{f_{fk}}{\gamma_f} \text{ if } L_b \geq L_d \\ \eta_b \sqrt{\tau_d \delta_d L_{per} E_f A_f} \frac{L_b}{L_d} \leq A_f \frac{f_{fk}}{\gamma_f} \text{ if } L_b < L_d \end{cases} \tag{4.19}$$

4.4 Results analysis

The results obtained in the analysis presented in the previous sections are discussed in the following. The discussion begins by presenting, in Section 4.4.1, the performance of the guidelines' original formulations in terms of failure mode prediction. Then, the remaining sections detail the major aspects related with the reliability analysis.

4.4.1 Specimens separated by guidelines' failure mode detection

According to EC philosophy, a theoretical resistance function should be developed based on the physics of the phenomenon in analysis. This means that the developed theoretical resistance function should be capable of predicting the real failure mode, even if the predicted strength results inaccurate.

To verify that aspect, both ACI and SA formulations as defined in the corresponding guidelines (presented in Section 2.4) were applied to the database used. Figure 4.3 presents a comparison between the failure modes obtained in the experimental pullout tests (horizontal axis) and those predicted by ACI and SA guidelines (vertical axis). As can be seen, while in the experimental tests all the possible five failure modes occurred, in the guidelines' predictions only two failure modes were predicted (F or B in ACI and C or B in SA). Note that whilst this corresponds to all the failure modes that ACI considers, in the case of SA, the failure by FRP rupture was not predicted in any test.

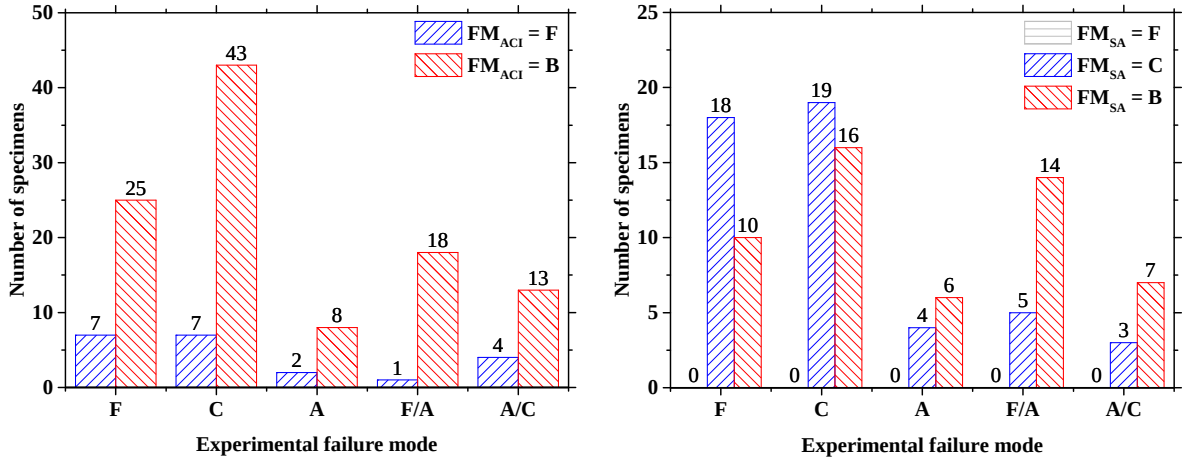

Figure 4.3: Failure modes (FM) obtained in the experimental tests *versus* its prediction using the theoretical resistance model defined in: (a) ACI guideline; (b) SA guideline.

Regarding ACI, it can be seen that its predictions fail more frequently when the failure occurs by FRP rupture than when it occurs by one of the other four failure modes (all grouped in the debonding failure mode of ACI). Taking into account that the failure by FRP rupture is expected to occur for the highest pullout force that a specimen can sustain (see Section 2.2), when ACI predicts debonding and the real failure mode was FRP rupture, the prediction can be considered safe. Contrarily, when ACI predicts FRP rupture and the real failure occurred by any debonding mechanism, the prediction is unsafe. Hence, even though ACI fails more frequently when the real failure mode is FRP failure, the major problem is related with those specimens in which ACI predicted

debonding failure and it actually occurred by FRP rupture.

Regarding SA, the first aspect to be mentioned is that, even though there are 32 specimens failing by FRP rupture in the database used, SA formulation did not predict any FRP rupture. Considering that the concrete failure is expected to occur for pullout forces larger than those occurring for any debonding failure (in SA this includes A, F/A and A/C) (see Section 2.2), the main problem regarding this formulation is also related with the prediction of debonding failure mode. In fact, there are several specimens for which the failure occurred by one of the three debonding mechanisms and SA predicted a failure within concrete.

4.4.2 Specimens separated by experimental failure mode

As already mentioned, a reliability analysis must be conducted taking into account the real failure mode occurred in each specimen. Hence, the specimens were separated by experimental failure mode regardless to the fact that, as referred in the previous section, the guidelines predict different failure modes in many cases.

Figure 4.4 presents the relationship between experimental pullout force and that foreseen by each guideline for each specimen. Note that the later was obtained by applying directly the limit state function corresponding to the experimental failure mode and not the formulation as described in each guideline.

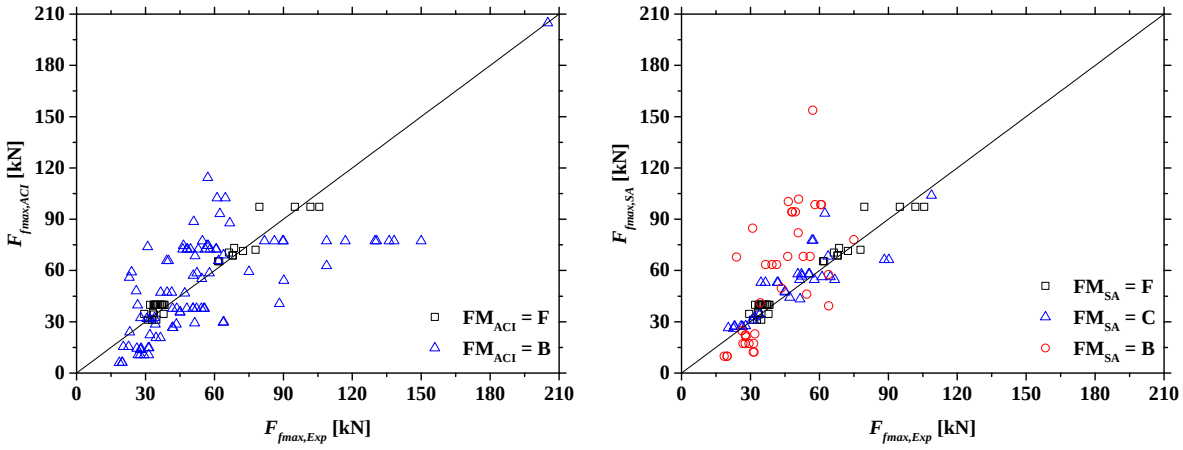

(a) (b)

Figure 4.4: Experimental *versus* predicted maximum pullout force considering the specimens separately by experimental failure mode (FM) and applying the corresponding limit state function using: (a) ACI guideline; (b) SA guideline.

For both guidelines it can be seen that the limit state function related with FRP rupture (F) is the one presenting the lowest dispersion in the predictions. In the case

of SA formulation, this dispersion was followed by the limit state functions for concrete cohesive failure (C) and, finally, debonding failure (B).

The limit state function associated with FRP rupture in NSM FRP systems coincides with the limit state function for the FRP rupture in tensile tests of FRP bars alone. The latter can be estimated using a classical and well established mechanical model (the product of the bar cross-section area by its normal strength). Hence, in this case, the dispersion of results should be mainly related with the different support conditions that exist in NSM FRP pullout tests when compared with those of a tension FRP bar test (together with the uncertainty in FRP mechanical properties).

The debonding limit state function addresses several failures using a single expression. Since the debonding mechanisms associated with each of these debonding failure modes are different, it is expectable that the same function predicts more accurately one of them and less accurately the reaming ones. This conclusion can be shown with the results in Figure 4.4b. Since SA has an individual limit state function for concrete failure, its dispersion is lower than that found for debonding failures. Moreover, since ACI debonding limit state function addresses four failure modes while in SA it addresses three, the dispersion of predictions is larger in the former (Figure 4.4a) than in the latter (Figure 4.4b). This, naturally, has implications on the partial safety factors that were determined.

4.4.3 Bond strength according to the theoretical resistance models

Again according to the principals defined in EC0 (CEN, 2002), a theoretical resistance function should be capable of predicting the phenomenon it is representing on average. This means that, the value of the theoretical resistance function error (δ), expressed as the ratio between experimental ($F_{fmax,Exp}$) and numerical ($F_{fmax,Num}$) pullout forces, should have an average equal to one, being its distribution approximately symmetric. Figure 4.5 presents the referred error obtained after applying both guideline's formulations to the database in analysis (red bars in each figure).

In both ACI (Figure 4.5a) and SA (Figure 4.5b) guidelines, about $\frac{1}{3}$ of predictions have a ratio inferior to one while the remaining $\frac{2}{3}$ stand above one. This means that both formulations are conservative, eventually already including some type of safety factors while those should be obtained *a posteriori*.

Contrarily, the ACI modified formulation (Figure 4.5c) presents 45% and 55% of the predictions equal or below and above the unit, respectively, resulting in a centred prediction.

4.4.4 Partial safety factor for CFRP (γ_f)

From the available data the 32 specimens that failed by FRP rupture were used in the calibration of γ_f. Since both ACI and SA formulations present the same function for this limit state, a single value of $\gamma_f = 1.4$ was obtained for both guidelines.

According to EC philosophy, each material should have a single partial safety factor to be used in all the situations where that material can be applied and regardless to the resistance model being used. The obtained γ_f matches that requirement.

The value of γ_f found herein corresponds to an upper bound of those suggested in the literature. According to the author's best knowledge, there are only two guidelines for the strengthening of concrete structures with FRP systems in which values of γ_f are explicitly provided.

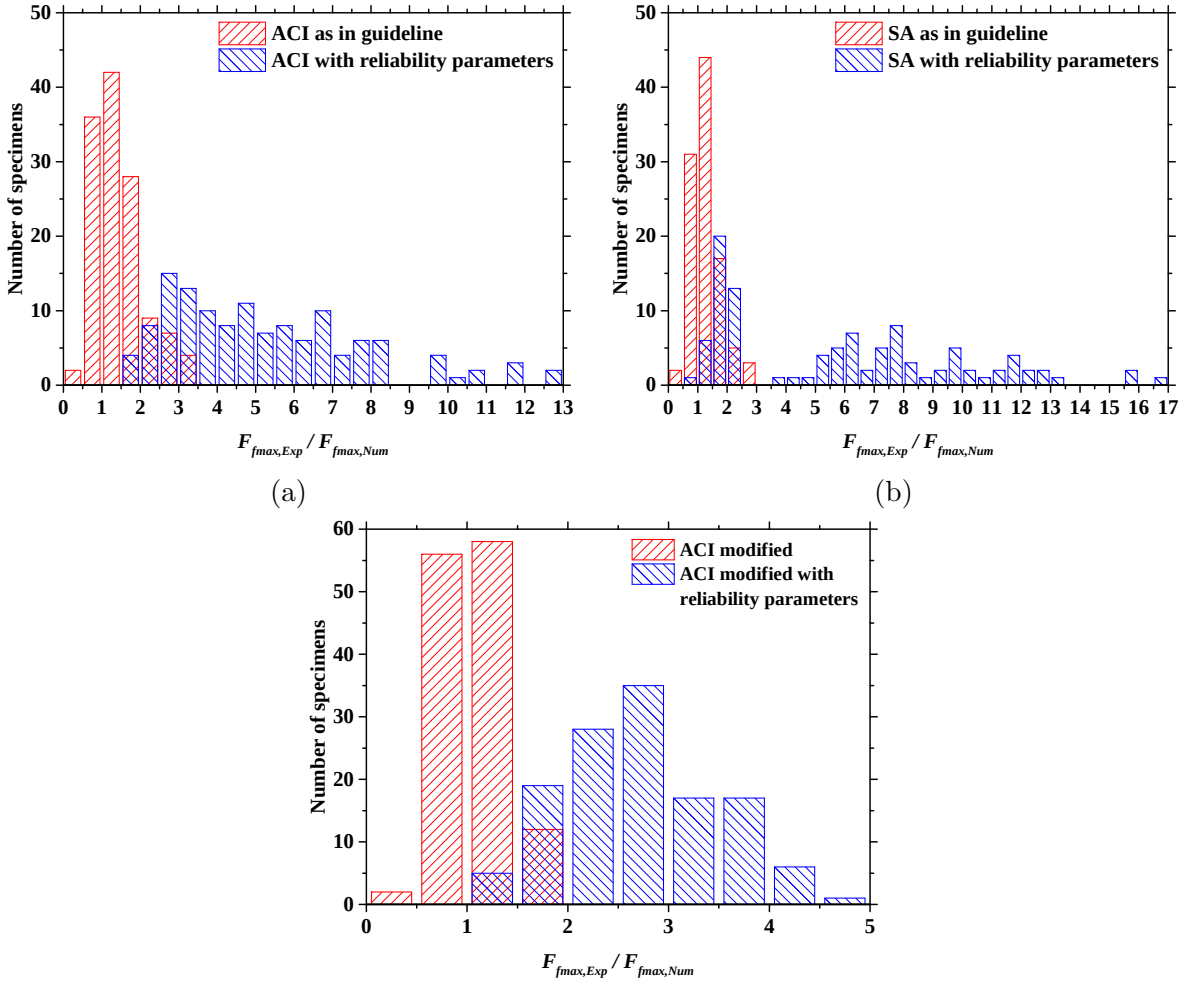

Figure 4.5: Histograms of the predictions errors for the resistance models of: (a) ACI guideline; (b) SA guideline; (c) ACI modified.

The first one, referred herein as Italian guideline (CNR, 2012), addresses the strengthening using the Externally Bonded Reinforcement (EBR) technique. It presents values of γ_f depending on the type of failure mode that can be influenced by the FRP properties. Hence, if the relevant failure mode is by FRP rupture (which is influenced by FRP properties) then its γ_f can be 1.1 or 1.25, depending on the type of certification of the strengthening system. If the critical failure mode is by debonding, γ_f can be 1.2 or 1.5, again depending on the certification type. Even though a single value should exist for γ_f, the authors of the Italian guideline decided for the use of different values for different limit states. Nevertheless, the important aspect is that the value suggested herein is in the range of those suggested by the Italian guideline thus harmonization of γ_f value could be easily achieved in the future.

The second guideline, is the Canadian Highway Bridge Design Code (CSA, 2006). This guideline presents the values for γ_f in the form of a global factor to be applied to FRP tensile strength. It suggests the use of 0.85 for Aramid and Carbon FRP and 0.75 for glass FRP, corresponding to γ_f of 1.18 and 1.33, respectively, which are also similar to the value of 1.4 suggested herein.

4.4.5 ACI debonding safety factor (τ_d)

Regarding the debonding limit state defined by ACI guideline it was decided to guarantee the required safety margin by reducing the bond strength. This resulted in replacing the value of the average bond strength proposed in ACI, $\tau_{avg} = 6.9$ MPa, by its design value $\tau_d = 1.77$ MPa, calibrated in Section 4.3. As referred before, this very large decrease (about 70%) in the bond strength results from the large uncertainty in the prediction models, a consequence of having a single expression addressing four different phenomena. Besides, as discussed in Section 3.1.1, the use of a single bond strength value, regardless of the FRP cross-section type, introduces a higher level of uncertainty than when the bond strength is estimated as a function of the FRP cross-section.

To verify that, the alternative designated ACI modified was also tested in Section 4.3. The design bond strength obtained with ACI modified was about 60% lower than the original value. This smaller reduction proves that, even if a single limit state function is used to address all four failure modes, a more accurate prediction model can result in a significant increase in design strength.

4.4.6 SA global safety factors (η_c and η_b)

Regarding SA limit states related with concrete and debonding failure modes, it was decided to guarantee adequate safety levels by applying global safety factors. The reason

for this decision is related with the type of variables included in their resistance functions. Besides geometric variables, which are treated as deterministic, both resistance functions contain two mechanical variables only. Namely, the compressive strength of concrete and the FRP modulus of elasticity (just in concrete limit state).

Regarding concrete compressive strength, it already has a well-established partial safety factor of 1.5 which, according to EC philosophy, should be maintained in all the applications of concrete material. Regarding the FRP modulus of elasticity, it is not usual to affect the elasticity modulus of a material with partial factors. Instead, the usual procedure consists on applying such factors to material's stresses and strains thus, by Hooke's law, the elasticity modulus remains unaffected by safety factors. In order to maintain this approach, thus addressing the compatibility between codes recommended by EC, it was also decided to do not apply partial safety factor to the FRP modulus of elasticity.

Hence, the solution adopted was the use of global safety factors as defined in Section 4.3 for concrete and debonding limit states. As expected, comparing the magnitude of values obtained, it can be seen that the safety factors are lower for debonding than for concrete limit state. This is mainly related with the former addressing several failure modes, as mentioned before.

For design purposes it would be better to have a single global safety factor for each limit state, regardless to the concrete class. In fact, EC also presents a single partial safety factor for concrete regardless to its class. On the other hand, the global safety factors obtained herein (see Table 4.2) are quite similar, thus the lowest value of each safety factor can be used for each limit state and for all concrete classes. The impact of this option would be a more conservative design for those specimens using concrete classes bellow C55/67, which is the class presenting the lowest global safety factors.

4.4.7 Bond strength in the theoretical resistance models with reliability parameters

Contrarily to what was referred before for the theoretical models, the models with reliability parameters are not expected to necessarily predict the real failure mode. In fact, these models will produce prediction values lower than the real ones, thus safer.

Figure 4.5 presents, as blue bars, the ratio between the experimental maximum pull-out force and that estimated using the proposed design formulations (including the corresponding safety factors). The obtained results show, as expected, that all these ratios are larger than one. The only exception occurs for SA guideline (see Figure 4.5b) where only one specimen attained a ratio of 0.94 mainly due to decimals rounding.

Comparing the magnitude of the ratios obtained, those are in agreement with the

reliability parameters estimated for each formulation. The higher the reductions applied to each limit state function, the larger the ratios are. It should be mentioned that, from a design viewpoint, larger ratios correspond to less economical designs, thus it would be better if the ratios were as small as possible, yet larger than one.

Concerning ACI formulation as defined in the guideline (Figure 4.5a) or its modified version (Figure 4.5c), it can be confirmed that the lower reduction on the design bond strength associated with the better accuracy of the latter, resulted in less conservative predictions. In other words, the blue bars in Figure 4.5a present a larger dispersion and are available in larger numbers in the right side of the figure than the ones shown in Figure 4.5c.

Regarding SA guideline (Figure 4.5b), the ratios are lower than 2.5 for about 40% of the specimens while for the remaining specimens the ratios increase up to 16.5. This should be related with the global reliability parameters applied for concrete and debonding failure limit states in SA formulation. In fact, the reductions applied to these limit states were as high as 35% and 77% of their theoretical prediction, respectively. This emphasizes the fact that safety factors should be applied to individual material properties, rather than to the entire resistance function.

4.4.8 Probability models adopted for CFRP parameters

Despite the considerable range of the two CFRP properties required by ACI and SA resistance models (E_f = [123-182] GPa, f_{fu} = [1850-3100] MPa), the same model was used for each parameter and for all specimens. Even though this could seem to be a limitation of the present study, the range of values referred above are within the range of values used in the development of the probabilistic models for CFRP properties used herein. Equations 4.6 and 4.7 were defined by using CFRP bars with E_f ranging between 118 to 218 GPa and f_{fu} ranging between 1780 to 3310 MPa (Gomes et al., 2013). Note that these CFRP bars correspond to a single brand from a single manufacturer. However, assuming that the production processes adopted by different manufacturers would be similar, the coefficients of variation regarding E_f and f_{fu} for other CFRP bars' brands, should be also similar, differing mainly in the average values.

It has been shown that CFRP tensile properties (E_f and f_{fu}) are well described by Weibull probability distributions (Atadero and Karbhari, 2005; Zureick et al., 2006; Gomes et al., 2013), which have a coefficient of variation, c_v, estimated according Equation 4.20, where Γ is the Gamma function and α is the Weibull distribution scale parameter. In the Weibull distributions presented in Equations 4.6 and 4.7 it can be seen that the parameter β (which does not appear in the expression of c_v) roughly coincides with the average value

of each property.

$$c_v = \frac{\sqrt{\Gamma\left(1+\frac{2}{\alpha}\right) - \Gamma^2\left(1+\frac{1}{\alpha}\right)}}{\Gamma\left(1+\frac{1}{\alpha}\right)} \tag{4.20}$$

Taking all of these into account, it can be assumed that since different CFRP brands would have different mechanical properties average values (related with the material composition) but similar coefficients of variation (related with the fabrication process), and that the average value has no influence on the coefficient of variation, the same model can be used for different CFRP brands, which validates the analyses presented in this work.

In any case, the results obtained in this work were found satisfactory. In the future, as new probabilistic models for these CFRP parameters become available, the analyses presented herein can be easily updated and these assumptions validated.

4.4.9 Influence of the mechanical model

As referred in Section 4.2, the improved versions of the guidelines formulations were also object of a reliability analysis using the methodology described in this chapter.

Regarding ACI, the recalibrated average bond strength value was equal to 9.25 MPa. As expected, it was found that the use of this value in the theoretical resistance function lead to the same value of $\tau_d = 1.77$ MPa in the design function. In fact, using 9.25, 6.9 or any other scalar as theoretical average bond strength, would lead to the same average bond strength design value. Using different scalars, one is just shifting the mean of the error being the coefficient of variation the same. Hence, unless the latter, which is the important statistical parameter in the reliability analyses, significantly changes, the design value would always be the same regardless to the theoretical value adopted.

An example of that change could be achieved by replacing the scalar average bond strength by an expression. That was already verified before when the ACI modified version was presented. In the end, the resistance design values obtained for ACI formulation with any scalar (6.9, 9.25, ... MPa) was always 0.26 while it increased to 0.39 for ACI modified version.

Regarding SA, the recalibrated expressions lead also to similar design values. In fact, the mechanical models were the same, but with lower average prediction errors. Hence, only the original version of this formulation was referred in the previous sections.

4.5 Reliability based design with soft computing models

For comparison purposes, the alternative models based on Data Mining (DM) algorithms (presented in Section 3.2) were also used in a reliability analysis similar to that presented in the previous sections for ACI and SA guidelines. The same group of specimens was used in the analysis with the data mining models.

Since only Direct Pullout Tests (DPT) specimens were considered in the reliability analysis, only the final four DM models developed for DPT (included in Table 3.6) were considered herein.

For all the four DM models, the reliability was introduced by means of a global safety factor. Since these models have no analytical expression this option was the most reasonable approach. The global safety factors obtained were 0.46, 0.50, 0.67 and 0.61 for the models using Artificial Neural Networks (ANN) and ACI inputs, Support Vector Machines (SVM) and ACI inputs, ANN and SA inputs and SVM and SA inputs, respectively. One of the conclusions of Section 3.1, was that the models using SA input parameters were more accurate than those using ACI inputs. Since the global safety factors for the two models using SA inputs are bigger, that conclusion is confirmed.

Comparing the global safety factors for each pair of models using the same inputs, SVM model is the best when ACI inputs are used, while ANN is the best when SA inputs are used. This again corroborates the conclusions included in Table 3.6.

To ease the comparison with the results presented in the previous section for ACI and SA guidelines, Figure 4.6 presents the histograms of the ratio between the experimental maximum pullout force and that estimated using both theoretical models predictions and those including reliability parameters predictions as red and blue bars, respectively, for all the four DM models.

Except for the model using ANN and ACI inputs, all the other three presented one specimen with a ratio lower than one. The values of the ratios for those specimens were 0.99, 0.98 and 0.87 for the models using SVM and ACI inputs, ANN and SA inputs and SVM and SA inputs, respectively. Hence, they were considered acceptable.

Regarding the histograms of the theoretical models the major conclusion is that they all present an amount of predictions lower and higher than one of about 50%, which, as already mentioned, is the expected behaviour of a theoretical model. The impact of that behaviour, associated with the great accuracy of all the four data mining models, is clearly seen in the histograms of the theoretical models with reliability parameters predictions. Those present a maximum ratio of 3.23 (for the model using ANN and ACI inputs), which

is lower than those obtained with any of the guidelines models (presented in Figure 4.5).

In addition, the dispersion seen in the blue bar histograms of Figure 4.6 is quite low, being its bars concentrated in a region between the ratios 1 and 3. This means that, designing with any of these four DM models would lead to more economical solutions, yet maintaining the same reliability index.

To complement this analysis, Table 4.3 present some metrics that were computed for the prediction errors of all the theoretical models (both guideline's and DM's models) with reliability parameters. This errors correspond to the same ratio used in the histograms shown in Figures 4.5 and 4.6.

Table 4.3: Metrics of all theoretical models with reliability parameters predictions errors.

Statistical metric	**Prediction model**						
	ACI guideline	**SA guideline**	**ACI modified**	**ANN with ACI inputs**	**SVM with ACI inputs**	**ANN with SA inputs**	**SVM with SA inputs**
Q_d	1.59	0.98	1.07	1.09	1.00	0.98	0.90
Mean	5.29	5.91	2.71	2.18	1.96	1.50	1.65
SD	2.56	3.98	0.77	0.38	0.32	0.16	0.21

Note: Q_d is the design percentile corresponding to the probability defined in Equation 4.5; SD is the standard deviation.

The first metric corresponds to the value of the design quantile of the error. This value was expected to be equal to one. However, since the errors are discrete values, this metric corresponds to the lowest value found. In any case, it is still possible to verify with this metric that, except for ACI guideline, all other models present a value close to the unit.

The remaining two metrics computed are the mean and standard deviation values of the predictions errors. The former allows to verify how conservative is in average each model while the later allows to check how stable the predictions of each model are. This again allow to see that ACI and SA formulations, as defined in their guidelines, lead to the less economic design values (higher mean). On the other hand, they are also the two models with higher differences between predictions (higher standard deviation), i.e. the difference between the best and worst predictions is higher for these models than for all the remaining others.

4.6 Conclusions

This chapter presented a reliability analysis over two of the most important guidelines for the design of concrete structures strengthened with NSM FRP systems. Namely, the

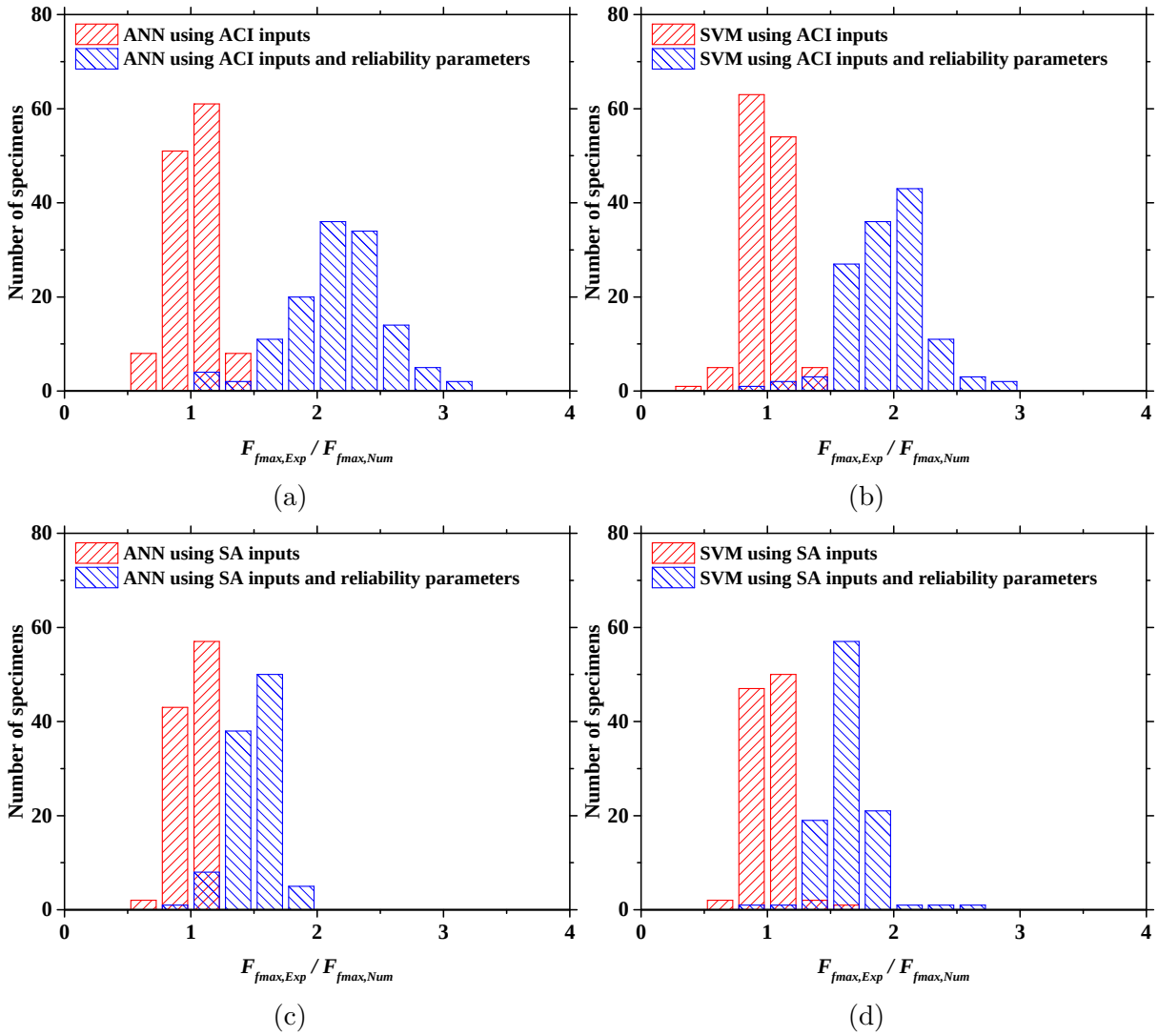

Figure 4.6: Histograms of the predictions errors for the resistance models using: (a) ANN algorithm and ACI input variables; (b) SVM algorithm and ACI input variables; (c) ANN algorithm and SA input variables; (d) SVM algorithm and SA input variables.

American Concrete Institute (ACI) and Standards Australia (SA) guidelines.

A formulation for calibrating the reliability parameters necessary to make the referred guidelines consistent with the partial safety factors philosophy was shown and the correspondent safety factors deduced. From the work presented herein, the following major conclusions can be drawn:

- the absence of probabilistic models for the different types of FRP limited this study to carbon FRP. A large scale analysis of the probabilistic models for FRP properties is paramount for defining reliable design codes;

- the amount of experimental data available is still very low. This has direct influence

in the definition of the errors associated with each limit state function. For this reason, in this work only direct pullout specimens with CFRP rectangular bars were considered. Hence, it is necessary to continue performing direct pullout tests, specially using combinations of parameters and materials that were not tested yet;

- due to the non-existence of a standard NSM FRP direct pullout test, part of the theoretical resistance models errors should be associated with the differences between tests conditions rather than with the models. In fact, aspects like specimen size, setup configuration or even support conditions could influence the experimental maximum pullout force value. That will naturally also influence the magnitude of the errors associated with the perdition models. Hence, the definition of a standard NSM FRP direct pullout test is urgent;

- while in the case of ACI formulation it was possible to define safety factors affecting directly specific properties (either FRP tensile strength or strengthening system bond strength), in the case of SA the reliability had to be included by means of global safety factors in order to maintain the partial safety factor of concrete in agreement with that already in the Eurocodes;

- it was confirmed that, mainly due to the difficulty of ACI and SA guidelines to predict separately all the five local failure modes existing in a NSM FRP system, more accurate resistance models should be developed for estimating the bond strength of NSM FRP systems in the future;

- regardless to the limitations of ACI and SA guidelines, the necessary safety factors were estimated and can be used in order to design NSM FRP systems according to Eurocodes philosophy, thus attaining a strengthening with the reliability index recommended by Eurocodes;

- finally, it was also proved that, prediction models based on data mining algorithms can also be used for design including the necessary reliability index.

CHAPTER 5

Experimental program of bond with NSM FRP systems in concrete

While there are two major types of bond tests to study the bond behaviour in Near-Surface Mounted (NSM) Fibre Reinforced Polymer (FRP) systems in concrete, the amount of Direct Pullout Tests (DPT) that have been conducted is bigger than that of Beam Pullout Tests (BPT). This is related with the advantages of the former as referred in Section 2.3.

On the other hand, neither DPT nor BPT are standardized. This aspect is more critical in the case of DPT, since the amount of test configurations used in the past is much higher than that verified in BPT. This absence of standardization was pointed out as a critical gap in Section 2.6. In fact, different combinations of concrete specimen shape (prismatic, c-shaped, h-shaped), loading conditions (single or double-shear) and concrete stress state (tension or compression) have been used by different researchers in the past. In Section 2.6 it was also mentioned that the standard DPT to be proposed would be either a tension or compression single-shear test.

Regarding the test control, the pullout tests have been performed by imposing a predefined rate of either force (force control) or displacement (displacement control). While for force control the load cell of the test machine is always used, for displacement control either the internal displacement of the test machine actuator or the displacement read by an external device (e.g. an LVDT, as in the present work) can be used. The later has the advantage of being possible applying it in order to control directly the FRP displacements at the loaded end section.

Using force control has the main disadvantage of only registering the test up to the

maximum pullout force. If the maximum pullout force is attained when the FRP fails in tension, the test ends. Otherwise, if any debonding mechanism occurs, there should be a post-peak response. Since the pullout force will diminish in post-peak, the machine load cell is unable of applying further load increments, thus the test will end. Contrarily, adopting displacement control has no such problem, thus the post-peak response can be obtained. However, using the internal displacement of the test machine actuator or an external LVDT placed at the loaded end has an important difference. In fact, even being in displacement control, it is almost impossible to obtain the post-peak response using the former.

For control purposes, a NSM FRP pullout test can be divided in two major stages. The first, corresponding to the initial elastic deformation of the FRP that goes from the loaded end section up to the machine grip. The second stage corresponds to the relative displacement between the FRP being pulled and the concrete block in which it is glued. In other words, the debonding process occurs only in the second stage.

The displacement magnitude of the first stage can be considerably bigger than that of the second one, thus, when the internal displacement of the test machine is being used, two scenarios can occur: (i) the test speed is slow enough to capture both stages of the test, thus it will take a lot of time; (ii) the test speed is increased so the first stage does not take too much time and the second stage can be lost. Normally, in the later scenario, the part of debonding process that occurs up to peak response is still captured, but the post-peak debonding process is lost. This is due to the recovering of FRP elastic deformation that takes place in post-peak.

When an LVDT placed at the loaded end is used instead, such problems do not exist, since it possible to fully obtain the second stage response in a reasonable amount of total time.

It was found in the literature that authors adopt either displacement or force control in their tests, both with a wide range of speed values. While it is believed that the former is best suited for NSM FRP DPT, due to the reasoning explaned above, an optimal value was not proposed yet.

Another aspect that was verified in the literature is that sometimes some authors, in an attempt to reduce concrete waste, reuse their concrete specimens in more than one side. However, according to the author's best knowledge, it was not yet verified whether or not such an option influences the obtained results or not.

In order to contribute for bridging these gaps, the DPT campaign presented in Table 5.1 was developed at the Structural Laboratory of the University of Minho Civil Engineering Department (LEST). Each series in this table was composed of three equal specimens.

Considering the review presented in Chapter 2, as well as the experience of the University of Minho Structural Composites research group, all tests were conducted using cubic blocks with 200 mm side. A concrete of strength class C25/30, according CEN (2004), was used. Each cube was tested in single-shear loading in three of the six sides available. In each side a groove with 5×15 mm^2 was cut and a carbon FRP (CFRP) bar with rectangular cross-section (designated laminate in what follows) was glued in it using an epoxy adhesive.

Also the bonded length was considered a fixed parameter, equal to 60 mm in all tests. In the scope of the research project in which this thesis was developed, several campaigns of pullout tests using the same NSM FRP system used herein were conducted. In one of those campaigns, the only parameter tested was the bonded length. From the results obtained in that campaign, it was found that the development length of this NSM FRP system would be about 80 mm (Fernandes, 2016). With a development length of 80 mm (or higher), the CFRP laminate attains its ultimate tensile strength. Considering that, since in the present campaign it was intended to obtain debonding failure mode, a bonded length of 60 mm was adopted.

While the parameters presented above (specimen and groove geometries, concrete strength class, bonded length, NSM FRP system) were kept equal in all tests, the following ones were evaluated:

- Test type: Single-shear compression *versus* tension tests, in order to assess the influence of the test configuration and concrete stress state;
- Test side of the concrete block in both compression and tension tests: lateral *versus* bottom side, in order to assess the influence of the concrete casting direction;
- Torque in compression tests: 30, 60 or 90 N×m, in order to assess the influence of the concrete initial stress state. Even though the great majority of DPT authors do not refer this value, it is believed that it can influence the obtained results;
- Test velocity in compression tests: 1, 2 or 5 $\mu m/s$, in order to assess the influence of the test speed.

The specimens are identified using the acronym A_B_C_D, where 'A' defines the type of test (C – compression; T – tension), 'B' stands for the testing side (BS – bottom side; LS – lateral side), 'C' defines the testing speed (V1, V2 and V5 – equal to 1 $\mu m/s$, 2 $\mu m/s$ and 5 $\mu m/s$, respectively) and 'D' stands for the torque applied to the steel rods (T0, T30, T60 and T90 – equal to 0 N×m, 30 N×m, 60 N×m and 90 N×m, respectively).

Table 5.1: Direct pullout test campaign (each series is composed of 3 specimens).

Series	Test type	Torque [$N \times m$]	Velocity [$\mu m/s$]	Test side
T_LS_V2_T0	Tension	-	2	Lateral
T_BS_V2_T0				Bottom
C_LS_V2_T60	Compression	60		Lateral
C_BS_V2_T60				Bottom
C_BS_V1_T60			1	Bottom
C_BS_V5_T60			5	Bottom
C_LS_V2_T30		30	2	Lateral
C_LS_V2_T90		90		Lateral

5.1 Tests configurations and specimen's preparation

Figure 5.1 shows the specimen's geometry and the corresponding test configuration. In the tension tests (Figures 5.1a and 5.1b), four M20 threaded steel rods were embedded in the concrete specimen and casted together with it. Those were then used to fix the specimen to a specific base used for tension tests.

In the compression tests (Figures 5.1c and 5.1d), a steel plate with 20 mm of thickness was applied on the top of the concrete specimen. This plate was then fixed to a base, different from that used in tension tests, by means of four M20 threaded steel rods.

Despite these slight differences in terms of specimen casting and test boundary conditions, everything else remained equal in the preparation of all tests.

As referred before, all specimens consisted of plain concrete cubes of 200 mm edge. They were casted using a specific mould, as shown in Figure 5.2a. This mould includes slots with threaded steel rods for tension tests' specimens and slots with plastic tubes which were used to pass the threaded steel rods that fix the compression test specimens.

All specimens were strengthened in three sides. Figure 5.3 depicts an example of a specimen and the corresponding casting mould slot to ease the identification of the strengthened sides. The two sides where either the plastic tubes or the steel rods passed, identified by the circles, were the top and bottom sides of the specimen while testing it, thus were not strengthened. Regarding the remaining four sides, only the top casting side was not strengthened. The main reason for this was that it is quite difficult to control the surface regularization during casting, thus the results obtained using the top side could be influenced by the different surfaces obtained in each cube.

In each strengthened side, a groove was made (see Figure 5.2b) 17 days after casting.

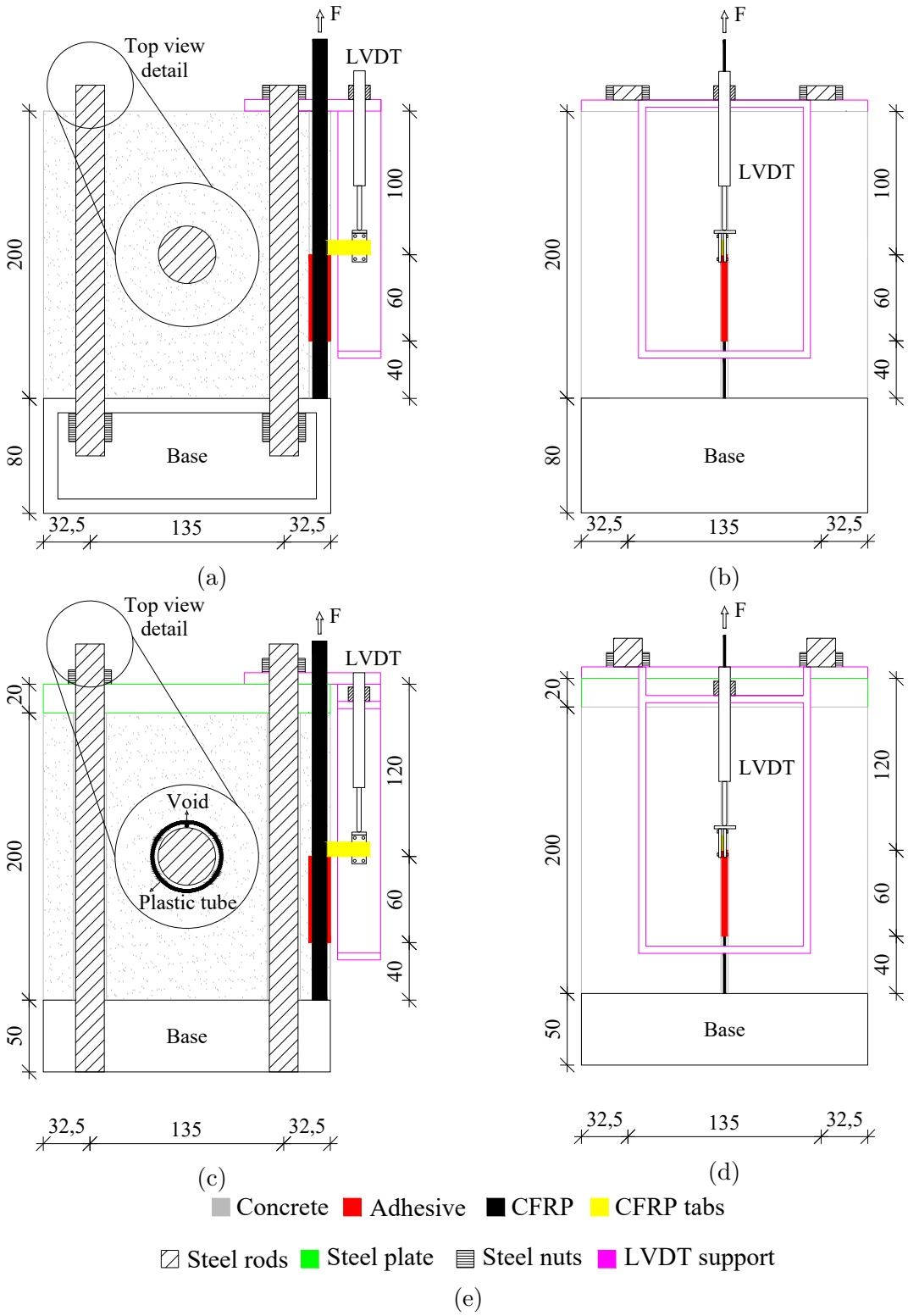

Figure 5.1: Geometry and test setup of direct pullout tests in: tension – middle section (a) and front view (b); compression – middle section (c) and front view (d). Note: the units are in millimetres.

While the groove was intended to have 5×15 mm^2, from discrete measurements made in several sections of the specimens, an average groove section of 5.20(±0.14) × 15.21(±0.29) mm^2 was obtained. A carbon FRP (CFRP) laminate (1.4×10 mm^2) was inserted and fixed using an epoxy adhesive.

To avoid premature failure of the specimens due to concrete cone formation near the top of the concrete block, the anchorage length was initiated at 100 mm from the top and extended 60 mm downwards.

The strengthening procedure, performed 44 days after casting, followed the steps detailed in Chapter 1. One specific detail adopted, but not explained in those steps, consisted on the application of paper tape prior to inserting the CFRP into the groove (see Figure 5.2c). This was made in order to avoid applying epoxy adhesive in the concrete surface since this could hide eventual cracks in the concrete during the tests.

All tests were performed 58 days after casting, thus 14 days after the strengthening. They were monitored with a displacement transducer (LVDT) and a load cell. The LVDT recorded the relative displacement between the CFRP and the concrete (slip) at the loaded end, s_l, while the applied force, F, was recorded through the load cell.

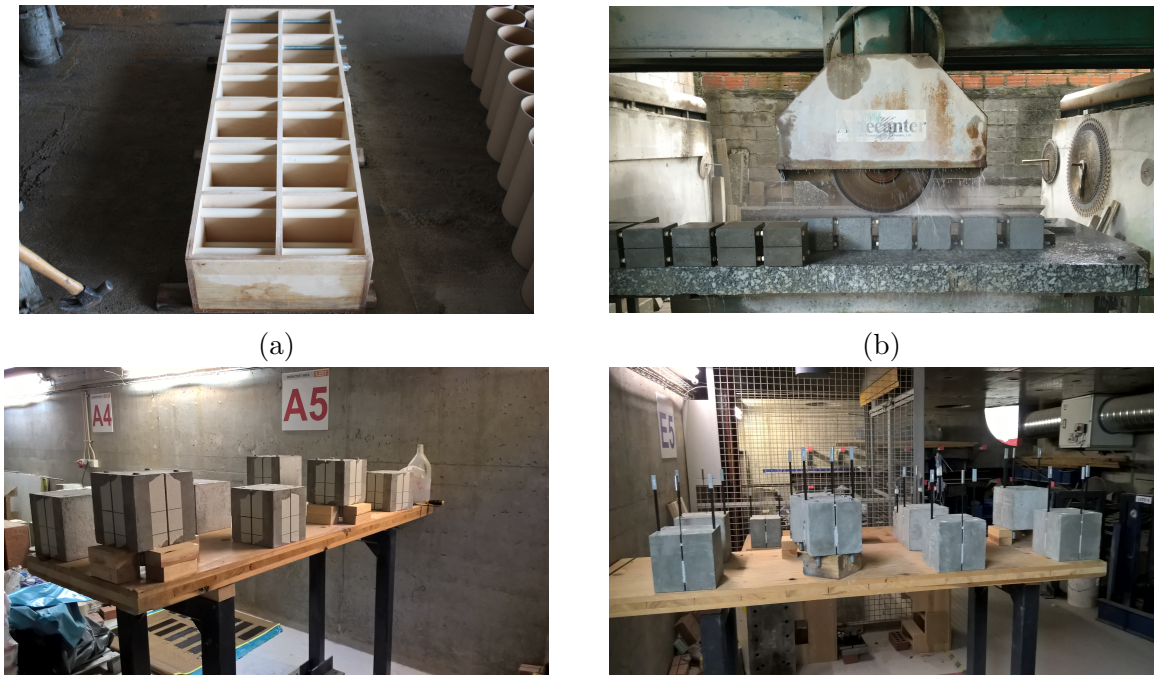

(a) (b)

(c) (d)

Figure 5.2: Preparation of the specimens: (a) mould for casting the specimens; (b) grooves opening; (c) paper mask application; (d) final appearance of the strengthened specimens.

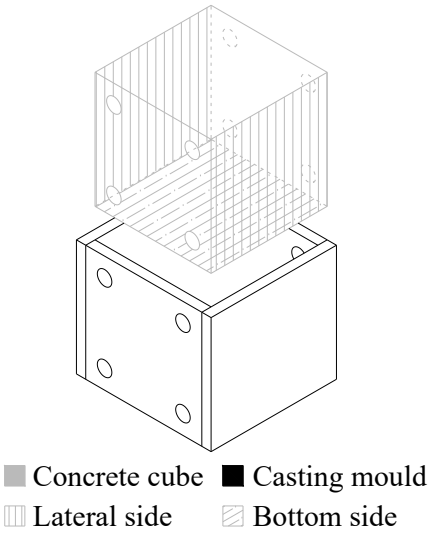

Figure 5.3: Identification of the strengthened sides in each cube.

5.2 Material characterization

Both CFRP laminate and epoxy adhesive were characterized in the scope of the research project in which this thesis was developed (CutInDur). The CFRP was characterized according to ISO (1997) and values of 169.5 GPa (coefficient of variation CoV = 2.5%), 2648.3 MPa (CoV = 1.8%) and 1.6% (CoV = 1.8%) were obtained for Young's modulus, tensile strength and strain at peak stress, respectively (Fernandes et al., 2015).

Regarding the epoxy adhesive, characterized according ISO (2012), values of 7.15 GPa (CoV = 3.71%), 22 MPa (CoV = 4.52%) and 0.36% (CoV = 15.22%) were obtained for Young's modulus, tensile strength and strain at peak stress, respectively (Fernandes et al., 2015).

The concrete, ordered to an external company, was required to be of strength class C25/30, exposure class XC2 and maximum aggregate size of 12.5 mm, according CEN (2004); slump class S4 and chlorides content class Cl0.4, according IPQ (2005).

Slump test was conducted, in the casting day, when the fresh concrete arrived. A value of 160 mm was obtained, which is whithin the range defined for slump class S4 ([160-210] mm), according IPQ (2005).

Twenty eight days after casting, the concrete was characterized by means of compression tests conducted to obtain the Young's modulus (LNEC, 1993) and compressive strength (IPQ, 2011). Values of 30.79 GPa (CoV = 2.84%) and 33.35 MPa (CoV = 4.33%) were obtained, respectively. Note that a concrete of strength class C25/30, according CEN (2004), should have mean values of 31 GPa and 33 MPa for Young's modulus and compressive strength, respectively.

5.3 Results obtained

Table 5.2 summarizes the results of the tests in terms of some important major outputs. The maximum pullout force (F_{fmax}) registered by the load cell and the corresponding loaded end slip (s_{lmax}) registered by the LVDT placed at that region. The maximum bond stress (τ_{max}), computed as the ratio between F_{fmax} and the contact area between CFRP and the epoxy adhesive. The ratio between the maximum normal stress installed in the CFRP f_{fmax} and its tensile strength f_{fu}. The fracture energy G_f, computed as the area under the pullout force *versus* loaded end slip curves. It should be stressed that G_f was only computed up to a loaded end slip of 2 mm. Finally, in the last column, the observed failure modes are reported, mainly failure at the interface between FRP and epoxy adhesive (F/A) or a combination of this (F/A) with concrete cohesive failure (C).

Table 5.2: Direct pullout tests main results (average for three specimens).

Series	F_{fmax} [kN]	s_{lmax} [mm]	τ_{max} [MPa][1]	$\frac{f_{fmax}}{f_{fu}}$ [%][1]	G_f [kN/mm]	Failure mode[2]
T_LS_V2_T0	24.19 (3.33)	0.35 (22.11)	17.69	65.2	29.66 (7.42)	F/A(3)
T_BS_V2_T0	25.55 (2.93)	0.47 (7.61)	18.68	68.9	33.92 (6.32)	F/A(3)
All T specimens	24.87 (4.16)	0.41 (20.70)	18.18	67.1	31.79 (9.56)	-
C_LS_V2_T60	23.41 (5.44)	0.53 (2.64)	17.11	63.1	29.56 (8.6)	F/A+C(2), F/A(1)
C_BS_V2_T60[3]	24.51 (0.80)	0.54 (3.60)	17.91	66.1	29.79 (4.61)	F/A+C(1), F/A(2)
C_BS_V1_T60	25.57 (0.86)	0.59 (11.56)	18.69	69.0	30.14 (3.22)	F/A(3)
C_BS_V5_T60	28.16 (2.22)	0.65 (8.22)	20.59	76.0	32.85 (11.7)	F/A+C(1), F/A(2)
C_LS_V2_T30	23.31 (3.88)	0.64 (1.17)	17.04	62.9	27.38 (7.09)	F/A(3)
C_LS_V2_T90	23.94 (0.85)	0.51 (4.88)	17.50	64.6	28.56 (4.24)	F/A+C(2), F/A(1)
All C specimens	24.83 (7.53)	0.58 (11.51)	18.15	67.0	29.71 (9.54)	-
All specimens	24.84 (6.81)	0.54 (19.17)	18.16	67.0	30.25 (10.02)	-

[1] coefficient of variation is the same obtained for F_{fmax}.
[2] values in parenthesis correspond to the amount of specimens with that failure mode.
[3] this series has only 2 specimens.

Figures 5.4 and 5.5 present, separated by series, the relationship between the pullout force and the loaded end slip ($F_f - s_l$) obtained in all the tests.

From these results, the following general conclusions can be drawn:

- in all tests the typical behaviour observed in NSM FRP systems in concrete was observed. Namely, the initial stage governed by the chemical bond between concrete, adhesive and CFRP, characterized by an almost linear behaviour. A second stage, corresponding to the progressive loss of chemical bond, which results in the degradation of the system's stiffness. Finally, a third stage governed by the friction that exists between the CFRP laminate and the surrounding adhesive;

- in all tests, the load level observed in the third stage (frictional phase) was almost

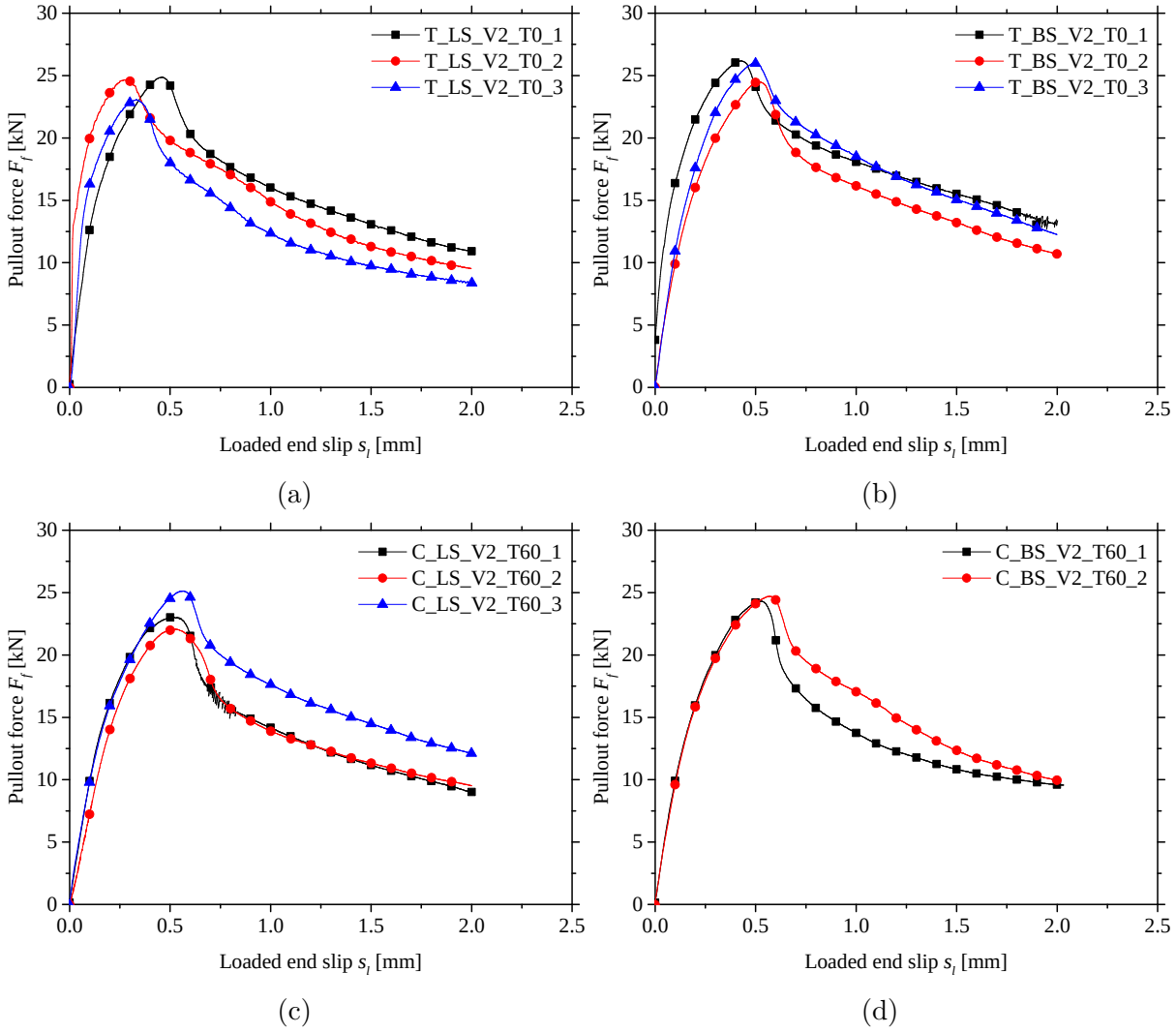

Figure 5.4: Pullout force *versus* loaded end slip obtained in series: (a) T_LS_V2_T0; (b) T_BS_V2_T0; (c) C_LS_V2_T60; (d) C_BS_V2_T60.

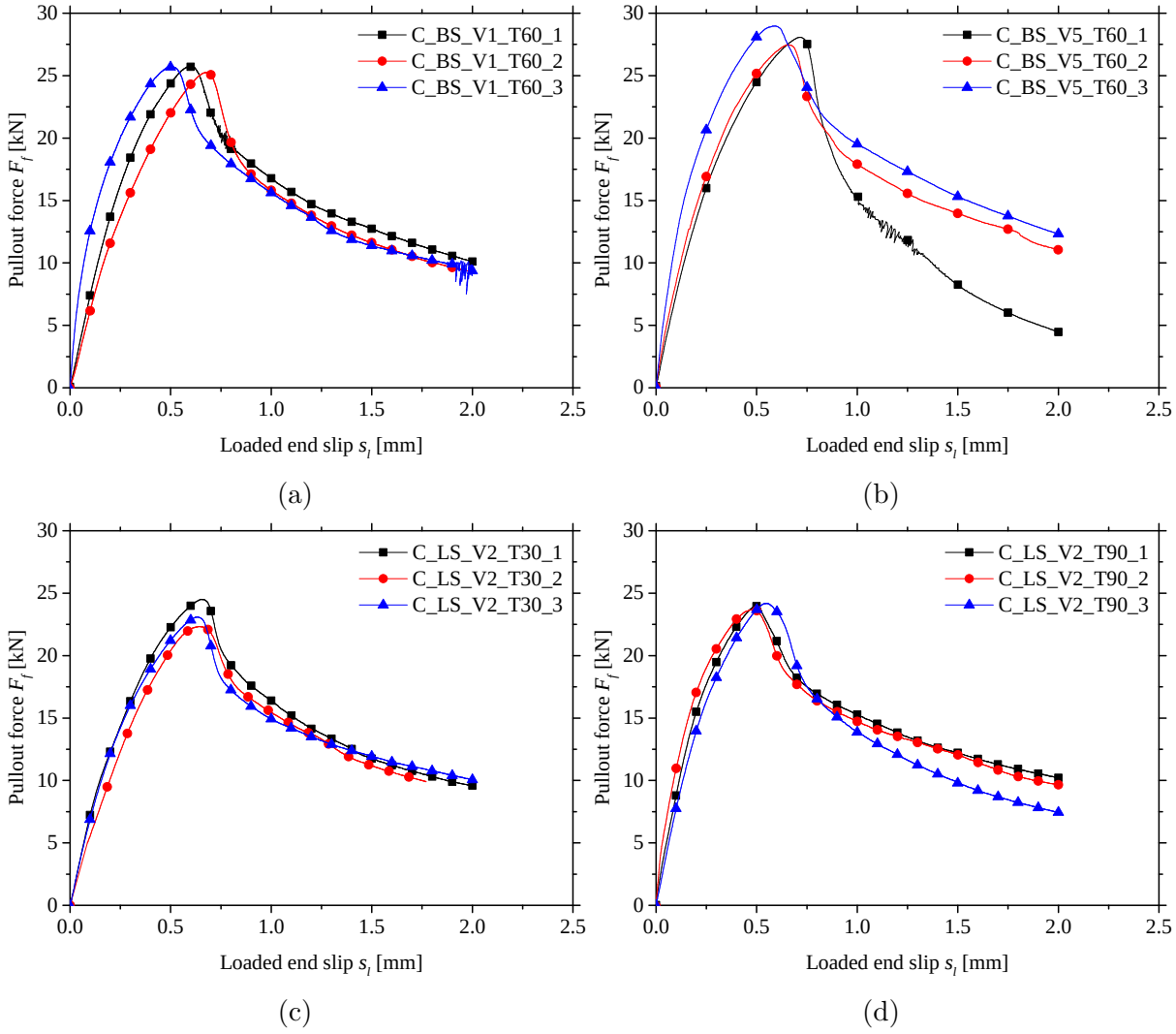

Figure 5.5: Pullout force *versus* loaded end slip obtained in series: (a) C_BS_V1_T60; (b) C_BS_V5_T60; (c) C_LS_V2_T30; (d) C_LS_V2_T90.

half of the maximum load obtained. This shows the important residual capacity that this NSM FRP system can sustain after debonding occur;

- the tests performed are quite similar in terms of F_{fmax} value. In fact, not only the CoV for each series is very low, but also the CoV obtained considering both tension tests series (All T specimens), all the six compression tests series (All C specimens) and all the tests (All specimens) together were found to be very low;

- the same similarity in the results was not observed in terms of s_{lmax}. The CoV of this parameter are in general bigger than those obtained for F_{fmax}. This suggests that, if one is only interested in obtaining F_{fmax}, any of the tests conducted could be selected to obtain it. Contrarily, if s_{lmax} is an important parameter to obtain, the test conditions adopted may be a concern. In the following paragraphs this issue is further discussed;

- another conclusion that can be extracted by comparing the obtained results with the existing literature, is the agreement between both:

  i. tension tests very similar to the reference series in tension (T_LS_V2_T0) presented herein were performed by Ceroni et al. (2012). The main differences between T_LS_V2_T0 series presented in Table 5.2 and those performed by Ceroni et al. (2012) are the bonded length (which was 300 mm in the later) and the concrete block dimensions (which were $160 \times 200 \times 400$ mm^3 in the later). Nevertheless, values of 0.3 mm and 23.3 kN were obtained for s_{lmax} and F_{fmax} by Ceroni et al. (2012), respectively, which compare very well with the ones obtained in series T_LS_V2_T0. Note that Ceroni et al. (2012) used strain gauges along the bonded length. The values referred before were computed when the local shear stress, evaluated by the strains recorded by the strain gauges closer to the loaded end, attained its maximum value;

  ii. on the other hand, compression tests almost equal to those presented in the reference compression series (C_LS_V2_T60) presented in Table 5.2 were conducted by (Fernandes, 2016). Those tests were also conducted by University of Minho researchers, using the same facilities and equipments used in the tests performed herein, thus no significant differences were expected. Nevertheless, the concrete used by (Fernandes, 2016) was different from that used herein and also the steel rods used to fix the concrete block were half the size of those used in this work (M10). Values of 0.55 mm and 24.25 kN were obtained for s_{lmax}

and F_{fmax}, respectively, which also compare with the ones obtained in series C_LS_V2_T60.

- the percentage of the ultimate strength of the FRP that was mobilized ranged between 60 and 75% of its ultimate strength, in all tests. This validates the choice for an L_b = 60 mm in order to safely study the bond behaviour and do not reach FRP rupture in any test.

Regarding the obtained failure modes, it should be firstly remembered that, as already mentioned in Section 2.5.2.11, there should be identified only one critical failure mode rather than presenting several failure modes based on the final appearance of the specimens. Hence, the interpretation of the failure modes should be conducted considering the whole picture together.

Nevertheless, in order to illustrate the failure mode interpretation procedure, Table 5.2 still reports the failure modes based on the specimens final appearance. In some specimens the failure consisted on a clean failure at FRP/adhesive interface (F/A) while in other it was a mix failure at FRP/adhesive interface and within concrete (F/A+C).

Failure mode F/A, exemplified in Figure 5.6a, was easy to identify since the specimens presented no other damage besides a small wedge of epoxy adhesive near the loaded end section (see Figure 5.6c), as a consequence of the debonding between FRP and epoxy adhesive.

(a) (b) (c)

Figure 5.6: Failure modes obtained in the direct pullout tests: (a) clean failure at FRP/adhesive interface (F/A); (b) mix failure at FRP/adhesive interface and within concrete (F/A+C); (c) loaded end section zoom.

Failure mode F/A+C, illustrated in Figure 5.6b, besides the phenomenon reported for F/A, presented also several cracks in the concrete. Those begun at the free end region

and developed towards the loaded end. This is the typical crack pattern commonly seen in NSM FRP systems in concrete (e.g., Sena-Cruz and Barros, 2004).

Considering the failure modes reported, it can be seen that the critical mode would be either failure at the interface FRP/adhesive (F/A) or concrete cohesive failure (C). To identify which of these was the critical one, the following reasoning was adopted.

Firstly, as previously mentioned, it was found that all tests achieved a similar pullout force, thus the stress level installed in the materials, which is directly related with the failure mode to obtain, was similar in all specimens. Secondly, it can be seen that series T_BS_V2_T0, C_BS_V1_T60 and C_BS_V5_T60 were the ones presenting higher pullout forces. Except for one specimen in series C_BS_V5_T60, all the other eight specimens in these three series showed only F/A. Hence, the critical failure mode should be F/A.

While this seems to be a valid interpretation of the critical failure mode, it is also important to understand why there are some specimens, even within the same test series, presenting the mix F/A+C failure mode. To clarify this, Figure 5.7 presents the location of series C_LS_V2_T60, C_BS_V2_T60 and C_LS_V2_T30 specimens in their corresponding concrete cubes. In this figure, the three lines represented consist on the contact surface between the concrete cube and the casting mould. The upper side is not represented since that was the side from which the concrete was introduced into the mould.

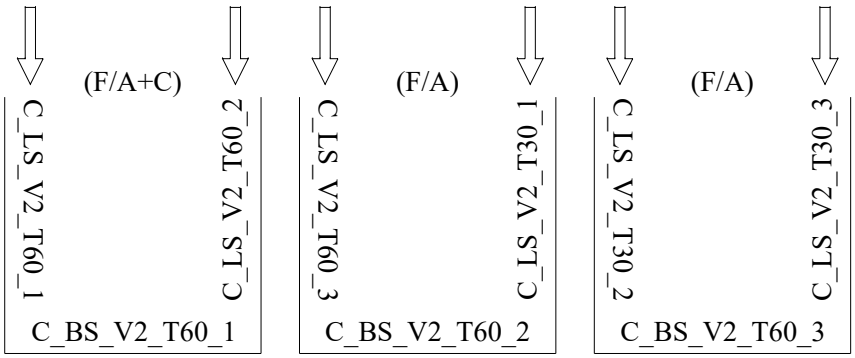

Figure 5.7: Location of series C_LS_V2_T60, C_BS_V2_T60 and C_LS_V2_T30 specimens in the concrete cubes. Note: the arrows illustrate casting direction.

For these three series, only three concrete cubes were necessary. The cube on the left contained specimens 1 and 2 of C_LS_V2_T60 series, the cube on the right contained specimens 2 and 3 of C_LS_V2_T30, the middle cube contained the remaining specimens of these two series, while in each cube the bottom side was used for C_BS_V2_T60 series.

As can be seen, even though the testing parameters where different in the three series, the failure mode obtained in all the tests using the same concrete cube (presented in

parenthesis on top of each cube) was the same. This suggests that the different failure modes should be related with the casting conditions of each concrete cube, rather than the testing parameters. This conclusion further emphasizes that the critical failure mode in all series was F/A.

Regarding the casting conditions referred before, it is not easy to come forward with an explanation since all specimens were casted simultaneously, using the same mould and the same concrete batch. The only two differences that could be pointed out are related with the application of dismantling fluid before casting and the vibration of the concrete cubes while casting. Even though these two aspect are user-dependent and very difficult to control, they were performed carefully in order to be as uniform as possible in all series.

5.4 Results analysis

In order to ease the interpretation of the obtained results, Figure 5.8 presents graphs with the average comparison between the relationship pullout force *versus* loaded end slip ($F_f - s_l$) of each series, properly arranged, in order to contain the parameters of interest for this study.

5.4.1 Influence of test type

Analysing Figure 5.8a it can be seen that the major difference between the average $F_f - s_l$ curve for series T_LS_V2_T0 and C_LS_V2_T60 is related with the stiffness of the pre-peak branch. This resulted in the same F_{fmax} but different s_{lmax} for each series.

After analysing the possible reasons for this behaviour, it was found that it should be related with the way the loaded end slip was being measured. In Figure 5.1 can be seen that, for both T_LS_V2_T0 and C_LS_V2_T60 tests, the LVDT registering s_l was supported in a steel device which was fixed at the top of concrete cube using the same steel threaded rods that fixed the concrete cube itself. Even though the slip is the relative displacement between the FRP and concrete, since the LVDT was in contact with concrete by means of the referred steel device, the slip measured was actually the relative displacement between the FRP and the steel threaded rods that hold the steel device in turn holding the LVDT.

While these steel rods were fixed to concrete in tension series (they were casted inside it), they were not in contact with concrete in compression series (they were placed inside the plastic tubes used). Hence, the concrete block could move horizontally in compression series, while it could marginally move in tension series. If the concrete block moves during the tests, the registered s_l values could be jeopardized. This becomes a bigger concern

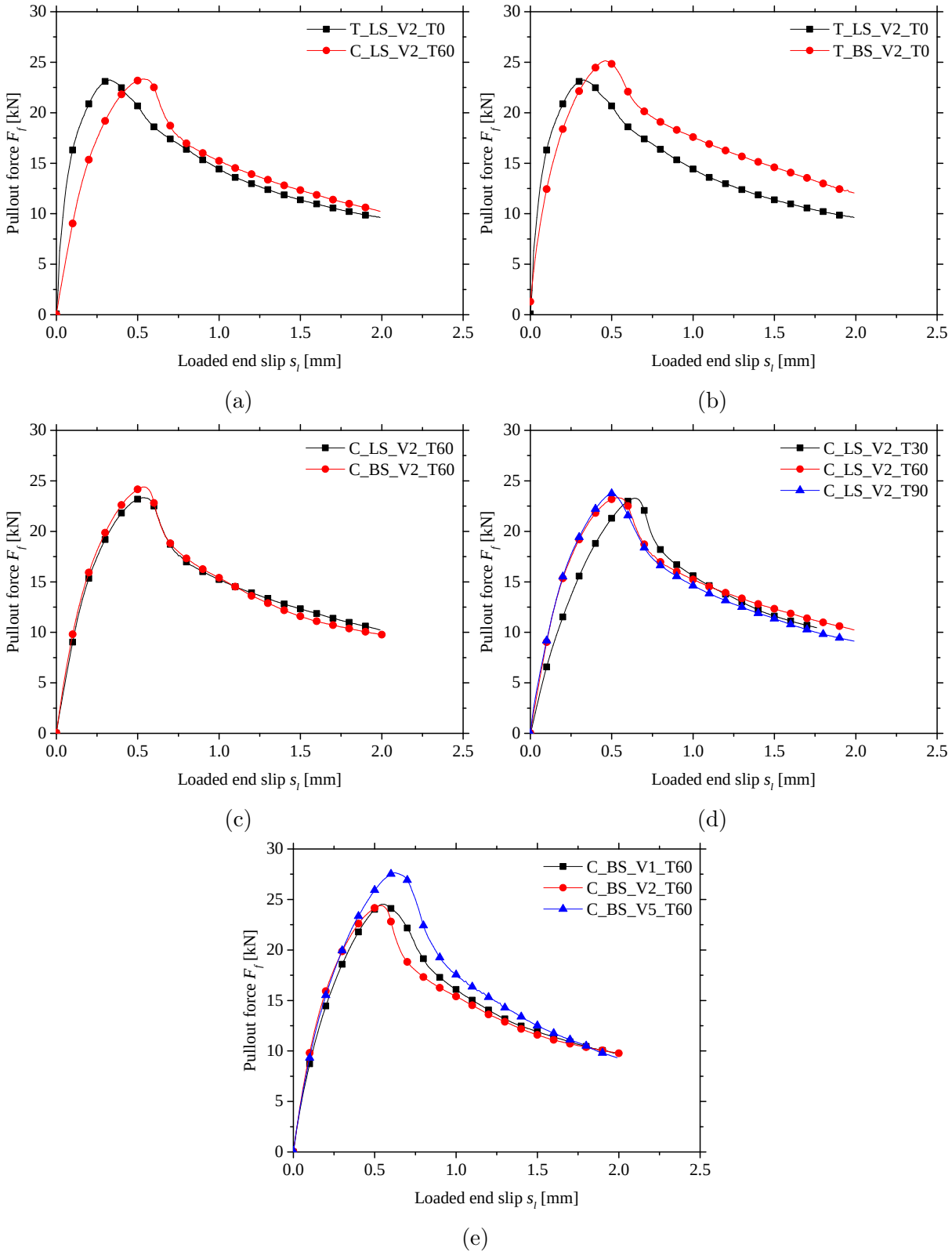

Figure 5.8: Pullout force *versus* loaded end slip obtained in series: (a) T_LS_V2_T0 and C_LS_V2_T60; (b) T_LS_V2_T0 and T_BS_V2_T0; (c) C_LS_V2_T60 and C_BS_V2_T60; (d) C_LS_V2_T30, C_LS_V2_T60 and C_LS_V2_T90; (e) C_BS_V1_T60, C_BS_V2_T60 and C_BS_V5_T60.

when considering the existing uplift of the concrete block during the tests. This uplift was similar in both T_LS_V2_T0 and C_LS_V2_T60 series and, considering the six specimens of these two series, attained a maximum value of 0.18 mm.

To verify this hypothesis, numerical simulations of series C_LS_V2_T60 were conducted. While the numerical simulation of this series is fully detailed in Section 6.2, in the analyses conducted herein, three different scenarios were considered:

1. in the first simulation (S1), fully detailed in Section 6.2, perfect bond between concrete cube and top steel plate (see interface A in Figure 5.9) was assumed, while the uplift of the cube at the test machine base was allowed;

2. the second simulation (S2), in which, besides restraining the slip between the top of the concrete cube and the steel plate, the contact surface between concrete cube and test machine base (see interface B in Figure 5.9) was also fully bonded, i.e. in this model the uplift of the cube was blocked;

3. the third simulation (S3), in which none of the contact surfaces referred in the previous models (S1 and S2) was restrained, i.e. there could occur relative displacements between the bottom surface of the concrete cube and steel base and between top steel plate and the top surface of the concrete cube.

Except for the different boundary conditions adopted in each of the three simulations conducted, everything else remained equal in all three. Namely, each one consisted of 2D FEM analysis, modelled as a plane stress problem using the generic mesh presented in Figure 5.9. The type of numerical elements used was: 4-node Serendipity plane stress elements with 2×2 Gauss-Legendre integration scheme for both concrete cube and steel plate; 2-node frame 2D elements for both FRP bars and steel rods; 4-node interface L2D elements with 2×1 Gauss-Lobatto integration scheme. The later were used to simulate not only the interface between CFRP and concrete, but also the interface between the top surface of the concrete cube and top steel plate in the simulations where the relative displacement at this region was allowed (S2 and S3). Regarding the interface between concrete cube and test machine base, unilateral contact supports were applied at the concrete block's base which allow for the cube uplift in the corresponding simulations (S1 and S3).

All materials were considered with linear elastic behaviour, using the properties defined in Section 5.2. The constitutive model adopted for all the interfaces was the one developed in the scope of the present thesis and fully described in Chapter 6. That chapter also presents the parameters used in the constitutive model describing the interface between

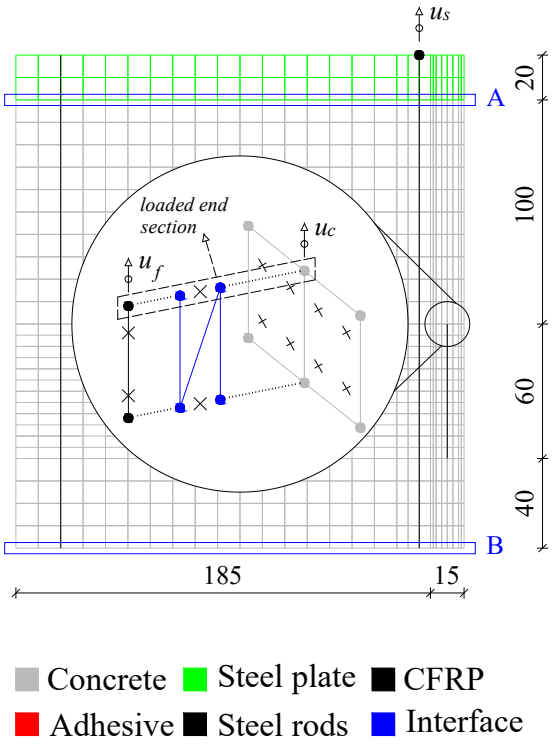

Figure 5.9: Mesh adopted in the FEM simulations conducted to validate the experimental results obtained in C_LS_V2_T60 series.

CFRP and concrete. The interface between concrete cube and top steel plate was provided with reasonable parameters in order to only allow the sliding between materials (i.e., the "opening" movement was restrained).

It should be clearly mentioned that these parameters are most likely wrong in terms of quantitative results. However, for the sake of the qualitative analyses intended in the present section, they were considered acceptable. In other words, while the results' trends presented in the following paragraphs are correct, the magnitude of the values obtained does not correspond to the experimental results.

Figure 5.10 presents a comparison between the results obtained in the three numerical simulations conducted. In Figure 5.10a the loaded end slip s_l was obtained as the difference between the FRP displacement (u_f in Figure 5.9) and the concrete displacement (u_c in Figure 5.9), both read at the loaded end section. Contrarily, in Figure 5.10b the loaded end slip was obtained as the the difference between the FRP displacement (u_f in Figure 5.9) and the displacement registered at the steel threaded rod top node (u_s in Figure 5.9) since, as previously mentioned, that was the point which fixed the steel device supporting the LVDT.

In both figures, the experimental average response obtained for series T_LS_V2_T0 and C_LS_V2_T60 was also included.

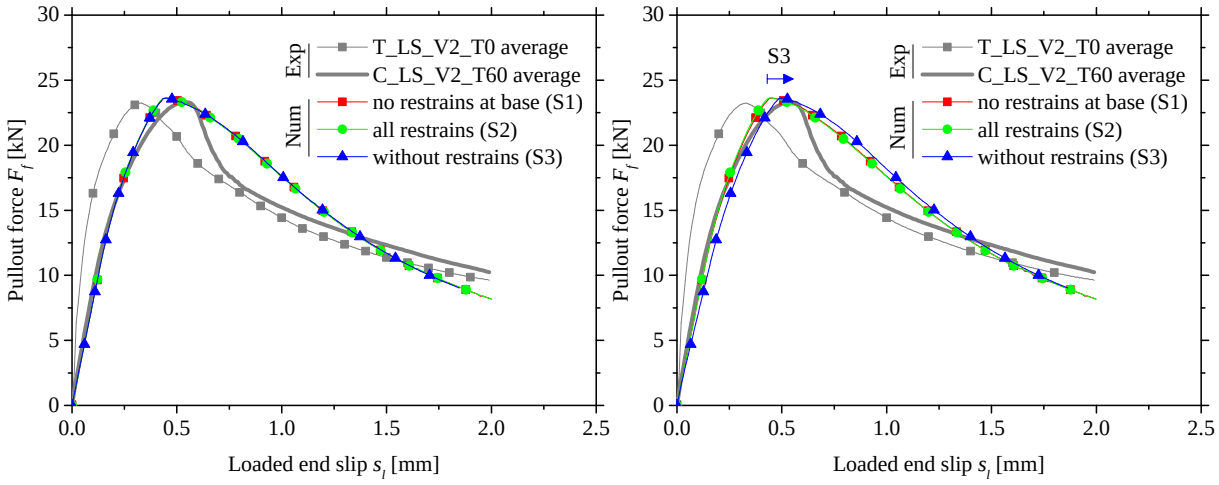

Figure 5.10: Pullout force *versus* loaded end slip obtained considering: (a) the slip as $(u_f - u_c)$; (b) the slip as $(u_f - u_s)$.

The results show that all the three numerical simulations (S1, S2 and S3) attain the same pullout force *versus* loaded end slip relationship, if the loaded end slip is obtained from $(u_f - u_c)$, as expected. However, when using $(u_f - u_s)$, the simulation S3 (without restrains at both top and bottom of concrete cube) achieved a result different from the other two simulations. Moreover, since in the other two simulations the results were the same, it is clear that the difference in the results is due to the relative movement between the concrete cube and the top steel plate, only allowed in simulation S3.

In Figure 5.10b the behaviour of the simulation S3, when compared with that of the other two simulations, has the same trend verified between series C_LS_V2_T60 and series T_LS_V2_T0 results. Namely, the maximum pullout force is the same but the corresponding slip is bigger, as highlighted by the blue arrow in Figure 5.10b.

While the previous paragraphs presented a reasonable explanation for the different loaded end slip registered in T_LS_V2_T0 and C_LS_V2_T60 tests, the magnitude of the difference observed numerically is very small when compared to the magnitude of the differences observed experimentally.

The reason for this difference could be related, as previously mentioned, with the parameters adopted for the constitutive model used to describe the interface between concrete cube and top steel plate.

Despite the differences between T_LS_V2_T0 and C_LS_V2_T60 series in terms of s_{lmax}, due to the reasons presented above, the results obtained in these two series still corroborate the literature in two ways. Firstly, as detailed in Section 5.3, because there are tests from other researchers in which similar results were obtained. But since in

this work the two test configurations were performed simultaneously, a second agreement can be found between this work's results and the literature. In fact, it was referred in Section 2.5.2.10 that the same values of F_{fmax} could be obtained using either tension or compression single-shear tests, as proved herein.

Whether this similarity is a consequence of the 100 mm unbonded length used in the tests (hypothesis suggested in Section 2.5.2.10) or a consequence of the failure mode not occurring within concrete (which would be the critical component when comparing the two types of tests), that is something that can only be answered in future experimental campaigns.

5.4.2 Influence of casting direction

Comparing Figures 5.8b and 5.8c it seems that only in tension tests there is an important influence of the test side. The peak point in the $F_f - s_l$ curve in tension tests seems to increase when the testing side is the bottom side when casting the specimens. Contrarily, in compression tests, such influence does not seem to be relevant.

It should be reminded that in series C_BS_V2_T60 only two valid tests are available, since there was a problem related with the LVDT readings in one of the three tests foreseen for this series. However, the pullout force was still properly registered and a value of 24.2 kN was obtained for F_{fmax}. This value is consistent with the other two of C_BS_V2_T60 series, thus it really seems that using specimen's lateral or bottom side has an incipient influence in the results of compression tests.

The best explanation that can be suggested for this behaviour should be, once again, related with either the application of dismantling fluid before casting or the vibration of the concrete cubes while casting. In fact, since the behaviour of both T_LS_V2_T0 and C_LS_V2_T60 series was the same (except from the s_l issue discussed before), the same similarity was expected to occur in T_BS_V2_T0 and C_BS_V2_T60 series.

On the other hand, the presence of steel rods in tension tests could have amplified the importance of the two explanations suggested. This would be even more important if the difference in the results was due to the vibration of concrete, which could be altered by the presence of steel rods.

Contrarily, the initial compressive state induced to concrete in compression tests could have reduced the influence of the casting direction in compression series.

Nevertheless, the results must be considered inconclusive and further experimental tests should be made towards solving this issue.

5.4.3 Influence of initial stress state level

The influence of the compression stress state level on the bond behaviour was assessed using three different prestress levels on the steel rods of compression tests. Specifically, torque values of 30, 60 and 90 N×m were adopted in series C_LS_V2_T30, C_LS_V2_T60 and C_LS_V2_T90, respectively.

From the average curves depicted in Figure 5.8d it can be seen that the behaviour was almost the same for torque values of 60 and 90 N×m. However, for a torque of 30 N×m, the value of loaded end slip s_l was larger than that obtained in the other two series.

This difference could be related with the lower confinement level provided by the lower torque value and, once again, it could also be related with the LVDT issue referred before. To clarify this, the numerical model referred in previous section in which the relative displacement between concrete cube and steel plate on its top was allowed, was again run using a torque of 30 N×m.

The obtained results showed that the global behaviour was exactly the same achieved when considering a torque of 60 N×m. However, in these two simulations the parameters used to describe the behaviour of the interface between concrete cube and the top steel plate were the same. But, since the torque of 30 N×m would result in a larger cube uplift, when compared to that obtained using a torque of 60 N×m, its interface behaviour should also be different. Namely, it should present a lower friction component (which is the only adhesion mechanism existing in this interface), thus the slip between concrete and steel plate would be bigger.

Since that slip (between concrete surface and the top steel plate) was not monitored during the tests, it is not possible to accurately simulate the different conditions at the interface between concrete and steel plate in the tests. Nevertheless, assuming that the reasoning explained above seems reasonable, that should be the explanation for the different behaviour.

Moreover, it can be guessed that the torque would have no influence in the results. In fact, the importance of the concrete strength increase, that was expected due to the increase of the confinement provided by the torque, would be easier to detect if the failure occurred within concrete. As it was found to be interfacial, it is not easy to verify the importance of this parameter.

Still, this should be verified with further experimental tests.

5.4.4 Influence of test velocity

Figure 5.8e presents a comparison between the $F_f - s_l$ curve for series C_BS_V1_T60, C_BS_V2_T60 and C_BS_V5_T60 using test speeds of 1, 2 and 5 $\mu m/s$, respectively.

As can be seen, while for test speeds of 1 and 2 $\mu m/s$ the results seem to be coincident, the same did not occurred for series C_BS_V5_T60. The later attained an higher peak response, thus both maximum pullout force and corresponding loaded end slip were bigger than those obtained for series with lower test speeds.

This behaviour was somehow expected since it is known for other materials properties, such as concrete compressive strength, that they increase with the rate of loading (e.g., Fu et al., 1991). Moreover, it was recently shown that similar behaviour is obtained when using the Externally Bonded Reinforcement (EBR) technique. Shen et al. (2015) performed double-shear tests at displacement rates of 0.07, 0.7, 7, and 70 mm/s on concrete specimens strengthened according to the EBR technique with basalt FRP sheets. They found that both the maximum pullout force and the corresponding displacement, thus the peak point, were successively increasing.

In pullout tests it is important to obtain, not only, the peak response (s_{lmax}, F_{fmax}) but also the post-peak behaviour. As can be seen in Figure 5.8, the pre-peak part is roughly 1/3 of the curves, while the remaining 2/3 of the curves present the post-peak behaviour up to a point where the post-peak trend was found to be perceived.

The corresponding average times (in minutes) for peak and final points of $F_f - s_l$ curves were 10/30, 5/15 and 2/6 for series C_BS_V1_T60, C_BS_V2_T60 and C_BS_V5_T60, respectively. Those show a perfectly linear relationship since the times for series C_BS_V2_T60 and C_BS_V5_T60 are 1/2 and 1/5 of those obtained in series C_BS_V1_T60.

There should be found a compromise between the test time and the impact on the results of increasing the test speed. Considering that in the tests conducted no intermediate test speeds are available, the value of 2 $\mu m/s$ can be suggested as optimal. Such test speed allows obtaining the full response in a reasonable time with no impact on the obtained results.

5.5 Conclusions

This chapter described the major details of an experimental campaign of Direct Pullout Tests (DPT). The main purpose of the tests conducted was to contribute for the development of a standard DPT. One of the major issues to be solved was the assessment of the differences between tension or compression DPT. In addition, three other parameters were analysed, since it is believed that those parameters should also be defined for the standard DPT. From the obtained results, the following conclusions can be drawn:

- the results obtained with both tension and compression tests were found to be similar

in terms of maximum pullout force. Regarding the corresponding loaded end slip, due to monitoring differences for getting such physical parameter fully justified, the results were not similar. However, it should be stressed that, comparing the results obtained with the existing literature, loaded end slip would be also similar if no problem occurred;

- since the results in terms of pullout force *versus* loaded end slip were very similar in both tension and compression DPT, the decision regarding which one should be the standard, will need to be made considering the importance of other parameters. For example, assuming that the standard DPT should also be used to study the bond durability, including corrosive environments, the existence of steel rods in the tension tests can be a drawback;

- the assessment of the impact of using three different sides in the same specimen was found to be inconclusive. Only in tension tests this seems to be a significant parameter, but more experimental tests (e.g., using bigger specimens in order to account for the real effect of casting) are necessary to clarify whether or not this is true and, if it is, why this is important;

- the torque applied to the steel rods in compression tests apparently has no influence on the bond behaviour. This should be related with the unbonded length that was left before the bonded zone;

- regarding the load speed used in the tests, it was verified that controlling the tests by imposing a speed rate of 2 $\mu m/s$ in the loaded end section, the full response can be obtained in a reasonable time and with no impact on the obtained results;

- as referred in the review presented in Chapter 2, the bond behaviour of NSM FRP systems in concrete is influenced by many parameters. Hence, the conclusions presented above are limited to the conditions in which the tests presented in this chapter were conducted and the parameters that were adopted. For example, if concrete strength, bonded length or FRP system, among others, were different, so the obtained failure mode would probably be thus the conclusions to be obtained could differ from those presented herein.

CHAPTER 6

Fracture-based interface model for NSM FRP systems in concrete

In the context of the present chapter, the bond behaviour of concrete elements strengthened with Fiber Reinforced Polymers (FRP) Near-Surface Mounted (NSM) systems is discussed from the standpoint of numerical simulation within the Finite Element Method (FEM). As referred in Section 2.3, the bond behaviour of such strengthening systems is normally studied by conducting bond tests. Hence, the focus of this chapter is more specifically devoted to the FEM simulation of FRP NSM bond tests.

In order to properly simulate this bond behaviour, three "continuum" materials and two "interfaces" need to be correctly simulated. These simulations include both physical representation and the material modelling of each one of them.

In terms of physical representation, line, surface or volume finite elements can be used to simulate all the three materials, depending on the type of FEM simulation to be performed.

Regarding the material modelling, there are already available in literature accurate non-linear constitutive models aimed at simulating the post-elastic and failure behaviour of concrete and adhesive, e.g. (Sena-Cruz et al., 2004; Ventura et al., 2008; Caggiano et al., 2011). The FRP can be simply assumed as linear elastic.

On the contrary, in the case of the interfaces, there is a lack of proper constitutive models. Hence the following paragraphs present a review of the strategies that have been adopted to simulate the existing interfaces, focusing on the main target of this chapter, i.e. the simulation of FRP NSM bond tests. Isoparametric zero-thickness interface elements

have been classically used for this purpose. Depending on the type of elements adopted to simulate FRP, adhesive and concrete, the interface finite elements can be lines or surfaces, in order to assure compatibility between finite elements.

From the literature review on experimental programs of pullout tests, described in Section 2.5, some included simulation of the interfaces' behaviour. Essentially two types of strategies to simulate the interfaces were found: (i) the first strategy consist on simulating the bond behaviour with a set of closed-form analytical expressions which were deduced from the physics of the observed phenomenon. Typically these mathematical expressions translate the different stages of stress transfer during a pullout test (Novidis et al., 2007; Mohamed Ali et al., 2008; Ceroni et al., 2012; Capozucca, 2013; Martinelli and Caggiano, 2014); (ii) the second strategy consists on the use of advanced numerical tools, namely, the Finite Element Method (FEM) for simulating the interfaces. This later one can in turn be divided into two.

The first group consists in using closed-form analytical expressions as constitutive models of interface elements. The use of such strategy as proved to be very effective in terms of capturing the global behaviour of the entire system. Even though it has been widely used in the past, since the scope of this chapter is limited to bond tests, only four examples were identified. Three of them use 2D FEM simulations of beam (Sena-Cruz et al., 2006) and direct (Ceroni et al., 2013; Sharaky et al., 2013) pullout tests. In all these three examples, only FRP and concrete were simulated with finite elements; the adhesive was simulated by the interface elements used in between FRP and concrete. Hence, the interface elements were used to simulate the joint behaviour of the adhesive and the two interfaces (FRP/adhesive and adhesive/concrete). Finally, the fourth example found consists on a 3D FEM simulation of beam pullout tests (Echeverria and Perera, 2013) in which the adhesive was simulated with volume finite elements.

The second group of works using FEM analyses, corresponds to approaches based on discontinuous constitutive models for zero-thickness interfaces, which represents the main subject of the present chapter. Since the bond behaviour in FRP NSM systems has an inherent three-dimensional nature, only four works using this approach in 3D FEM analyses were found in the literature. Three examples consist of direct pullout tests, two with round (De Lorenzis et al., 2004; Sasmal et al., 2013) and one with rectangular FRP bars (Teng et al., 2013). The fourth example consists of a beam pullout test with square FRP bars (Lundqvist et al., 2005).

In (De Lorenzis et al., 2004), the adhesive/concrete interface was modelled with a frictional model based on a Coulomb yield surface. The interface FRP/adhesive was modelled using an elasto-plastic interface constitutive model originally developed for internal steel

reinforcement. The yield surface of this model was defined by two functions. In tension, a Coulomb yield surface with zero cohesion and non-associated flow rule was adopted. In compression, another surface sets the limit in compression considering an associated flow rule.

In the second example of direct pullout tests with round FRP bars (Sasmal et al., 2013), the interface adhesive/concrete was not modelled, thus full bond was assumed between these two materials. The interface FRP/adhesive was modelled using a Mohr-Coulomb yield surface. This surface was limited by a normal stress equal to the tensile strength of the epoxy and by a limit value of tangential stress.

In the last example of direct pullout tests (Teng et al., 2013) the interfaces were not simulated since the experimental failure mode was not interfacial. Instead, a cohesive failure of the concrete surrounding the bonded length occurred. Once again, full bond between concrete and adhesive and adhesive and FRP bar was assumed.

Similarly, in the fourth example (Lundqvist et al., 2005) the authors also considered full bond in both interfaces since the failure in their tests was cohesive within adhesive and/or concrete. Hence, no interface constitutive model was used.

Comparing the two strategies using FEM analyses presented above, in practical terms, there is essentially one main difference between them. While the first (using an analytical expression as constitutive model) is generally based on assuming *a priori* an analytical expression for the interface bond-slip law, the second strategy is completely conceived within the general framework of constitutive theories (e.g. fracture mechanics, plasticity, damage, among others) where the interface bond-slip law is not known *a priori*.

It is worth mentioning that the first strategy, based on analytical expressions, normally needs a lower number of parameters to be adjusted (depending on the analytical expression adopted), which may explain the higher use of such strategy when compared with the second one.

In the following sections, the major details of the implementation of an interface constitutive model are summarized. Then, several numerical simulations are presented aiming at validating the implemented interface constitutive model.

6.1 Formulation of the interface constitutive model

Regarding the interface's constitutive model, it should have the ability of describing the two possible fracture modes in concrete elements strengthened with FRP NSM systems. Figure 6.1 presents an example of a FRP NSM direct pullout test where the FRP can be seen moving simultaneously in x_1^g and x_2^g directions. The sliding movement in x_1^g

direction is associated with fracture mode II while the opening movement in x_2^g direction is associated with mode I.

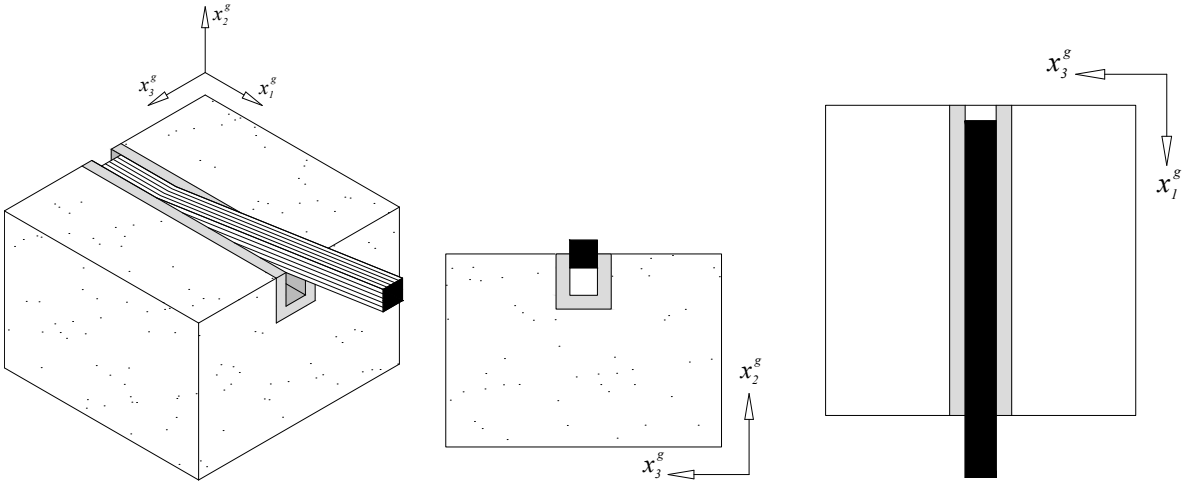

Figure 6.1: Fracture modes associated with concrete elements strengthened with NSM FRP systems: (a) 3D view; (b) opening (fracture mode I); (c) sliding (fracture mode II).

As previously referred, most formulations used in literature are based on adopting "a priori" analytical expressions for describing the interface bond-slip law. Furthermore, these formulations are generally based on assuming a fracture process in pure mode II thus neglecting the effect of the interface normal stresses and the occurrence of out-of-plane displacements.

The constitutive model implemented in this chapter was provided with separate modules which allow performing 2D and 3D analyses considering either only mode II or both modes I and II of fracture simultaneously. This represents one of the key contributions of this work.

All the work presented in this chapter was developed in the framework of FEMIX 4.0 (Sena-Cruz et al., 2007), which is a FEM code based on the displacements method. Figure 6.2 presents the numerical interface elements available in FEMIX on which the constitutive model was implemented. Particularly, it includes two line interface elements, with 4 and 6 nodes, which are schematically presented in Figures 6.2a and 6.2b, respectively. Even though each of those interfaces can be used in 2D and 3D simulations, in this chapter only 2D line interface elements are addressed.

FEMIX also includes two surface interface elements with 8 and 16 nodes (Figures 6.2c and 6.2d, respectively).

Table 6.1 presents the three modules of the implemented constitutive model:

- the first module is used for 2D and 3D FEM analyses where only fracture mode II

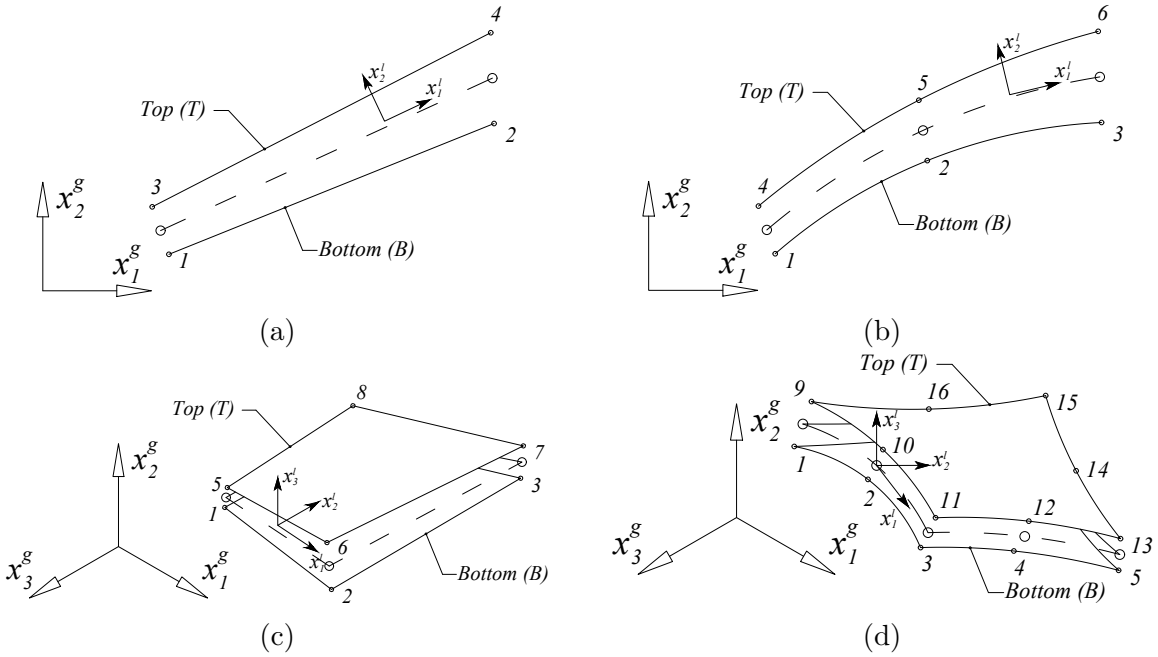

Figure 6.2: Interface elements available in FEMIX: (a) linear 4-node; (b) quadratic 6-node; (c) Lagrangian 8-node; (d) Serendipity 16-node.

is considered – developed by Caggiano and Martinelli (2013). Hence, the non-linear elasto-plastic behaviour is considered for local direction x_1^l, while the remaining directions behave elastically;

- a second module was developed for 2D FEM analysis where both fracture modes I and II are available – published in (Caggiano and Martinelli, 2012);

- the third module addresses 3D FEM simulations where all the local directions have an elasto-plastic coupled behaviour – proposed by Caballero et al. (2008).

The following paragraphs summarize the formulation of the three modules composing the implemented constitutive model. The most relevant expressions of all modules are presented together in Appendix B. Further detailed information regarding each module should be found in (Caggiano and Martinelli, 2013, 2012; Caballero et al., 2008).

The constitutive model presented is based on the classical Flow Theory of Plasticity. The basic assumption of this theory, in the context of small displacements, is the decomposition of the incremental joint relative displacement (designated as slip from this point onwards) vector, $\Delta\underline{s}$, in an elastic reversible part, $\Delta\underline{s}^e$, and a plastic irreversible one, $\Delta\underline{s}^p$. The later is defined according to a general flow rule which depends on the plastic multiplier $\Delta\lambda$ and the plastic flow direction $\underline{m}$. Hence, the relationship between slip and

Table 6.1: Details of the three modules composing the constitutive model implemented.

Constitutive model module	**Behaviour of each interface element**				
	Type	**Dimensions**	**Behaviour in each local direction**[1]		
			x_1^l	x_2^l	x_3^l
II	Line	2D	Elasto-plastic	Elastic	-
	Surface	3D		Elastic	
I/II_2D	Line	2D		Elasto-plastic	-
I/II_3D	Surface	3D		Elasto-plastic	

[1] see Figure 6.2 for more details.

stress in the constitutive model is obtained by the following expressions, where $\Delta\underline{\sigma}$ and $\underline{\underline{D}}$ are the incremental stress vector and the constitutive matrix, respectively.

$$\Delta\underline{s} = \Delta\underline{s}^e + \Delta\underline{s}^p \tag{6.1}$$

$$\Delta\underline{\sigma}^e = \underline{\underline{D}}^e \Delta\underline{s}^e = \underline{\underline{D}}^e(\Delta\underline{s} - \Delta\underline{s}^p) \tag{6.2}$$

$$\Delta\underline{s}^p = \Delta\lambda\underline{m} \tag{6.3}$$

Assuming that in a generic stress state $n-1$, previously converged, the slips and stresses vectors and the hardening parameters are known, all these parameters need to be updated when a new increment of the slip vector is added (step n). This update is performed by using the backward Euller method (Carol et al., 1997) presented in the local return-mapping algorithm flowchart of Figure 6.3. Block (2) of this flowchart corresponds to the beginning of the new step where the stress vector is updated by adding the new increment of slip vector. Then, if the new stress state lies inside the yield surface (i.e. the third residue $f_{3,n}^q$ is negative – see block (4) in Figure 6.3), the actual stress state is in the elastic phase, otherwise it has a plastic component that must be accounted for. This is made using an iterative Newton-Raphson method which requires the estimation of the Jacobian matrix, $\underline{\underline{J}}$, in order to estimate the variations δ of stress and state variables (i.e. hardening parameter κ and plastic multiplier $\Delta\lambda$) in the new iteration. The Jacobian matrix (Equation 6.4) is obtained by deriving the three functions used to estimate the residues necessary to check the stress state (see block (3) in Figure 6.3), as shown in Equation 6.4. This algorithm is then repeated until convergence is reached, i.e. until all three residues are lower than a predefined tolerance (see block (5) in Figure 6.3).

$$\underline{\underline{J}} = \begin{bmatrix} \frac{\partial f_1}{\partial \underline{\sigma}} & \frac{\partial f_1}{\partial \kappa} & \frac{\partial f_1}{\partial \Delta\lambda} \\ \frac{\partial f_2}{\partial \underline{\sigma}} & \frac{\partial f_2}{\partial \kappa} & \frac{\partial f_2}{\partial \Delta\lambda} \\ \frac{\partial f_3}{\partial \underline{\sigma}} & \frac{\partial f_3}{\partial \kappa} & \frac{\partial f_3}{\partial \Delta\lambda} \end{bmatrix} = \begin{bmatrix} \left[\underline{\underline{D}}^e\right]^{-1} + \Delta\lambda \frac{\partial \underline{m}}{\partial \underline{\sigma}} & \Delta\lambda \frac{\partial \underline{m}}{\partial \kappa} & \underline{m} \\ -\frac{\partial \Delta\kappa}{\partial \underline{\sigma}} & 1 - \frac{\partial \Delta\kappa}{\partial \kappa} & -\frac{\partial \Delta\kappa}{\partial \Delta\lambda} \\ \underline{n} & \frac{\partial f}{\partial \kappa} & 0 \end{bmatrix} \tag{6.4}$$

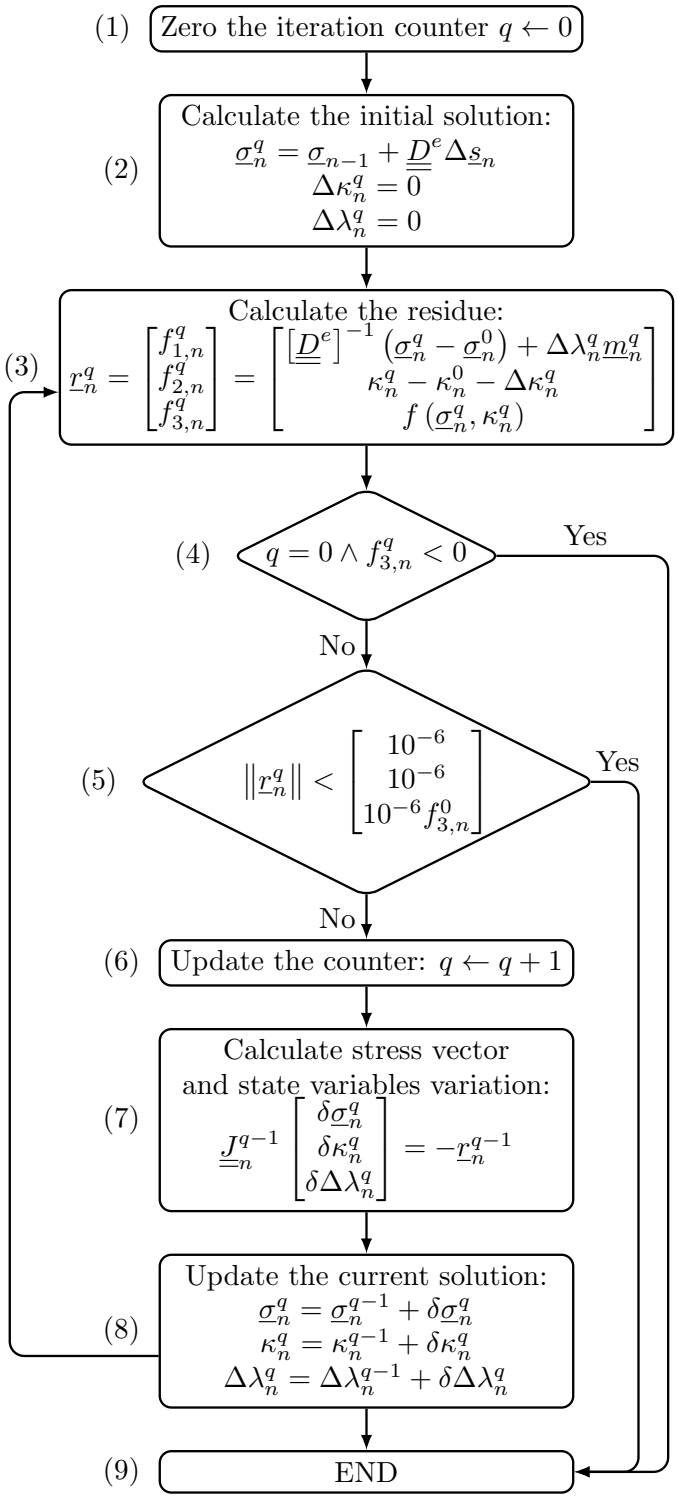

Figure 6.3: Local return-mapping algorithm.

If the constitutive relation presented in Equation 6.2 is true for elastic increments, it ceases to be when entering into the elasto-plastic regime. Hence, the elastic constitutive matrix shall be replaced by an elasto-plastic one. In this case, the expression of this new matrix can be deduced by imposing the consistency conditions and the Kuhn-Tucker condition presented in Equation 6.5 (Carol et al., 1997). Taking into account that the constitutive model was formulated under the work-hardening hypotheses, this condition can be rearranged to obtain the plastic multiplier (Equation 6.6), where the parameter H is defined according to Equation 6.7. Replacing the plastic multiplier in the constitutive relation of the interface model, the elasto-plastic constitutive matrix can be obtained (Equation 6.8). Hence the new relation between slip and stress vectors is finally defined according Equation 6.9.

$$\Delta\lambda \geq 0,\ f(\underline{\sigma},\kappa) \leq 0,\ \Delta\lambda f(\underline{\sigma},\kappa) = 0,\ \Delta f(\underline{\sigma},\kappa) = 0 \tag{6.5}$$

$$\Delta\lambda = \frac{\underline{n}^T \underline{\underline{D}}^e \Delta\underline{s}}{H + \underline{n}^T \underline{\underline{D}}^e \underline{m}} \tag{6.6}$$

$$H = -\frac{\partial f(\underline{\sigma},\kappa)}{\partial\lambda} \tag{6.7}$$

$$\underline{\underline{D}}^{ep} = \underline{\underline{D}}^e \left(1 - \frac{\underline{n}^T \underline{\underline{D}}^e \underline{m}}{H + \underline{n}^T \underline{\underline{D}}^e \underline{m}}\right) \tag{6.8}$$

$$\Delta\underline{\sigma} = \underline{\underline{D}}\Delta\underline{s} \Rightarrow \underline{\underline{D}} = \begin{cases} \underline{\underline{D}}^e & \text{if loading/unloading/reloading (elastic phase)} \\ \underline{\underline{D}}^{ep} & \text{if loading (elasto-plastic phase)} \end{cases} \tag{6.9}$$

Appendix B includes all the expressions used in the formulation of the constitutive models. This includes yield function f, hardening variables $\underline{\Phi}$, yield surface gradient $\underline{n}$, plastic potential g, plastic potential variables $\underline{\Psi}$, plastic flow direction $\underline{m}$ and hardening law $\Delta\kappa$. In the following paragraphs few important comments are presented regarding those parameters.

In all the three Constitutive Model (CM) the hardening parameter is the plastic work, since, as referred before, work hardening was admitted in all formulations. However, the way the hardening parameter affects the yield surface is different in each CM since it depends on different variables. Hence, in CM II there is only a single hardening variable which is the shear strength, c, while in the other two CM (I/II_2D and I/II_3D), three variables exist: tensile (χ) and shear (c) strengths and the friction angle ($\tan\phi$).

The plastic potential surface of CM II and I/II_2D is not explicitly defined. However, since the formulation only requires the direction of the plastic flow, that is provided instead. The major difference between these two CM is that in CM II the plastic flow is

associated while in CM I/II_2D a non-associated flow rule is admitted. Additionally, in CM I/II_2D an additional parameter exists which is the dilation stress, σ_{dil}. This stress corresponds to the normal stress at which the dilatancy vanishes when compression and shear stresses occur at the same time.

The plastic potential of CM I/II_3D is described through a hyperbola identical to the yield surface but with different shear strength and friction angle (tensile strength is the same). This means that, in this model, plastic potential shear strength and friction angle need to be provided.

In terms of hardening law, it should be highlighted that, in CM I/II_2D and CM I/II_3D, due to the different interaction that occurs between tangential and normal stresses, different expressions are used for the scenarios of tension and compression.

In all three CM, the evolution of the yield surface depends on the evolution of the hardening parameters, which depend on the evolution of the plastic work, W. The variation of the plastic work is considered by means of a dimensionless parameter (Equation 6.10), which translates the amount of fracture energy, G_f, spent in a certain plastic work. Since CM I/II_2D and CM I/II_3D account for two fracture modes, there will be two dimensionless parameters in those CM, one for fracture mode I and other for fracture mode II.

Each dimensionless parameter is then input of a scaling function (Equation 6.11) in addition to a shape parameter (α) which can be different for each hardening variable. Equations 6.12 to 6.16 present the variation of each hardening variable where the indexes 0 and r, refer to the initial and residual value of the corresponding variable, respectively.

$$\xi_i = \begin{cases} \frac{1}{2} - \frac{1}{2}\cos\left(\frac{\pi W}{G_f^i}\right) & \text{if } 0 \leq W \leq G_f^i \\ 1 \text{ if } W > G_f^i \end{cases}, i = \{I, II\} \tag{6.10}$$

$$S\left(\xi_i, \alpha_j\right) = \frac{e^{-\alpha_j \xi_i}}{1 + \left(e^{-\alpha_j} - 1\right)\xi_i}, i = \{I, II\}, j = \{\chi, c, \tan\phi\} \tag{6.11}$$

$$c = c_0 \left[1 - S\left(\xi_{II}, \alpha_c\right)\right] \tag{6.12}$$

$$\chi = \chi_0 \left[1 - S\left(\xi_I, \alpha_\chi\right)\right] \tag{6.13}$$

$$\tan\phi = \tan\phi_0 - \left[\tan\phi_0 - \tan\phi_r\right] S\left(\xi_{II}, \alpha_{\tan\phi}\right) \tag{6.14}$$

$$c_g = c_{g,0}\left[1 - S\left(\xi_{II}, \alpha_{c_g}\right)\right] \tag{6.15}$$

$$\tan\phi_g = \tan\phi_{g,0}\left[1 - S\left(\xi_{II}, \alpha_{\tan\phi_g}\right)\right] \tag{6.16}$$

From the user standpoint, all the three constitutive models (CM) presented in the previous sections are included in a single global constitutive model and, depending on the type of analysis being performed, the user is allowed to set up one of the three.

To simultaneously exemplify and present the parameters adopted in the simulations further explained, Table 6.2 presents the required parameters in each CM.

Table 6.2: Parameters required in each constitutive model.

Symbol	Units	Constitutive model					
		II		I/II_2D		I/II_3D	
Test[i]		A	B	A	B	A	B
-	-	_MODE_II		_MODE_I_II			
χ	MPa	-	-	16.0	6.0	15.0	6.0
c	MPa	17.5	6.5	18.5	7.0	17.5	6.5
c_g	MPa	-	-	-	-	10.0	2.0
σ_{dil}	MPa	-	-	2.0	2.0	-	-
$\tan$	-	-	-	0.8	0.8	0.8	0.8
$\tan_g$	-	-	-	-	-	0.2	0.05
$\tan_r$	-	-	-	0.5	0.5	0.1	0.1
$\tan$	-	-	-	0.05	0.05	-	-
α_χ	-	-	-	0.0	0.0	0.0	0.0
α_c	-	-0.4	0.5	-0.4	0.0	-0.4	0.0
$\alpha_{\tan\phi}$	-	-	-	0.0	0.0	0.0	0.0
G_f^I	N/mm	-	-	30.0	15.0	8.0	5.0
G_f^{II}	N/mm	40.0	15.0	45.0	25.0	18.0	10.0
k_1^e	MPa/mm	125.0	200.0	125.0	200.0	120.0	200.0
k_2^e	MPa/mm	1x10^6	1x10^6	100.0	150.0	100.0	150.0
k_3^e	MPa/mm	1x10^{6}[ii]	1x10^{6}[ii]	-	-	100.0	150.0

[i] A = CaReCo, B = GlRoTe.
[ii] only necessary in 3D analysis.
Legend: χ - Tensile strength; c, c_g - Cohesion in yield and plastic potential functions, respectively; σ_{dil} - Normal stress at which the dilatancy vanishes; $\tan\phi$, $\tan\phi_g$ - Friction angle in yield and plastic potential functions, respectively; $\tan\phi_r$ - Residual friction angle; $\tan\beta$ - Dilation angle; α_χ, α_c, $\alpha_{\tan\phi}$ - Tensile strength, cohesion and friction angle softening parameters, respectively; G_f^I, G_f^{II} - Fracture energy in modes I and II, respectively; k_1^e, k_2^e, k_3^e - Elastic tangential stiffness in l_1, l_2 and l_3 local directions, respectively.

6.2 Model validation: simulation details

The implemented constitutive model was validated using the experimental results of direct pullout tests of series C_LS_V2_T60 presented in Chapter 5, designated by CaReCo hereafter. In order to complement the validation, also an example from the literature (Bilotta et al., 2011a) was simulated, designated by GlRoTe.

Figure 6.4 shows the FEM mesh of CaReCo test (that test configuration was already shown in Figure 5.1c). Figure 6.5 shows not only the FEM mesh, but also the geometry

of the specimens and the test configurations of GlRoTe tests.

While they both consist of direct pullout tests, there are interesting differences between them, which justifies the simulation of both tests:

1. CaReCo tests use carbon FRP (CFRP) while GlRoTe use glass FRP (GFRP);
2. CaReCo specimens have rectangular FRP bars (laminates) while in the case of GlRoTe round FRP bars are used;
3. CaReCo and GlRoTe adopt test configurations which induce compression and tension, respectively, in the concrete specimens used;
4. The results of CaReCo include the pullout force *versus* post-peak slip curve (full range response) while the results of GlRoTe test are only up to peak pullout force;
5. In GlRoTe test strain gauges were used on the external surface of the GFRP along the bond length and their readings were provided while in CaReCo test such data are not available since no strain gauges were used.

While CaReCo tests are fully described in chapter 5, the following paragraphs summarize the important aspects about GlRoTe tets. GlRoTe specimens are prismatic plain concrete blocks (160×200×400 mm^3) in which a GFRP round bar with 8 mm of diameter was glued with an epoxy adhesive in a square groove with 14 mm side cut on the concrete block. To avoid premature failure of the specimen due to concrete cone formation near the top of the block, the anchorage length was initiated at 50 mm from the top. The bond between the FRP and the concrete (L_b) was extended 300 mm downwards. GlRoTe specimen was fixed to the base through two M20 threaded steel rods casted in the middle of the concrete block.

GlRoTe tests were monitored with a LVDT, which recorded the relative displacement, at the loaded-end, between the FRP and the concrete (slip), while the applied force F was recorded through a load cell. Additionally, in GlRoTe test, five strain gauges were glued along the GFRP bar to measure its axial strains.

Based on the material characterization conducted by the authors, a modulus of elasticity of 18.6 GPa, 51 GPa and 10.7 GPa was obtained in GlRoTe tests for concrete, FRP and adhesive, respectively.

Since in both types of experimental tests (CaReCo and GlRoTe) the specimens failed by debonding at FRP/adhesive interface, all the non-linearity of the system was located at that interface. Hence, all materials were assumed linear elastic using the properties referred above (a modulus of elasticity of 200 GPa was used for the steel elements).

Additionally, the interface elements were only used at the interface between FRP and adhesive, thus assuming that all the other regions of contact between different materials were fully bonded.

In order to assess the performance of the implemented interface constitutive model, two different FEM models were built for each type of test. Particularly, they differ essentially in the interface elements adopted, which were line 2D (L2D) and surface (S) interface elements.

Each FEM model was then run using either CM II or CM I/II, which resulted in four different FEM analyses for both CaReCo and GlRoTe tests. In the following paragraphs each single FEM model is described in detail. The parameters adopted in each constitutive model are presented in Table 6.2.

6.2.1 FEM model with interface L2D elements

In L2D FEM model, the direct pullout tests were modelled as a plane stress problem using the meshes represented in Figures 6.4a and 6.5c for CaReCo and GlRoTe specimens, respectively. For for both specimens the type of elements used was the same, namely: 4-node Serendipity plane stress elements with 2×2 Gauss-Legendre integration scheme for both concrete block and steel plate; 2-node frame 2D elements for both FRP bars and steel rods; 4-node interface L2D elements (see Figure 6.2a) with 2×1 Gauss-Lobatto integration scheme.

Both types of specimens were fixed to the corresponding testing machine by means of steel threaded rods. The only difference between them is that, while in the case of GlRoTe the rods were directly in contact with the concrete block, in CaReCo they were connected to a steel plate which in turn was in contact with the concrete block. Thus, the FEM support conditions in both types of tests consisted in fixing the bottom node of the steel rods. Additionally, unilateral contact supports were applied at the concrete block's base. Those restrain the downward movement in z direction (see Figures 6.4 and 6.5), but allow upward free movement. In CaReCo test, the effect of the pre-stress in the steel rods was simulated by applying a uniform temperature variation to the rod elements equivalent to the torque applied.

In both tests the load was applied by means of a vertical prescribed displacement (direction z – see Figures 6.4 and 6.5) in the top node of the FRP element.

6.2.2 FEM model with interface S elements

The S FEM model outlined in this section was built in order to test the S elements, thus deals with a 3D analysis with solid elements (see Figures 6.4b and 6.5d). Due to

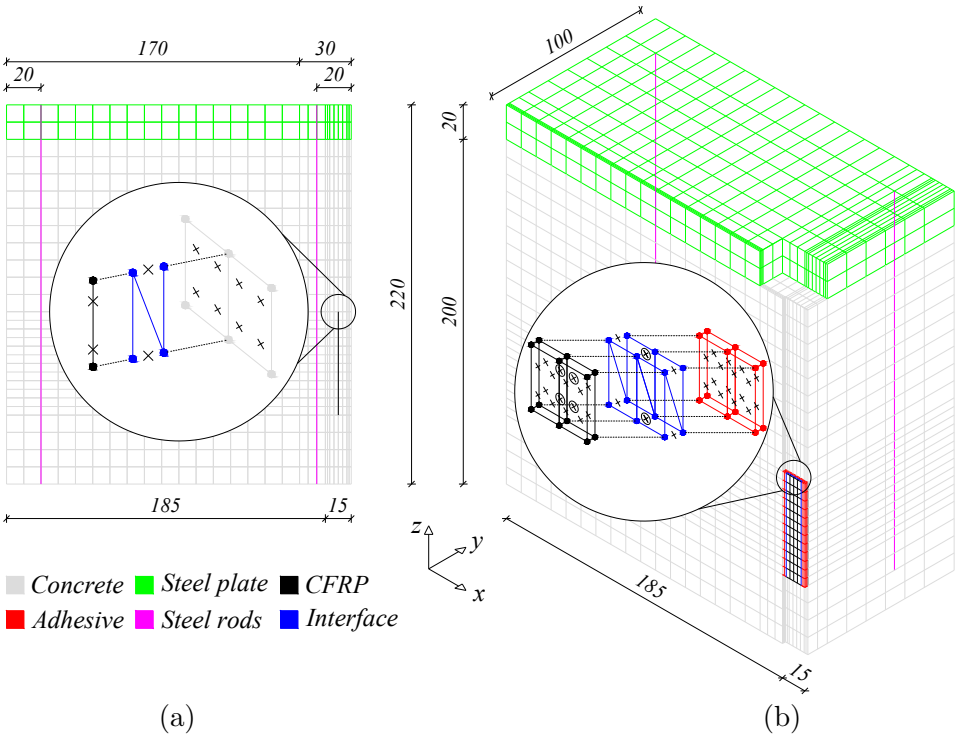

Figure 6.4: CaReCo direct pullout test: FEM mesh for analyses with interface line (a) and surface (b) elements. NOTE: dimensions in millimetres.

computational costs, in each case only half of the specimen was modelled since both specimens have a symmetry on the xz plan.

In both CaReCo and GlRoTe concrete block specimens, steel plate (in the case of CaReCo), adhesive and FRP were modelled using 8-node solid elements with $2 \times 2 \times 2$ Gauss-Legendre integration scheme. For the steel rods 2-node frame 3D elements were adopted. The interface elements were modelled with 8-node interface S elements (see Figures 6.2c) and 2×2 Gauss-Lobatto integration scheme.

The test boundary conditions were simulated in a way similar to that explained in the previous section. Additionally, in these 3D simulations the displacements following y axis were also restrained along the symmetry plan.

The load was also applied by means of a vertical prescribed displacement, in this case, in all the top nodes of the FRP.

6.2.3 Parameters of each interface constitutive model

The input parameters of each CM were defined in order to obtain numerical results that best fit the experimental results.

While in the analyses with CM II both L2D and S FEM models used the same input

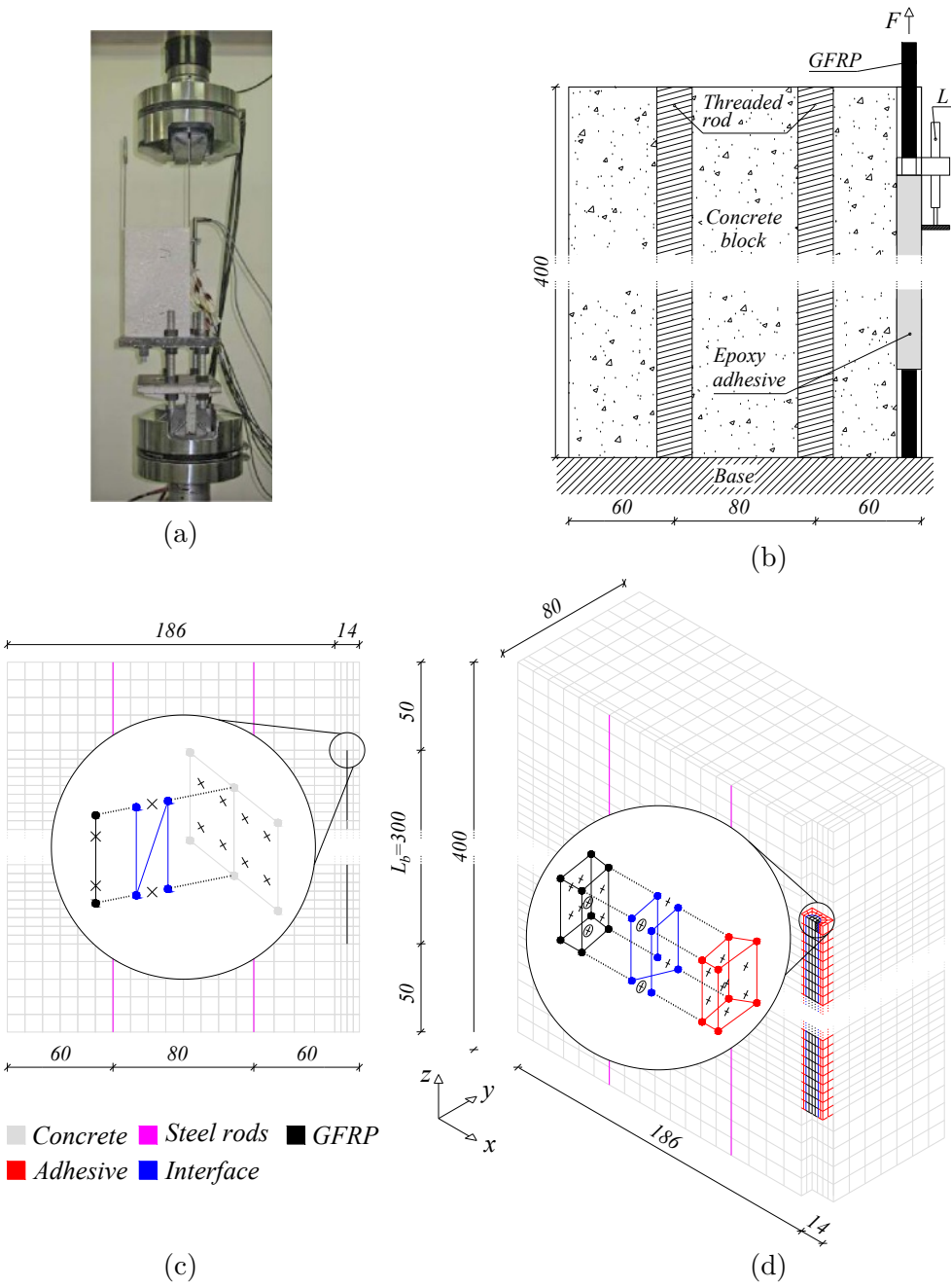

Figure 6.5: GlRoTe direct pullout test: (a) test photo (Bilotta et al., 2011a); (b) geometry and test setup scheme; FEM mesh for analyses with interface line (c) and surface (d) elements. NOTE: dimensions in millimetres.

parameters for the interface constitutive model, in CM I/II simulations the parameters used by each FEM model (2D and 3D) were slightly different as shown in Table 6.2.

These differences in the parameters used in each simulation with CM I/II are related to the influence that the behaviour in the normal direction has in the global response. In fact, the behaviour in the normal direction of FEM model with S elements is affected by the stiffness of the surrounding materials (adhesive and concrete) which can be seen as a "confinement" effect in the normal direction. Such influence does not exist when CM II is used since the behaviour in the normal direction is considered elastic in both L2D and S FEM models.

6.3 Model validation: numerical results

As previously referred, CaReCo test results include the post-peak response while GlRoTe test results provide FRP strains. Hence, for the sake of brevity, in the following sections the obtained results are presented and discussed only for CaReCo test. The only exceptions to this are related with the global response in terms of pullout force *versus* slip and the obtained FRP strains. The former is discussed for both (CaReCo and GlRoTe) in order to show the success of the FEM simulations. The later is presented and analysed in Section 6.3.4 for GlRoTe test only. Nevertheless it is worth to highlight that the trends and conclusions drawn in the following sections were very similar in the FEM simulation of both types of tests, thus are valid for both.

6.3.1 Experimental *versus* numerical results

Figures 6.6a and 6.6b present the results of all the eight FEM analyses conducted, in terms of the relationship between pullout force and slip at the loaded-end. Each graph includes the experimental results envelope and the results for the FEM analyses with L2D and S interface elements, as well as using both CM II and CM I/II.

For both types of test, in the case of L2D FEM models, the pullout force was taken from the top node of the FRP element (the node with imposed displacement) while the slip was taken from the top integration point of the top line interface element (see Figures 6.4a and 6.5c). In the case of S FEM models, the pullout force was computed as the sum of all the forces obtained in all top nodes of the FRP element (loaded nodes), while the slip was obtained from one of the top nodes of the top surface elements (see Figures 6.4b and 6.5d).

All the FEM analyses of CaReCo test successfully captured the three major stages of the experimental tests:

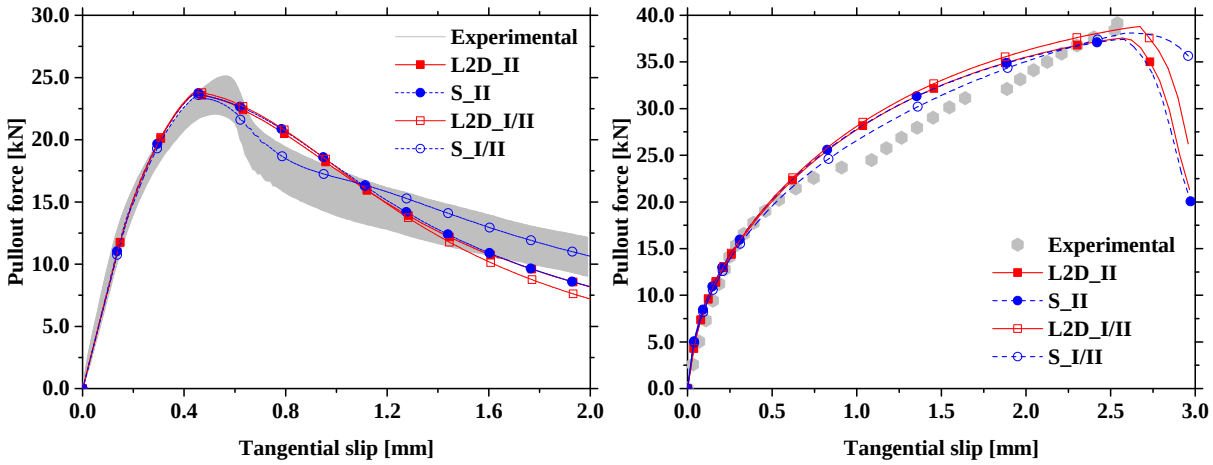

Figure 6.6: Tangential slip *versus* pullout force relationship for: (a) CaReCo tests; (b) GlRoTe tests.

- the initial stage, governed by the chemical bond between concrete, adhesive and CFRP. Typically this stage is characterized by an almost linear behaviour;

- the second stage, corresponding to the system's stiffness degradation that occurs as a consequence of the progressive loss of chemical bond;

- the third stage (post-peak branch), governed by the friction that exist between the CFRP laminate and the surrounding adhesive.

The most remarkable aspect is related with the FEM model using interface S elements and considering both fracture modes (CM I/II). This is the FEM model which better captured the abrupt force decrease at the beginning of the post-peak branch. This, once again, highlights the three-dimensional nature of the NSM FRP technique and the need for conducting 3D FEM analyses.

In GlRoTe, since the post-peak response was not registered, only the first two stages mentioned above were obtained. The FEM results were found to be very accurate in the first stage (up to a load level of 15-20 kN) as well as in terms of maximum pullout force prediction. Contrarily, the results in the middle region of the pullout force *versus* slip curve were not as accurate. However it is believed that this inaccuracy should be associated with acquisition difficulties during the experimental tests.

In addition, for GlRoTe test the beginning of the post-peak FEM curves is also included (see Figure 6.6b). This suggests a sudden pullout force decrease which can also justify the difficulty in capturing the post-peak response experimentally.

6.3.2 CM II *versus* CM I/II results

Figures 6.7 and 6.8 present the graphs with the evolution of interface's slips and stresses in the simulations with both L2D and S FEM models using CM II and CM I/II, respectively. In all curves the horizontal axis corresponds to the 60 mm bonded length. For the sake of readability, the graphs only include two curves in the pre-peak phase for load levels of 5 and 15 kN, the curve for the peak load (F_{fmax}) and two curves in the two post-peak phase for load levels of 20 and 10 kN.

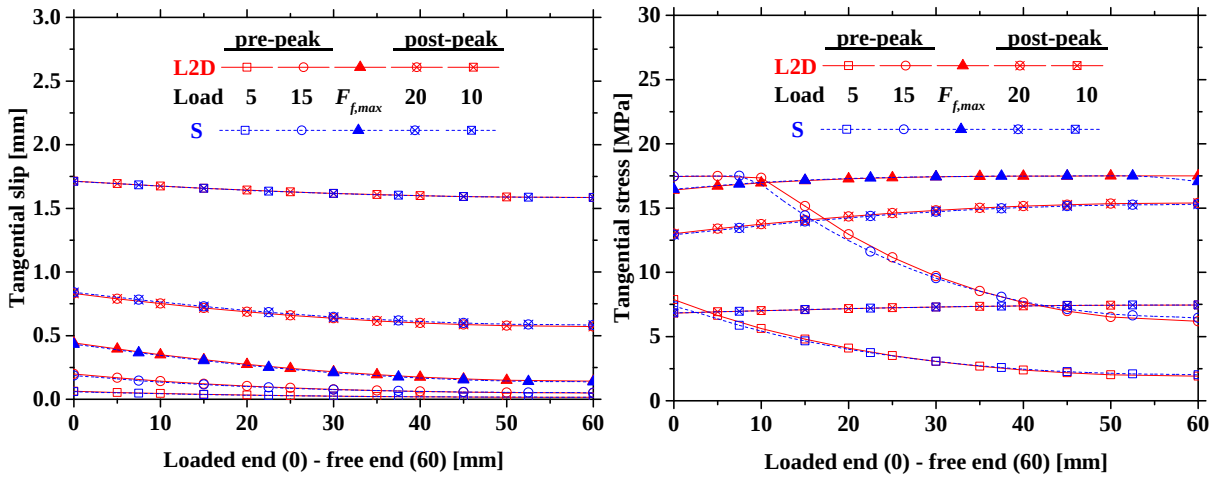

(a) (b)

Figure 6.7: Results of CaReCo FEM simulations using CM II and L2D or S interface elements: slip (a) and stress (b) along the interface in the loading direction.

In the FEM models with L2D interfaces, slips and stresses were monitored at the integration points of the L2D interface elements which coordinates coincide with those of the interfaces' nodes.

In order to get, for each parameter, a curve comparable to that obtained in the models with L2D interfaces, in FEM models with surface elements, slips and stresses were read at the middle integration points of the two middle columns of surface interface elements. The referred reading points are inscribed inside circles in Figure 6.4b.

Considering that there are differences in terms of numerical integration between 2D and 3D FEM models, the first conclusion that can be taken is that the results when using CM II are practically the same for both L2D and S FEM models, while they present some differences when using CM I/II. In fact, while in the FEM models using CM II the curves for L2D and S seem to be just slightly shifted (as a consequence of the referred differences in the numerical integration), in the FEM models using CM I/II they are actually different in terms of shape. This corroborates the previously referred influence of the normal direction behaviour.

Another conclusion that can be drawn is related with the curves of the parameters in the normal direction. Those are only presented for the FEM models using CM I/II and show that, when using L2D interface elements there is normal slip while when using S interface elements the normal slip is almost zero. As a consequence, the opposite occurs in terms of normal stress, i.e. when using L2D the normal stress is almost zero while when using S compressions are obtained in the normal direction. These findings corroborate the "confinement" effect that only exist in 3D simulations due to the influence of the surrounding materials stiffness, as previously mentioned (see Section 6.2.3).

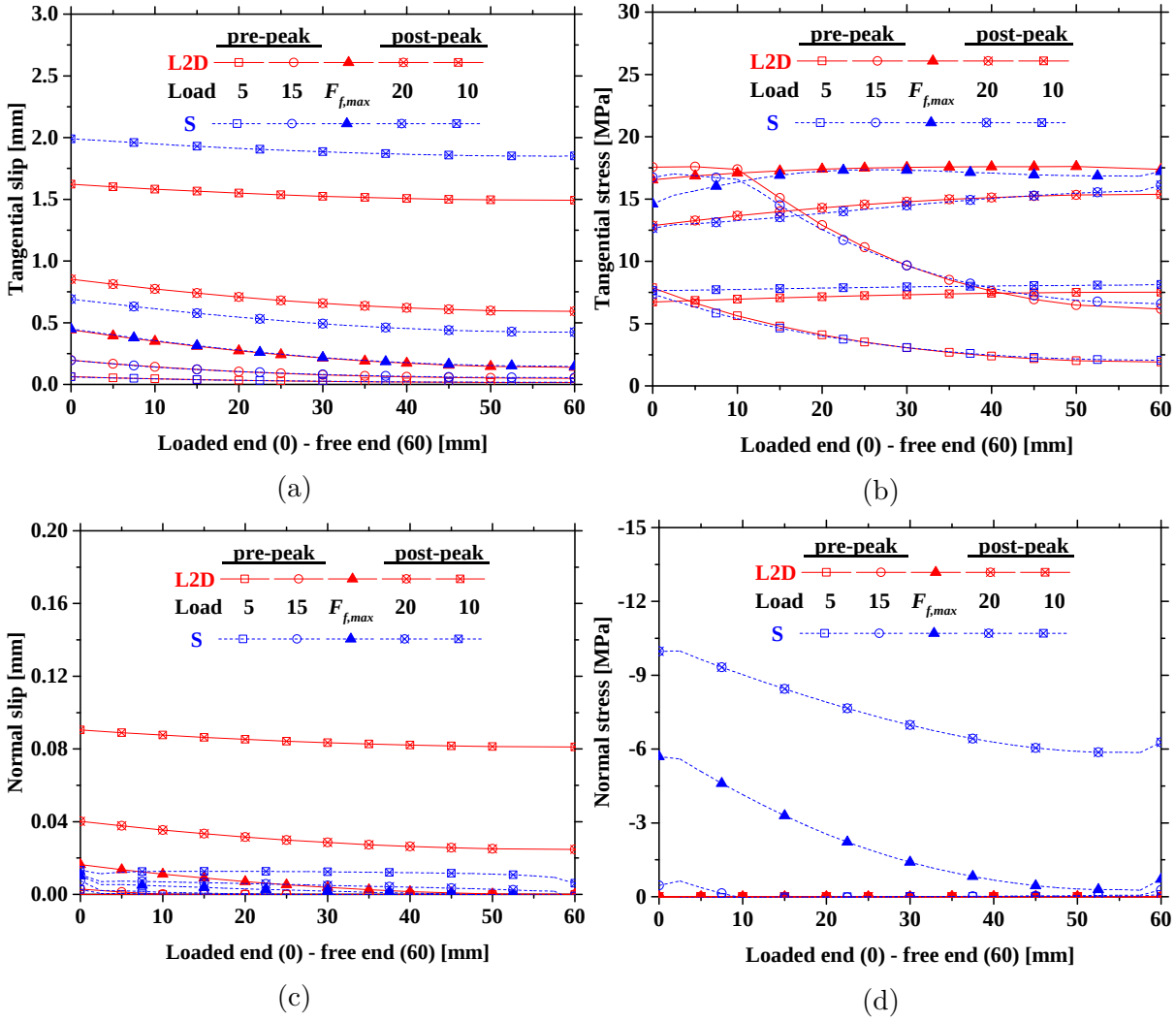

Figure 6.8: Results of CaReCo FEM simulations using CM I/II and L2D or S interface elements: slip (a) and stress (b) along the interface in the loading direction; slip (c) and stress (d) along the interface in the normal direction.

6.3.3 L2D *versus* S FEM models results

As previously mentioned, the bond phenomenon in the context of NSM FRP systems is intrinsically a three-dimensional problem, even though it has been shown that such problems can be successfully simulated using 2D FEM analyses. However, there are some important aspects, like the "confinement" effect shown before, that can only be simulated using 3D analyses. In addition to that, the type of information that can be obtained from 3D analyses is richer than that obtained in 2D analyses. As an example, Figure 6.9 presents the contour plots along the S interfaces for both 3D FEM models for the peak pullout force. This figure includes all the three components of slip and stress in the three local directions of the interface elements.

As a reference it should be said that the graphs of S interfaces presented earlier in Figures 6.7 and 6.8 correspond to the slips/stresses along the middle vertical line in each plot of Figure 6.9, which coincides with the location of the CFRP and L2D interfaces in the 2D models. Now, a global picture of what happens along the entire perimeter of the interface between CFRP and adhesive can also be seen.

Firstly, this figure shows that the width effect associated with the different boundary conditions was captured in the simulations. This is evident in the slips associated with l_1 direction (first plot in both Figures 6.9b and 6.9c). Those have a bell-shape format, in which the values are bigger in the middle region and lower in the extremities. Such an effect has already been described in the literature for the Externally Bonded Reinforcement (EBR) technique (Subramaniam et al., 2007).

Secondly, the effect of the eccentric location of the CFRP laminate is well captured by means of the interface-based modelling. For example, the slips in l_1 direction are slightly larger in the left side than in the right side, which correspond to inner and outer sides of the bond, respectively. This effect should be associated with the downwards movement of the concrete block as the CFRP is being pulled upwards, which should be smaller closer to the concrete block outer face.

Finally, it shows the different behaviour obtained when using CM I and I/II. This is more evident in the stresses along l_1 direction (fourth plot in both Figures 6.9b and 6.9c). This plots show that due to the elastic behaviour in the remaining direction when using CM II, the l_1 stresses are similar in all the three sides of the groove that were simulated. Contrarily, when using CM I/II the behaviour in all the three sides is quite different. In fact, comparing the region closer to the loaded end of each groove side, values of approximately 12, 14 and 16 MPa of tangential stress can be found, at maximum pullout force, for the outer, middle and inner sides of the groove, respectively. This numerical observation can be explained by the curvature that occurs at the CFRP during the pullout.

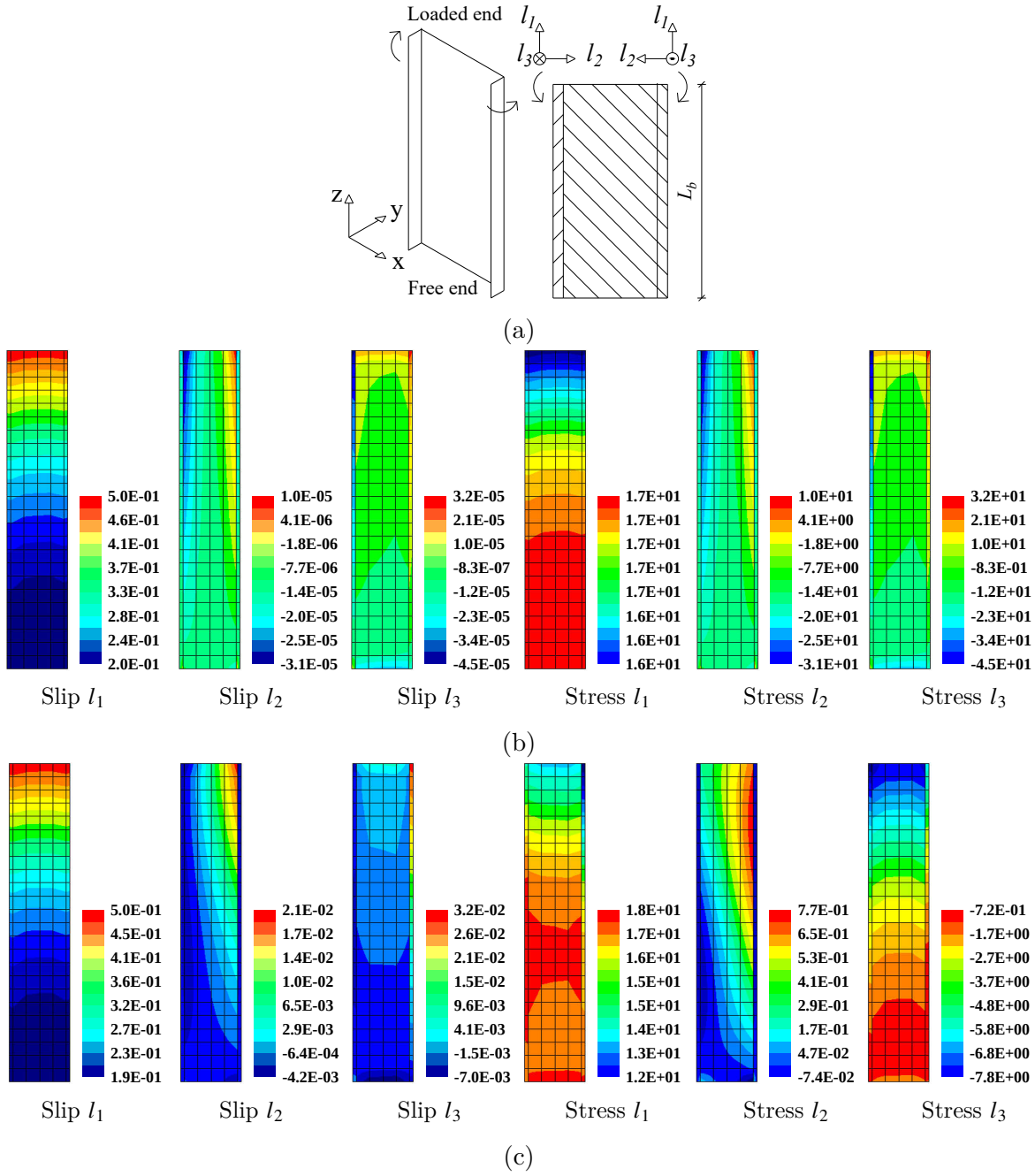

Figure 6.9: Contour plots of CaReCo tests at maximum pullout force for the S interface elements: (a) scheme; results for the FEM models using (b) CM II; (c) CM I/II. Note: slips appear in mm while stresses are in MPa.

This further highlights again the different loading stage of each region of the interface. In addition, with these plots, it is easy to identify the regions where the interface remains in the elastic range and those where it already entered the softening stage.

6.3.4 Experimental *versus* numerical FRP axial strain

In the FEM models with L2D interfaces, the GFRP strains were read at the integration points of the GFRP elements which do not coincide with their elements' nodes. This is related with the adopted integration schemes. In the FEM models with surface elements, the strains in the GFRP were obtained from the integration points closer to the centreline of the concrete block front face, in order to match the position of the strain gauges in the experimental tests (inscribed in circles in Figure 6.5d).

Figure 6.10 presents the evolution of the axial strain in the GFRP obtained in the experimental tests and the corresponding FEM results for different load levels. The FEM results include the 2D simulations using L2D interface elements and the 3D simulations with surface interface elements. Even though FEM simulations using both CM II and CM I/II were carried out, only one result is presented in order to do not overcharge the graphs. However, it should be stressed that the results were very similar in both cases.

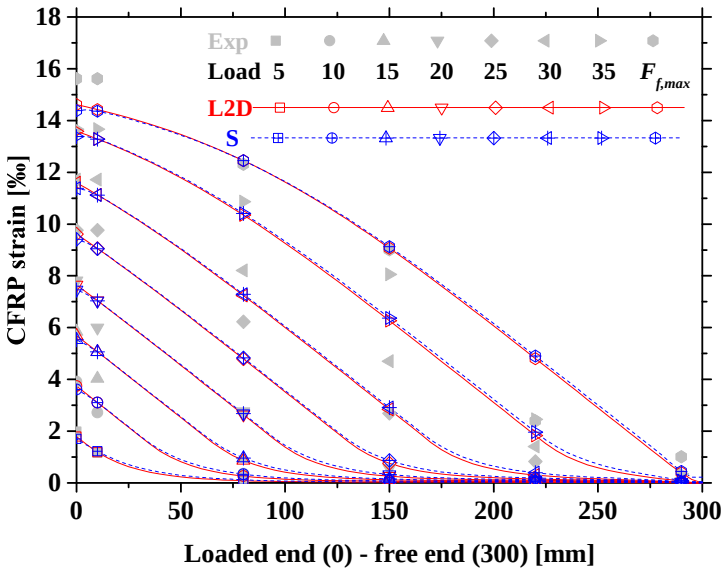

Figure 6.10: GFRP longitudinal strains obtained in GlRoTe experimental test and FEM simulations.

The strain gauges provide discrete readings in the regions of the GFRP bar where they were installed. Hence, all the curves presented in Figure 6.10 include a symbol to sign the regions where the strain gauges were located in the experimental tests. As it can be seen, up to a load level of 20 kN the results are quite satisfactory. After this load level

there are important differences between the experimental and numerical curves. However, this is true either in terms of strain (shown in Figure 6.10) or pullout force (shown in Figure 6.6b). In fact, as already mentioned in Section 6.3.1, the experimental response after the load level of 20 kN is quite unusual. Since there is a direct relationship between GFRP strain and pullout force, if the later is not well captured, the former will not be well captured as well. At the peak pullout force, again the numerical model captured very well the results obtained in the experimental test.

6.4 Conclusions

In this chapter, the major details about the implementation of an interface constitutive model (CM) in the FEMIX software were presented. It shall be emphasized that this CM is an adaptation of three already existing CM for quasi-brittle materials. One of the CM only allows accounting for fracture mode II while the other two CM deal with both fractures modes I and II in 2D or 3D FEM simulations.

Hence, the main contributions of the work presented in this chapter were, in the first place, bring those three CM to the field of NSM FRP systems' interfaces simulation. Secondly, implementing the three CM as a single CM in order to made available in FEMIX a single and complete interface model. The third contribution corresponds to the presentation of FEM simulations with the developed model, thus highlighting its validation.

The later contribution is specially important, since this work adds to the literature examples of 2D and 3D FEM simulations of pullout bond tests, either using only mode II of fracture or combining both modes I and II together. Additionally, it was shown that the implemented model can be used with line or surface interface elements in the framework of the well-known discrete crack analysis.

Regarding the results of the performed simulations, a good agreement between the experimental results and the numerical ones was found in all simulations performed in terms of pullout force *versus* slip. In addition, it was shown that further and more detailed information can be obtained when using surface interface elements. Namely, the effect of the eccentric location of the FRP bar is well captured by means of the 3D FEM simulations performed. The use of surface interfaces with CM I/II also allowed to verify that the bond behaviour varies, not only in the FRP tangential direction (load direction) but also in its normal direction (perpendicular to loading). In fact, the value of maximum tangential stress varies from the outer to the inner regions of the interface FRP/adhesive.

Finally, a comparison was made in terms of FRP axial strains where good agreement between experimental and numerical values was also obtained.

CHAPTER 7

Conclusions and future developments

At the end of each one of the previous chapters several specific conclusions were drawn, considering the specific part of the work developed. In the following sections, an overview of the work conducted is presented, the major results are highlighted and the suggestions for future developments are provided.

This work was developed in the context of strengthening concrete structures using Near-Surface Mounted (NSM) Fibre Reinforced Polymers (FRP) systems. Even though this technique has been increasingly investigated and used in the past decades, it was found the need of revisiting its foundations. In fact, while one of the new focus of NSM FRP research is its long-term behaviour and durability ("distant" issues), the truth is that the basilar concepts are not fully understood yet, which is a short-term concern. In particular, the way stresses are transferred from the existing concrete to the added FRP (bond behaviour), is not yet fully understood and cannot be accurately predicted.

Since the bond behaviour is the "smallest unit" of the NSM technique, of which all other aspects depend, if this is not dominated, uncertainty will propagate to every aspect of modelling, design and assessment. This was the main driver to the work presented in this thesis.

Many reasons can be pointed out to justify the insufficient knowledge that still exists in the bond behaviour of NSM FRP systems in concrete. Firstly, the complexity of the physical phenomena associated with NSM technique. It was shown in this work that there are several failure modes, specific of this technique, that should be considered. At least three at structural level and five at local (mesoscale) level.

But, if the complexity of the NSM technique can not be avoided, the same can not be said regarding the way it has been studied. In fact, the second big reason that can be pointed out is related with the lack of standard pullout tests. It is not reasonable that, being the pullout tests the major "tool" to study the bond behaviour, no standards exist normalizing it. The consequence of this absence of standard pullout tests is that it is very difficult to compare and try to extract useful information from different pullout tests conducted by different researchers.

7.1 Main conclusions

To reach the objectives proposed in the beginning of the present work, three different and complementary work components were defined. The following paragraphs describe the major outcomes of each work component.

7.1.1 Experimental component

The two major objectives defined for the experimental component of the thesis were successfully reached. Firstly, a database containing the details of the majority of pullout tests available in the literature was created and made available in the following website: www.frpbondata.civil.uminho.pt. From the work conducted, the following major conclusions can be drawn:

- from the critical analysis of the compiled database of pullout tests, it was possible to establish an updated state-of-the-art regarding the bond behaviour of NSM FRP systems in concrete;

- it is urgent to define standard pullout tests. This aspect is more critical in the case of DPT, which exist in a higher number of versions (sets of test configuration, specimen geometry and loading control, among other important aspects) compared with Beam Pullout Tests (BPT). Otherwise it is very difficult to analyse and compare the results obtained in DPT performed by different authors;

- the final solution regarding a standard DPT was found to be either a tension or compression single-shear test using a prismatic concrete specimen;

- the great majority of the experimental works' authors tend to report several failure modes since they look essentially to the final appearance of the specimens. However, it would be preferable to indicate only the critical one from the possible five

failure modes, namely, FRP rupture, cohesive failure within concrete or adhesive, or interfacial failure at either FRP/adhesive or adhesive/concrete interfaces.

Secondly, a campaign of Direct Pullout Tests (DPT) was conducted in order to contribute for the definition of a standard DPT. From the work conducted, the following major conclusions can be drawn:

- for the conditions analysed (materials properties and test/specimens configuration), both tension and compression single-shear DPT lead to very similar results;
- the assessment of the impact of using three different sides in the same specimen was found to be inconclusive. Only in tension tests this seems to be an important parameter, but more experimental tests are necessary to clarify whether or not this is true and, if so, why this is important;
- apparently, the torque in the steel rods in compression DPT does not affect the bond behaviour. This trend is also justified by the unbonded zone kept before the bonded zone;
- regarding the load speed used in the tests, it was verified that controlling the tests by imposing a loading rate of 2 $\mu m/s$ in the loaded end section, the full response can be obtained in a reasonable time and with no impact on the obtained results.

7.1.2 Analytical component

The main objective defined for the analytic component of the thesis was the definition of a bond strength model for NSM FRP systems in concrete. This objective was successfully achieved through the two tasks that were defined. Firstly, bond strength models were sought and validated on the database of pullout tests compiled. Secondly, for those bond strength models, a reliability analysis was conducted in order to provide them with the necessary safety features, so that they could be used for designing bond.

From the work conducted to achieve this objective, the following major conclusions can be drawn:

- due to the difficulty in jointly analyse and compare the pullout tests available in the compiled database, it was not possible to propose a new analytic bond strength model. Alternatively, two analytic bond strength models found in two of the most important guidelines, namely, American Concrete Institute (ACI) and Standards Australia (SA), for NSM FRP systems in concrete were analysed;

- by testing both ACI and SA bond strength models in the database of pullout tests, it was found that they need to be improved in order to become more accurate. Specifically, they need to be able of accounting for all the existing failure modes and be made FRP cross-section independent, among other improvements;

- two different improvements were made in ACI and SA bond strength models, namely:

  (i) firstly, both models were recalibrated;

  (ii) secondly, in the case of ACI, an alternative expression to estimate the average bond strength was also proposed. In the case of SA, it was also made FRP cross-section independent by considering the groove rather than the FRP perimeter as reference for estimating the failure perimeter;

- alternative bond strength models were proposed based on Data Mining (DM) algorithms. Those are known to be capable of modelling phenomena of high complexity, which is the case of the NSM technique. Thus, they were found to be more accurate than the ones included in ACI and SA, both when considering the same input parameters as defined in ACI and SA or considering different sets of input parameters;

- since the DM based models need a computational environment to be applied, in the same website that was developed to store the compiled database of pullout tests, a tool was made available to allow the use of DM based models by anyone (no knowledge on DM is required to use these models);

- all the bond strength models analysed/proposed in this work were adapted to be used in the design of NSM FRP systems in concrete, according to the Eurocodes philosophy. This includes the ACI and SA models, their improved/recalibrated versions and also the DM based models. The partial safety factors were calibrated to consider both material properties variability and model uncertainty.

7.1.3 Numerical component

The main objective defined for the numerical component of the thesis was the proposal of an interface constitutive model to allow the numerical simulation of the interfaces existing in NSM FRP systems. This objective was successfully achieved by the adaptation of an existing constitutive model for quasi-brittle materials.

From the work conducted to achieve this objective, the following major conclusions can be drawn:

- the constitutive model, that works with zero-thickness interface elements, allows accounting for fracture mode II (interfacial sliding) or the combination of fracture modes I and II (interfacial sliding and opening), both in 2D or 3D numerical simulations;

- while the constitutive models commonly used in the past are based on assuming *a priori* an analytical expression for the interface bond-slip law, the one developed in this work is conceived within the general framework of the classical Flow Theory of Plasticity where the interface bond-slip law is only obtained *a posteriori*;

- the results obtained in the numerical simulations performed to validate the implemented constitutive model were found very good in terms of capturing the global behaviour of the tests (described by the relationship between pullout force and loaded end slip);

- since it is known that the NSM technique has an inherent three-dimensional nature, the possibility of performing 3D simulation is one of the key features of the implemented constitutive model. The importance of this was shown in the numerical simulations conducted, since the 3D simulations attained the best results.

7.2 Future developments

Since the most critical aspect verified in the present thesis was the absence of a standard DPT, the future developments to be suggested are also conditioned by solving this issue. In fact, while a database of pullout tests was compiled/analysed and bond strength models were analysed and transformed into design models, the truth is that all this work is just a compromise and/or short-term solution, considering the existing state of knowledge.

Ideally, in the near future, a standard DPT will be defined. Then, a new database of pullout tests will be gradually built. Since this new database will consist of DPT made in "standard" conditions, it will be possible to analyse/compare the DPT made by different authors, to validate and update the existing state-of-the-art on the bond behaviour and then to suggest new bond strength models or to analyse/recalibrate the existing ones.

In other words, the work conducted in this thesis should be repeated again when a new and more reliable database of pullout tests is made available. This depends and requires the contribution of all research community working in this field. To contribute for this challenge, tools like the website developed in this work, are a privileged platform to promote the interaction between the research community. In fact, if the website database

is continuously increased, as new pullout tests become available, it would be easier/faster to develop and validate new bond strength models in the future.

7.2.1 Experimental component

While the focus should be on defining a standard DPT, the amount of experimental data available is still very low. Hence, it is necessary to continue performing pullout tests, specially using combinations of parameters and materials that were not tested yet. Some examples of important aspects that were not covered by the experimental campaign described in this thesis nor in the literature reviewed, are:

- experimental tests with different groove dimension in order to provide an upper limit to groove's width and also to update the groove to FRP shape ratios since the former does not exist in the existing guidelines while the later was found to be outdated;

- an experimental campaign with different unbonded lengths (between specimen's top and loaded end section) and concrete strengths in order to clarify which one is responsible for obtaining similar maximum pullout forces in tension and compression DPT;

- tension DPT considering different locations of the steel threaded rods (with different cover) should be conducted in order to verify if the different results obtained while testing on the lateral or bottom side of the concrete specimens are a consequence of the presence of the steel rods.

Additionally, further research is necessary to establish a standard method to define and describe the failure modes observed in pullout tests.

7.2.2 Analytical component

Considering the amount of parameters which can influence the bond behaviour of NSM FRP systems in concrete, it can be said that an holistic model for predicting their strength will be very difficult to obtain, even if, as already referred, a new database of "standard" DPT is available.

Nevertheless, that task need to be done in order to achieve better and more accurate design bond strength models. As a contribute for this, the following suggestions are provided:

- the ACI and SA bond strength models need to be upgraded with new features in order to become more accurate and less sensitive to the value of the bonded length, since it was found that their predictive capacity seems to be influenced by it;
- there are failure modes which are not explicitly accounted for in ACI and SA bond strength models. This gap should also be bridged in the future;
- while there are three materials involved, both ACI and SA bond strength models do not include variables representing the mechanical parameters of all the materials involved. Probably one way to account for all the failure modes associated with the materials would be using such variables in the bond strength models;
- a large scale analysis of the probabilistic models for FRP properties is paramount for defining reliable design code.

7.2.3 Numerical component

The numerical simulations presented in this work were focused in pullout tests, since those were the type of NSM FRP applications discussed in this thesis. On the other hand, the simulations conducted were found enough to validate the developed interface constitutive model, thus no further simulations were made.

Nevertheless, the developed model should be further explored and validated in the future. Specifically, the simulation of scenarios in which the type of stresses to which the interface will be subject is not predominantly tangential (as in the DPT simulated in this thesis). Hence, the following numerical simulations are suggested:

- BPT, beams/slabs and beam-column joints, all made of concrete strengthened (in shear and/or flexure) with NSM FRP systems, are examples of simulations of increasing difficulty that could be made to further validate the constitutive model;
- since the constitutive model can be used in any type of numerical simulation using zero-thickness interface elements, the possibilities to test it are not limited to the context of NSM FRP systems in concrete, thus should be explored.

This page was left blank intentionally.

Bibliography

ACI, 2008. Guide for the design and construction of externally bonded FRP systems for strengthening concrete structures. 4402R-08, American Concrete Institute, Farmington Hills, MI, USA.

Al-Mahmoud, F., Castel, A., François, R., Tourneur, C., 2011. Anchorage and tension-stiffening effect between near-surface-mounted CFRP rods and concrete. Cement and Concrete Composites 33, 346–352.

Atadero, R.A., Karbhari, V.M., 2005. Probabilistic based design for FRP strengthening of reinforced concrete. Special Publication (ACI) 230, 723–742.

Bakis, C., Bank, L., Brown, V., Cosenza, E., Davalos, J., Lesko, J., Machida, A., Rizkalla, S., Triantafillou, T., 2002. Fiber-reinforced polymer composites for construction – state-of-the-art review. Journal of Composites for Construction 6, 73–87.

Barros, J., Costa, I., 2010. Bond tests on near surface reinforcement strengthening for concrete structures. Technical Report. Civil Engineering Department, University of Minho, Guimarães, Portugal.

Bilotta, A., Ceroni, F., Di Ludovico, M., Nigro, E., Pecce, M., Manfredi, G., 2011a. Bond efficiency of EBR and NSM FRP systems for strengthening concrete members. Journal of Composites for Construction 15, 757–772.

Bilotta, A., Ceroni, F., Di Ludovico, M., Nigro, E., Pecce, M., Manfredi, G., 2012. Experimental bond test on concrete members strengthened with NSM FRP systems: influence of groove dimensions and surface treatment, in: CICE 2012 – Rome, Italy.

Bilotta, A., Ceroni, F., Nigro, E., Pecce, M., 2014. Strain assessment for the design of NSM FRP systems for the strengthening of RC members. Construction and Building Materials 69, 143–158.

Bilotta, A., Faella, C., Martinelli, E., Nigro, E., 2013. Design by testing procedure for intermediate debonding in EBR FRP strengthened RC beams. Engineering Structures 46, 147–154.

Bilotta, A., Ludovico, M.D., Nigro, E., 2011b. FRP-to-concrete interface debonding: experimental calibration of a capacity model. Composites Part B: Engineering 42, 1539–1553.

Blaschko, M., 2003. Bond behaviour of CFRP strips glued into slits, in: FRPRCS-6 – Singapore.

Caballero, A., Willam, K.J., Carol, I., 2008. Consistent tangent formulation for 3d interface modeling of cracking/fracture in quasi-brittle materials. Computer Methods in Applied Mechanics and Engineering 197, 2804–2822.

Caggiano, A., Etse, G., Martinelli, E., 2011. Interface model for fracture behaviour of fiber-reinforced cementitious composites (FRCCs). European Journal of Environmental and Civil Engineering 15, 1339–1359.

Caggiano, A., Martinelli, E., 2012. Fracture-based model for mixed mode cracking of FRP strips glued on concrete, in: Bond in Concrete 2012, Brescia, Italy.

Caggiano, A., Martinelli, E., 2013. A fracture-based interface model for simulating the bond behaviour of FRP strips glued to a brittle substrate. Composite Structures 99, 397–403.

Capozucca, R., 2013. Analysis of bond-slip effects in RC beams strengthened with NSM CFRP rods. Composite Structures 102, 110–123.

Carol, I., Prat, P., López, C., 1997. Normal/shear cracking model: application to discrete crack analysis. Journal of Engineering Mechanics 123, 765–773.

CEN, 2002. Eurocode 0: Basis of structural design. EN 1990:2002 E, Comité Européen de Normalisation, Bruxeles.

CEN, 2004. Eurocode 2: Design of concrete structures. EN 1992-1-1:2004 E, Comité Européen de Normalisation, Bruxeles.

CEN, 2013. Strengthening with FRP: Draft version. TC250-SC2-WG1-TG1-N17, Comité Européen de Normalisation, Bruxeles.

Ceroni, F., Barros, J., Pecce, M., Ianniciello, M., 2013. Assessment of nonlinear bond laws for near-surface-mounted systems in concrete elements. Composites Part B: Engineering 45, 666–681.

Ceroni, F., Pecce, M., Bilotta, A., Nigro, E., 2012. Bond behavior of FRP NSM systems in concrete elements. Composites Part B: Engineering 43, 99–109.

Chojaczyk, A.A., Teixeira, A.P., Neves, L.C., Cardoso, J.B., Guedes Soares, C., 2015. Review and application of artificial neural networks models in reliability analysis of steel structures. Structural Safety 52, Part A, 78–89.

CNR, 2012. Istruzioni per la progettazione, l'esecuzione ed il controllo di interventi di consolidamento statico mediante l'utilizzo di compositi fibrorinforzati. CNR-DT 200 R1/2012, National Research Council, Rome, Italy.

Coelho, M., Sena Cruz, J., Dias, S., Miranda, T., 2013. Evaluation of code formulations for NSM CFRP bond strength of RC elements, in: FRPRCS-11 – Guimarães, Portugal.

Coelho, M., Sena-Cruz, J., Neves, L., 2015. A review on the bond behavior of FRP NSM systems in concrete. Construction and Building Materials 93, 1157–1169.

Cortes, C., Vapnik, V., 1995. Support-vector networks. Machine Learning 3, 273–297.

Cortez, P., 2010. Data mining with neural networks and support vector machines using the R/rminer tool. Chapter 4 of Lecture Notes in Computer Science, Springer Berlin Heidelberg.

Cortez, P., Embrechts, M.J., 2013. Using sensitivity analysis and visualization techniques to open black box data mining models. Information Sciences 225, 1–17.

CSA, 2006. Canadian highway bridge design code. CAN/CSA S6-06, Canadian Standards Association, Canada.

De Lorenzis, L., 2002. Strengthening of RC structures with near surface mounted FRP rods. Phd thesis. University of Leece, Italy.

De Lorenzis, L., Lundgren, K., Rizzo, A., 2004. Anchorage length of near-surface mounted fiber-reinforced polymer bars for concrete strengthening – experimental investigation and numerical modeling. ACI Structural Journal 101, 269–78.

De Lorenzis, L., Rizzo, A., La Tegola, A., 2002. A modified pull-out test for bond of near-surface mounted frp rods in concrete. Composites Part B: Engineering 33, 589–603.

De Lorenzis, L., Teng, J.G., 2007. Near-surface mounted FRP reinforcement: An emerging technique for strengthening structures. Composites Part B: Engineering 38, 119–143.

Doran, B., Yetilmezsoy, K., Murtazaoglu, S., 2015. Application of fuzzy logic approach in predicting the lateral confinement coefficient for RC columns wrapped with CFRP. Engineering Structures 88, 74–91.

Echeverria, M., Perera, R., 2013. Three dimensional nonlinear model of beam tests for bond of near-surface mounted FRP rods in concrete. Composites Part B: Engineering 54, 112–124.

El-Hacha, R., Rizkalla, S., 2004. Near-surface-mounted fiber-reinforced polymer reinforcements for flexural strengthening of concrete structures. ACI Structural Journal 101, 717–26.

Çevik, A., 2011. Modeling strength enhancement of FRP confined concrete cylinders using soft computing. Expert Systems with Applications 38, 5662–5673.

Çevik, A., Kurtoğlu, A., Bilgehan, M., Gülşan, M., Albegmprli, H., 2015. Support vector machines in structural engineering: a review. Journal of Civil Engineering and Management 21, 261–281.

Fayyad, U., Piatesky-Shapiro, G., Smyth, P., 1996a. From data mining to knowledge discovery: an overview. Advances in Knowledge Discovery and Data Mining, AAAI Press / The MIT Press, Cambridge MA.

Fayyad, U., Piatetsky-Shapiro, G., Smyth, P., 1996b. From data mining to knowledge discovery in databases. AI Magazine 17, 37–54.

Fernandes, P., 2016. Bond behaviour of NSM CFRP-concrete systems: durability and quality control. PhD Thesis. University of Minho, Portugal.

Fernandes, P., Silva, P., Sena-Cruz, J., 2015. Bond and flexural behavior of concrete elements strengthened with NSM CFRP laminate strips under fatigue loading. Engineering Structures 84, 350–361.

Fu, H., Erki, M., Seckin, M., 1991. Review of effects of loading rate on reinforced concrete. Journal of Structural Engineering 117, 3660–3679.

Garzón-Roca, J., Marco, C.O., Adam, J.M., 2013. Compressive strength of masonry made of clay bricks and cement mortar: Estimation based on neural networks and fuzzy logic. Engineering Structures 48, 21–27.

Gomes, S., Neves, L., Dias-da Costa, D., Fernandes, P., Júlio, E., 2013. Probabilistic models for mechanical properties of prefabricated CFRP, in: 11^{th} fiber reinforced polymers for reinforced concrete structures (FRPRCS11), Guimarães, Portugal.

Hassan, T., Rizkalla, S., 2004. Bond mechanism of near-surface-mounted fiber-reinforced polymer bars for flexural strengthening of concrete structures. ACI Structural Journal 101, 830–839.

Haykin, S., 2009. Neural networks and learning machines. Pearson Education, Inc., Upper Saddle River, New Jersey.

IPQ, 2005. Concrete. Part 1: Specification, performance, production and conformity. NP EN 206-1, Portuguese Quality Institute, Lisbon, Portugal.

IPQ, 2011. Testing hardened concrete. Part 3: Compressive strength of test specimens. EN 12390-3, Portuguese Quality Institute, Lisbon, Portugal.

ISO, 1997. Plastics - Determination of tensile properties - Part 5: Test conditions for unidirectional fibre reinforced plastic composites. ISO 527-5, International Organization for Standardization, Genève, Switzerland.

ISO, 2012. Plastics – Determination of tensile properties – Part 2: Test conditions for moulding and extrusion plastics. ISO 527-2, International Organization for Standardization, Genève, Switzerland.

JCSS, 2001. Probabilistic model code. The Joint Committee on Structural Safety.

Kalupahana, W., 2009. Anchorage and bond behaviour of near surface mounted fibre reinforced polymer bars. PhD Thesis. University of Bath, United Kingdom.

Kang, J.Y., Park, Y.H., Park, J.S., You, Y.J., Jung, W.T., 2005. Analytical evaluation of RC beams strengthened with near surface mounted CFRP laminates, in: FRPRCS-7 – Kansas City, Missouri, USA.

Kotynia, R., 2012. Bond between FRP and concrete in reinforced concrete beams strengthened with near surface mounted and externally bonded reinforcement. Construction and Building Materials 32, 41–54.

Lee, D., Cheng, L., 2013. Bond of NSM systems in concrete strengthening – Examining design issues of strength, groove detailing and bond-dependent coefficient. Construction and Building Materials 47, 1512–1522.

Lee, D., Hui, J., Cheng, L., 2012. Bond characteristics of NSM reinforcement in concrete due to adhesive type and surface configuration, in: CICE 2012 – Rome, Italy.

Lee, S., Lee, C., 2014. Prediction of shear strength of FRP-reinforced concrete flexural members without stirrups using artificial neural networks. Engineering Structures 61, 99–112.

LNEC, 1993. Concrete — Determination of the elasticity young modulus under compression. E397-1993, National Laboratory of Civil Engineering, Lisbon, Portugal.

Lundqvist, J., Nordin, H., Taljsten, B., Olofsson, T., 2005. Numerical analysis of concrete beams strengthened with CFRP – a study of anchorage lengths, in: International Symposium on Bond Behaviour of FRP in Structures (BBFS2005), Hong Kong, China.

Macedo, L., Costa, I., Barros, J., 2008. Assessment of the influence of the adhesive properties and geometry of CFRP laminates in the bond behavior, in: BE2008 - Betão Estrutural 2008. Guimarães, Portugal.

Martin, T., Cleland, D., Robinson, D., Taylor, S., 2012. Experimental study of bond stress for near surface mounted basalt fibre reinforced polymer strips on concrete, in: Bond in Concrete 2012 – Brescia, Italy.

Martinelli, E., Caggiano, A., 2014. A unified theoretical model for the monotonic and cyclic response of FRP strips glued to concrete. Polymers 6, 370–381.

Martins, F.F., Miranda, T.F.S., 2012. Estimation of the rock deformation modulus and RMR based on data mining techniques. Geotechnical and Geological Engineering 30, 787–801.

Merdas, A., Fiorio, B., Chikh, N., 2012. Bond behavior of carbon laminate strips and rods into concrete by pullout-bending tests, in: Bond in Concrete 2012 – Brescia, Italy.

Mitchell, P., 2010. Freeze-thaw and sustained load durability of near surface mounted FRP strengthened concrete. Msc thesis. Queen's University, Canada.

Mohamed Ali, M.S., Oehlers, D.J., Griffith, M.C., Seracino, R., 2008. Interfacial stress transfer of near surface-mounted frp-to-concrete joints. Engineering Structures 30, 1861–1868.

Monti, G., Alessandri, S., Santini, S., 2009. Design by testing: a procedure for the statistical determination of capacity models. Construction and Building Materials 23, 1487–1494.

Monti, G., Santini, S., 2002. Reliability-based calibration of partial safety coefficients for fiber-reinforced plastic. Journal of Composites for Construction 6, 162–167.

Novidis, D., Pantazopoulou, S., 2008a. Beam pull out tests of NSM-FRP and steel bars in concrete, in: CICE2008 – Zurich, Switzerland.

Novidis, D., Pantazopoulou, S.J., Tentolouris, E., 2007. Experimental study of bond of NSM-FRP reinforcement. Construction and Building Materials 21, 1760–1770.

Novidis, D.G., Pantazopoulou, S.J., 2008b. Bond tests of short NSM-FRP and steel bar anchorages. Journal of Composites for Construction 12, 323–333.

Oehlers, D.J., Haskett, M., Wu, C., Seracino, R., 2008. Embedding NSM FRP plates for improved IC debonding resistance. Journal of Composites for Construction 12, 635–642.

Palmieri, A., Matthys, S., Barros, J., Costa, I., Bilotta, A., Nigro, E., Ceroni, F., szabó, Z., Balázs, G., 2012a. Bond of NSM FRP strengthened concrete: round robin test initiative, in: CICE 2012, Rome, Italy.

Palmieri, A., Matthys, S., Taerwe, L., 2012b. Double bond shear tests on NSM FRP strengthened members, in: CICE 2012, Rome, Italy.

Parretti, R., Nanni, A., 2004. Strengthening of RC members using near-surface mounted FRP composites: design overview. Advances in Structural Engineering 7, 469–483.

R, C.T., 2012. R: A language and environment for statistical computing, in: R Foundation for Statistical Computing – Vienna, Austria.

Rashid, R., Oehlers, D.J., Seracino, R., 2008. IC debonding of FRP NSM and EB retrofitted concrete: plate and cover interaction tests. Journal of Composites for Construction 12, 160–167.

RILEM, 1982. RC5: Bond test for reinforcement steel. 1. Beam test. Recommendations for the testing and use of constructions materials.

RILEM, 1983. RC 6: Bond test for reinforcement steel. 2. Pull-out test. Recommendations for the testing and use of constructions materials.

RILEM, 2015. Design procedures for the use of composites in strengthening of reinforced concrete structures. State-of-the-art report of the RILEM technical committee 234-DUC, Springer Netherlands.

SA, 2008. Design handbook for RC structures retrofitted with FRP and metal plates: beams and slabs. HB 305-2008, Standards Australia GPO Box 476, Sydney, NSW 2001, Australia.

Sasmal, S., Khatri, C.P., Ramanjaneyulu, K., Srinivas, V., 2013. Numerical evaluation of bond-slip relations for near-surface mounted carbon fiber bars embedded in concrete. Construction and Building Materials 40, 1097–1109.

Sena-Cruz, J., 2004. Strengthening of concrete structures with near-surface mounted CFRP laminate strips. PhD Thesis. University of Minho, Portugal.

Sena-Cruz, J., Barros, J., 2004. Bond between near-surface mounted carbon-fiber-reinforced polymer laminate strips and concrete. Journal of Composites for Construction 8, 519–527.

Sena-Cruz, J., Barros, J., Azevedo, A., 2004. Elasto plastic multi fixed smeared crack model for concrete. Technical Report 04-DEC/E-05. Civil Engineering Department, University of Minho, Guimarães, Portugal.

Sena-Cruz, J., Barros, J., Azevedo, A., Gouveia, A., 2007. Numerical simulation of the nonlinear behavior of RC beams strengthened with NSM CFRP strips, in: CNME 2007-Congress on Numerical Methods in Engineering and XXVIII CILAMCE – Iberian Latin American Congress on Computational Methods in Engineering, FEUP, Porto, Portugal.

Sena-Cruz, J., Barros, J., Gettu, R., Azevedo, A., 2006. Bond behavior of near-surface mounted CFRP laminate strips under monotonic and cyclic loading. Journal of Composites for Construction 10, 295–303.

Seo, S.Y., Feo, L., Hui, D., 2013. Bond strength of near surface-mounted FRP plate for retrofit of concrete structures. Composite Structures 95, 719–727.

Seracino, R., Jones, N., Ali, M., Page, M., Oehlers, D., 2007a. Bond strength of near-surface mounted FRP strip-to-concrete joints. Journal of Composites for Construction 11, 401–409.

Seracino, R., Saifulnaz, M., Oehlers, D., 2007b. Generic Debonding Resistance of EB and NSM Plate-to-Concrete Joints. Journal of Composites for Construction 11, 62–70.

Sharaky, I.A., Barros, J.A.O., Torres, L., 2013. FEM-based modelling of NSM-FRP bond behaviour, in: FRPRCS-11, Guimarães, Portugal.

Shen, D., Shi, H., Ji, Y., Yin, F., 2015. Strain rate effect on effective bond length of basalt FRP sheet bonded to concrete. Construction and Building Materials 82, 206–218.

Shield, C., French, C., Milde, E., 2005. The effect of adhesive type on the bond of NSM tape to concrete, in: FRPRCS7, Kansas City, Missouri, USA, pp. 355–72.

Soliman, S.M., El-Salakawy, E., Benmokrane, B., 2011. Bond performance of Near-Surface-Mounted FRP bars. Journal of Composites for Construction 15, 103–111.

Subramaniam, K., Carloni, C., Nobile, L., 2007. Width effect in the interface fracture during shear debonding of FRP sheets from concrete. Engineering Fracture Mechanics 74, 578–94.

Teng, J.G., De Lorenzis, L., Wang, B., Li, R., Wong, T., Lam, L., 2006. Debonding failures of RC beams strengthened with near surface mounted CFRP strips. Journal of Composites for Construction 10, 92–105.

Teng, J.G., Zhang, S.S., Dai, J.G., Chen, J.F., 2013. Three-dimensional meso-scale finite element modeling of bonded joints between a near-surface mounted FRP strip and concrete. Computers & Structures 117, 105–117.

Thorenfeldt, E., 2007. Bond capacity of CFRP strips glued to concrete in sawn slits, in: FRPRCS-8, Patras, Greece.

Tinoco, J., Gomes Correia, A., Cortez, P., 2011. Application of data mining techniques in the estimation of the uniaxial compressive strength of jet grouting columns over time. Construction and Building Materials 25, 1257–1262.

Ventura, A., Barros, J., Azevedo, A., Sena-Cruz, J., 2008. Multi-fixed smeared 3d crack model to simulate the behavior of fiber reinforced concrete structures, in: CCC2008 – Challenges for Civil Construction, FEUP, Porto, Portugal.

Wang, B., Teng, J.G., Lorenzis, L.D., Zhou, L.M., Ou, J., Jin, W., Lau, K.T., 2009. Strain monitoring of RC members strengthened with smart NSM FRP bars. Construction and Building Materials 23, 1698–1711.

Yan, X., Miller, B., Nanni, A., Bakis, C., 1999. Characterization of CFRP rods used as near surface mounted reinforcement, in: 8^{th} International Conference on Structural Faults and Repair – Edinburgh, Scotland.

Yun, Y., Wu, Y.F., Tang, W.C., 2008. Performance of FRP bonding systems under fatigue loading. Engineering Structures 30, 3129–3140.

Zureick, A., Bennett, R., Ellingwood, B., 2006. Statistical characterization of fiber-reinforced polymer composite material properties for structural design. Journal of Structural Engineering 132, 1320–1327.

APPENDIX A

FRPBonData website

The following figures present some of the main features included in the FRPBonData website. A full image of the website potential can only be obtained accessing it at www.frpbondata.civil.uminho.pt.

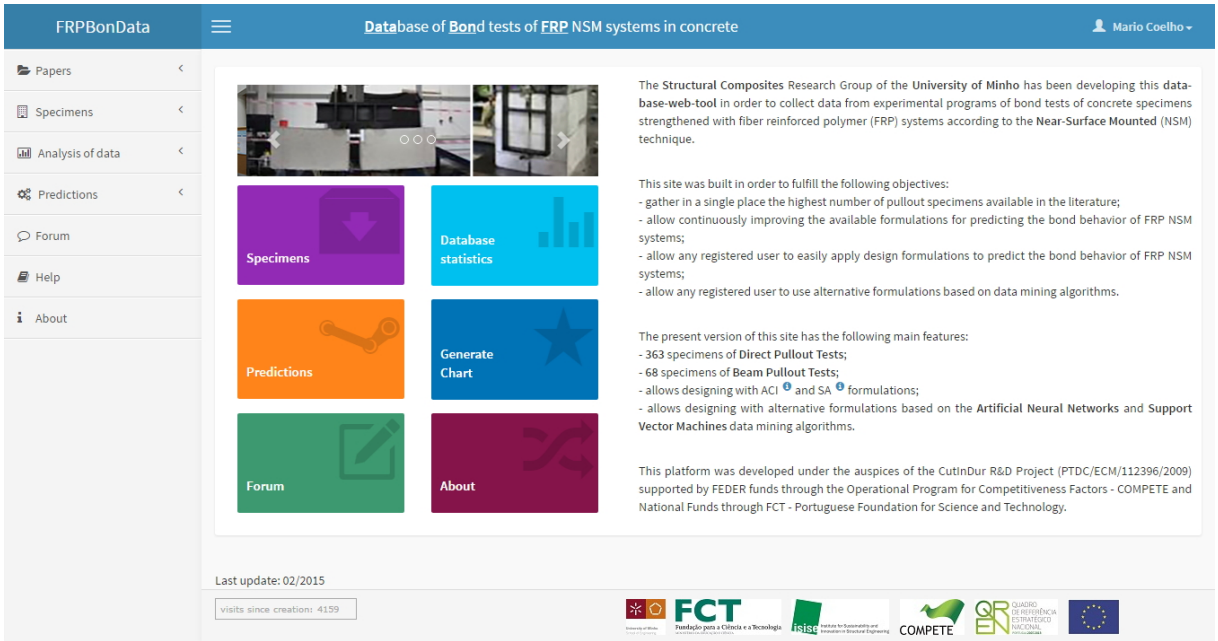

Figure A.1: FRPBonData website homepage.

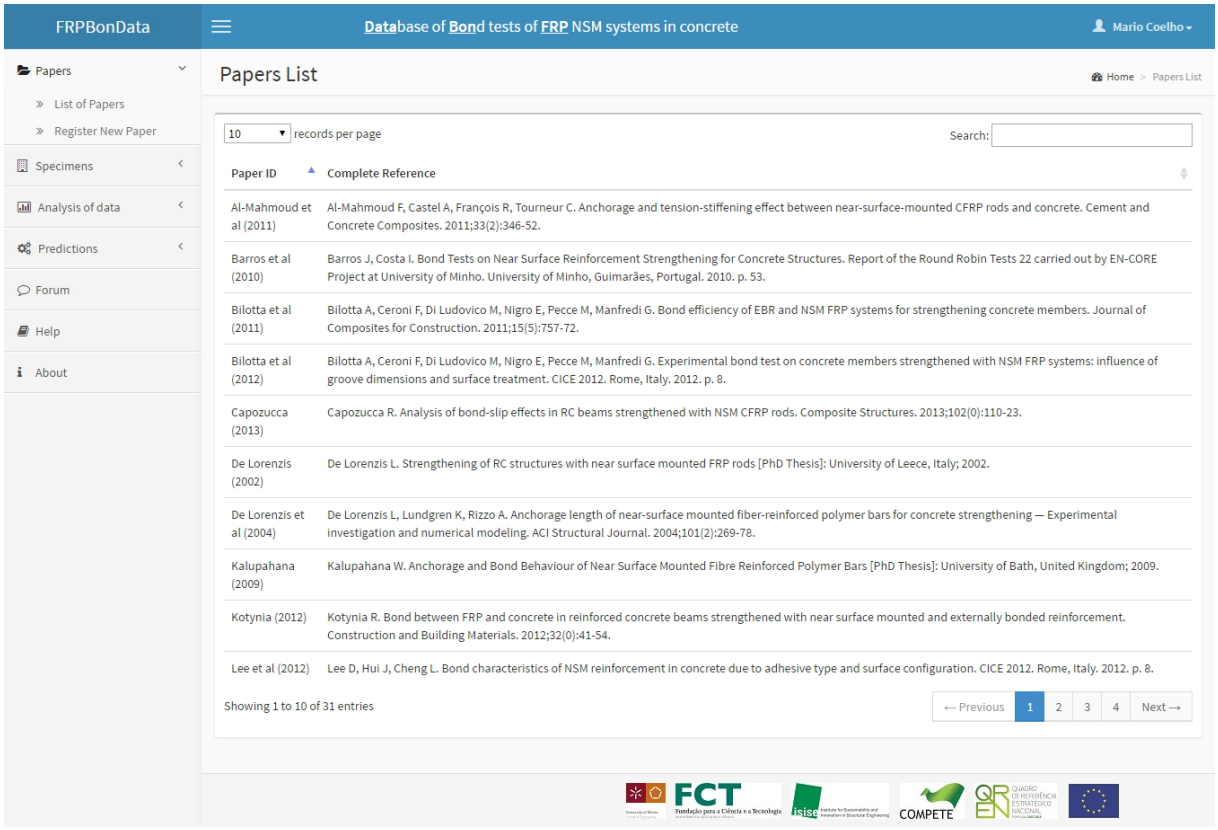

Figure A.2: FRPBonData website list of papers page.

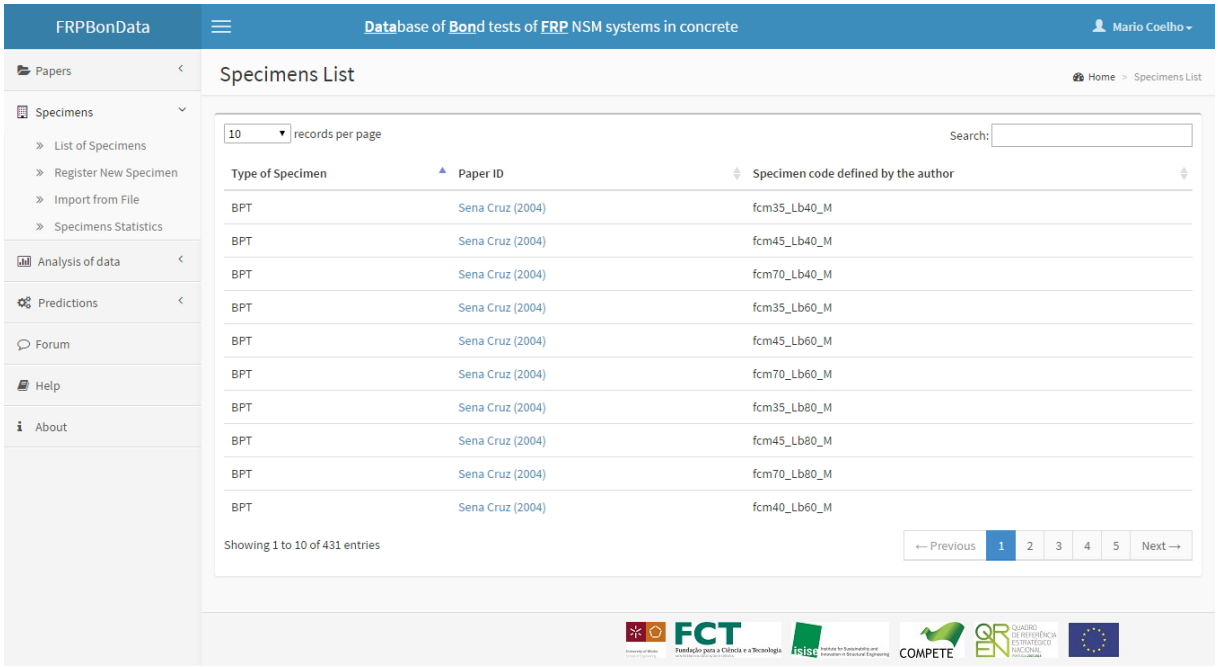

Figure A.3: FRPBonData website list of specimens page.

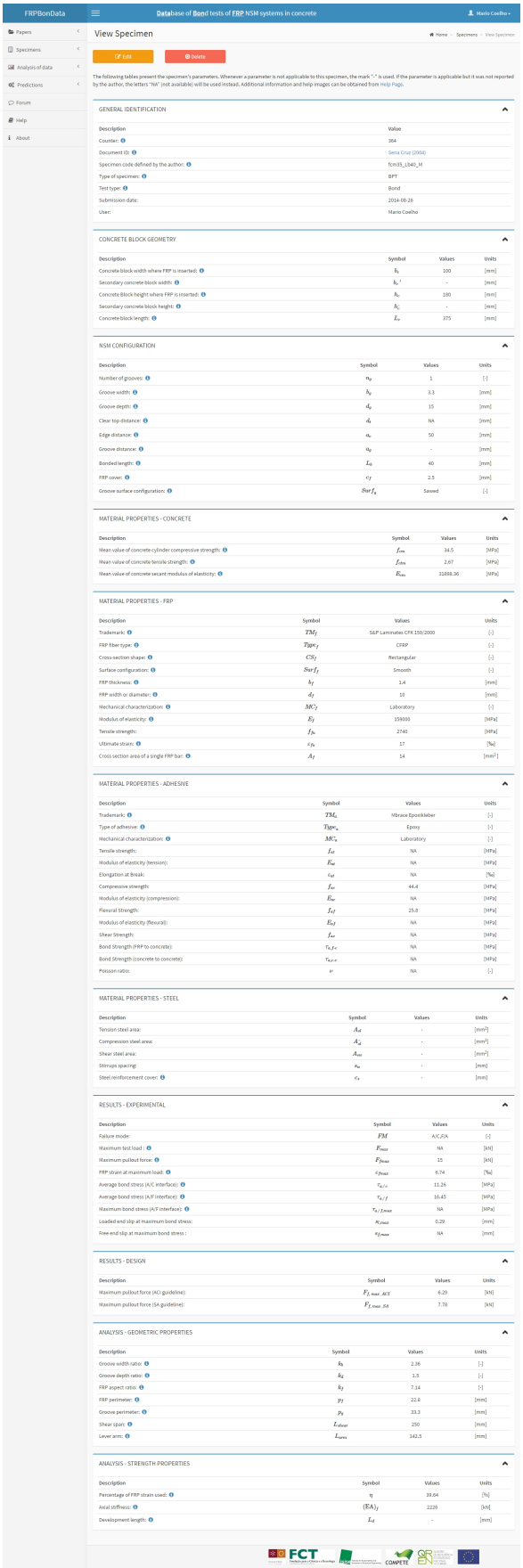

Figure A.4: FRPBonData website specimen details page (example).

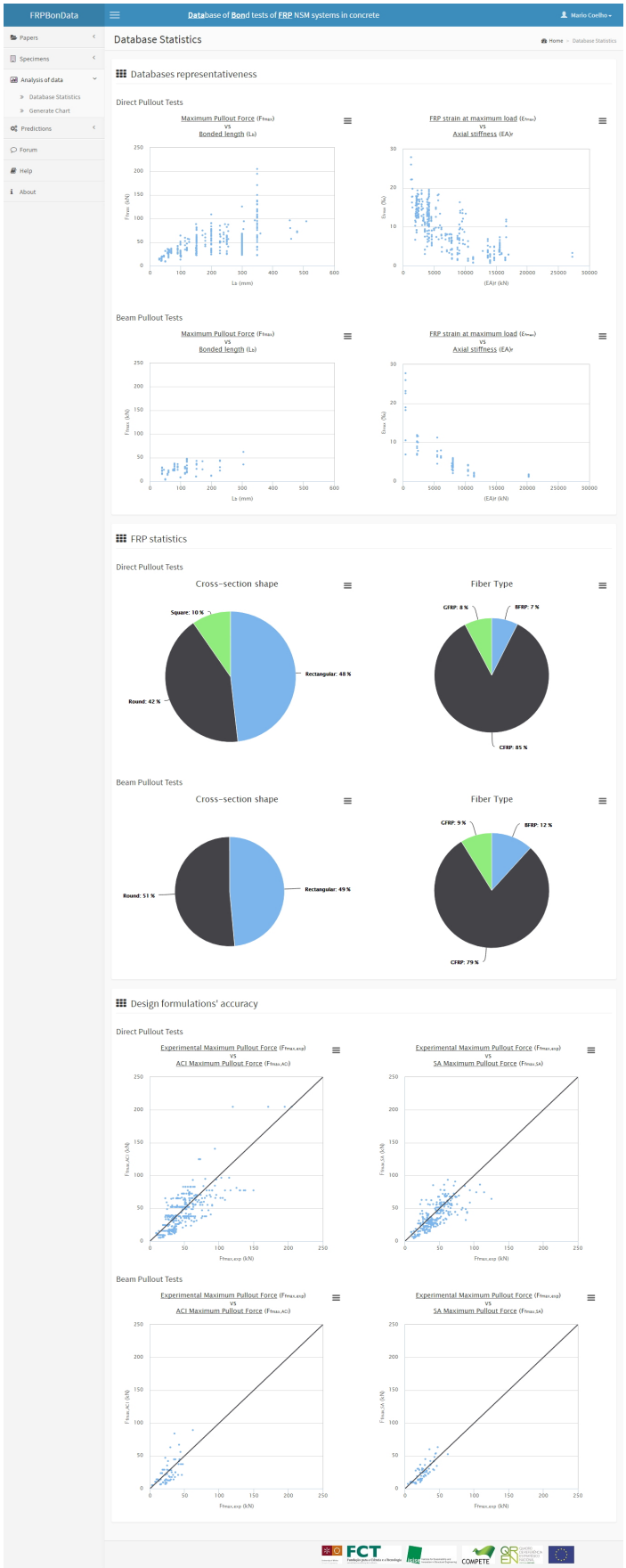

Figure A.5: FRPBonData website database predefined charts page.

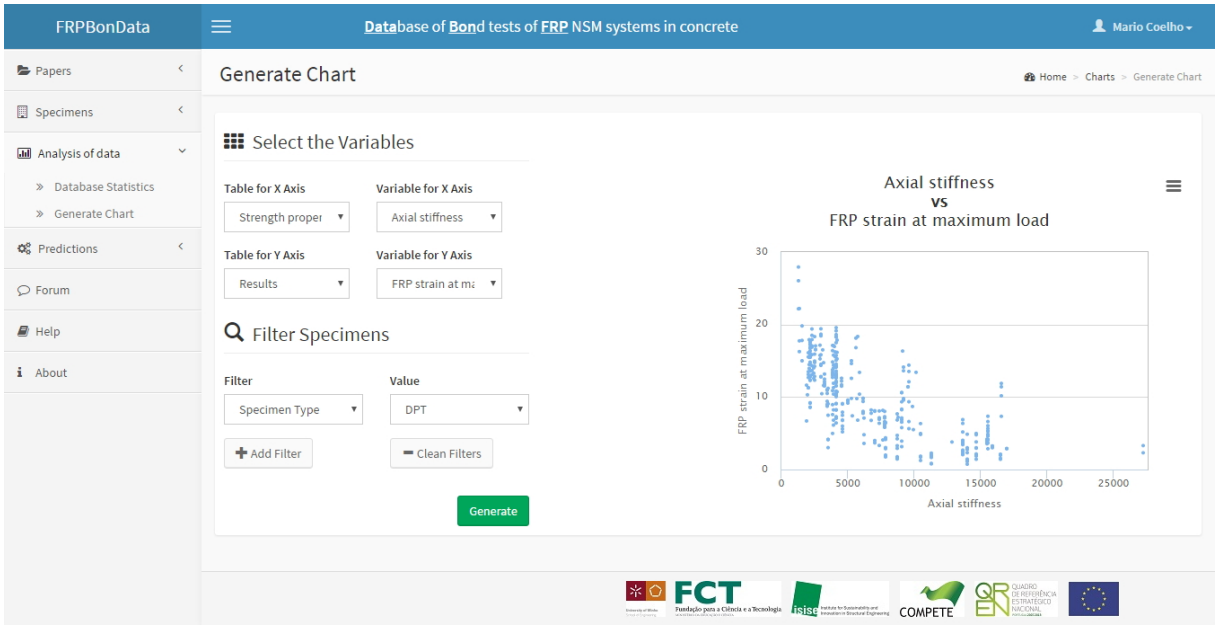

Figure A.6: FRPBonData website user defined charts page (example).

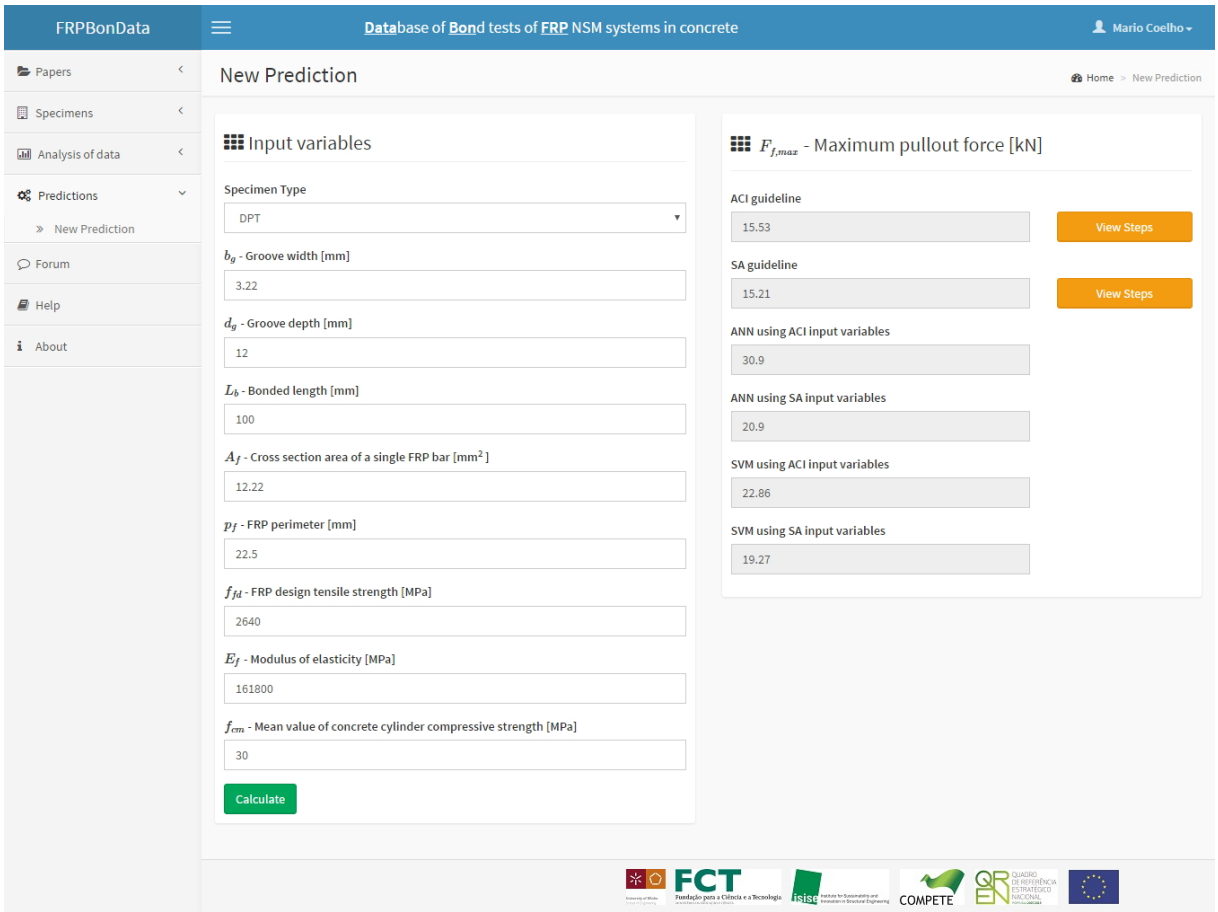

Figure A.7: FRPBonData website predictions page (example).

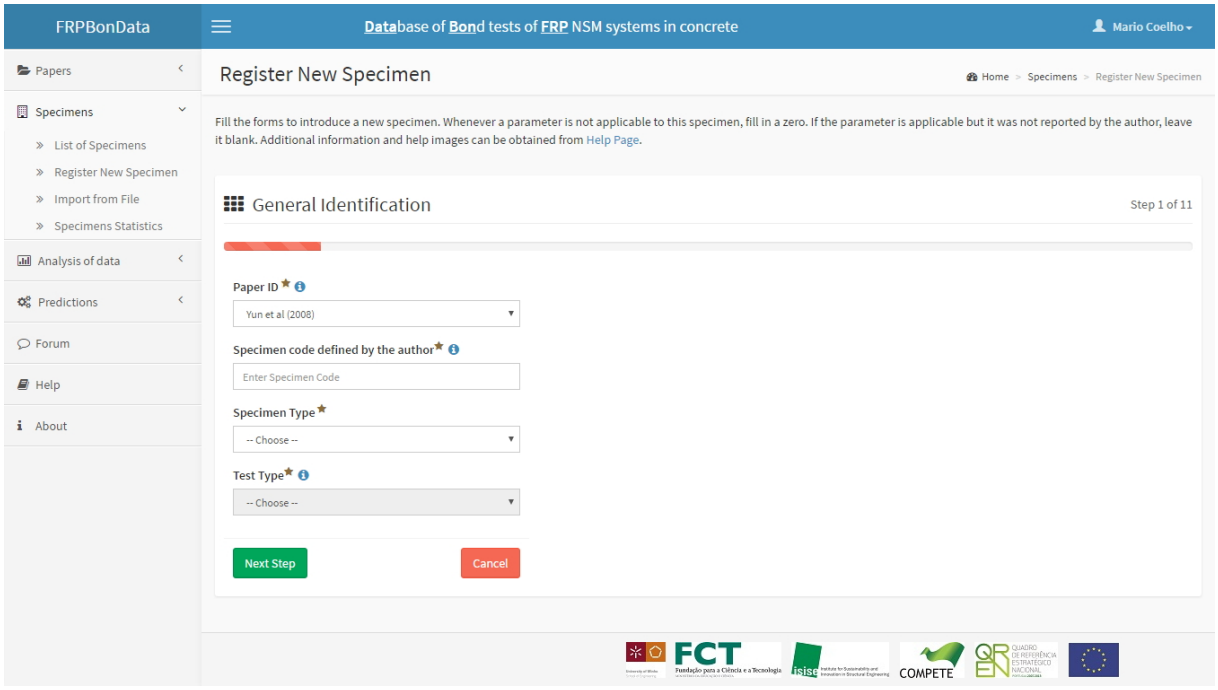

Figure A.8: FRPBonData website registering new specimens page.

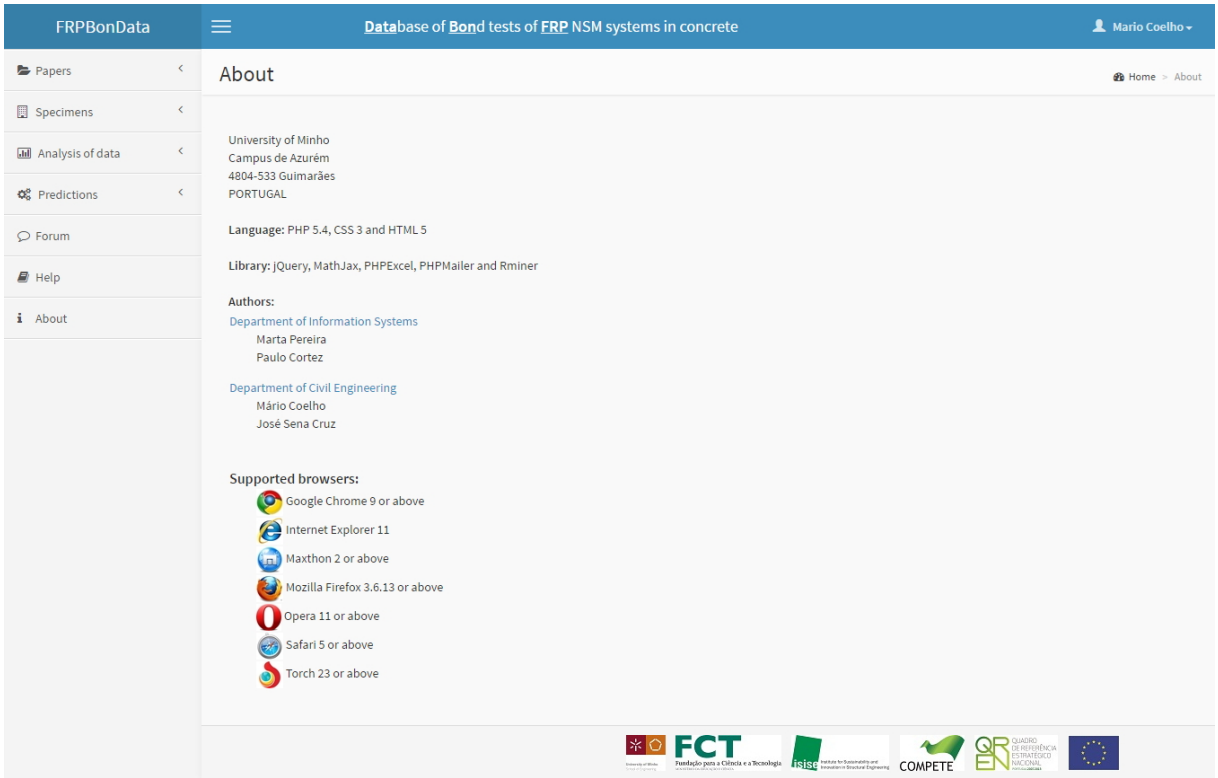

Figure A.9: FRPBonData website about page.

APPENDIX B

Interface constitutive model detailed formulation

The following sections detail the expressions used in the formulation of each one of the three modules composing the interface constitutive model implemented in this work.

The definition of all the entities used can be consulted in the symbols chapter.

B.1 Constitutive model II

$$f\left(\underline{\sigma}, \kappa\right) = f\left(\underline{\sigma}, \underline{\Phi}\right) = f\left(\sigma_1, c\right) = \sigma_1^2 - c^2 \tag{B.1}$$

$$\underline{\Phi}\left(\kappa\right) = \left[c\left(\kappa\right)\right] \tag{B.2}$$

$$\underline{n}\left(\underline{\sigma}, \kappa\right) = 2\sigma_1 \tag{B.3}$$

$$\underline{m}\left(\underline{\sigma}, \kappa\right) = \underline{n}\left(\underline{\sigma}, \kappa\right) = 2\sigma_1 \tag{B.4}$$

$$\Delta\kappa = \sigma_1 \Delta\lambda m_1 \tag{B.5}$$

B.2 Constitutive model I/II_2D

$$f\left(\underline{\sigma}, \kappa\right) = f\left(\underline{\sigma}, \underline{\Phi}\right) = \sigma_1^2 - \left(c - \sigma_2 \tan\phi\right)^2 + \left(c - \chi \tan\phi\right)^2 \tag{B.6}$$

$$\left[\underline{\Phi}\left(\kappa\right)\right] = \left[\chi\left(\kappa\right), c\left(\kappa\right), \tan\phi\left(\kappa\right)\right] \tag{B.7}$$

$$\underline{n} = \left(\underline{\sigma}, \kappa\right) = \begin{bmatrix} 2\sigma_1 \\ 2\tan\phi\left(c - \sigma_2 \tan\phi\right) \end{bmatrix} \tag{B.8}$$

$$\underline{m}\left(\underline{\sigma},\kappa\right)=\begin{cases}\begin{bmatrix}2\sigma_1\\2\tan\beta\left(c-\sigma_2\tan\phi\right)\end{bmatrix} & \text{if } \sigma_2\geq 0\\ \begin{bmatrix}2\sigma_1\\2\tan\beta\left(c-\sigma_2\tan\phi\right)\left(1+\frac{\sigma_2}{\sigma_{dil}}\right)\end{bmatrix} & \text{if } -\sigma_{dil}\leq\sigma_2<0\\ \begin{bmatrix}2\sigma_1\\0\end{bmatrix} & \text{if } \sigma_2<-\sigma_{dil}\end{cases} \tag{B.9}$$

$$\Delta\kappa=\begin{cases}\sigma_1\Delta\lambda m_1+\sigma_2\Delta\lambda m_2 \text{ if } \sigma_2\geq 0\\ \left(\sigma_1+\sigma_2\tan\phi\right)\Delta\lambda m_1 \text{ if } \sigma_2<0\end{cases} \tag{B.10}$$

B.3 Constitutive model I/II_3D

$$f\left(\underline{\sigma},\kappa\right)=f\left(\underline{\sigma},\underline{\Phi}\right)=-\left(c-\sigma_3\tan\phi\right)+\sqrt{\sigma_1^2+\sigma_2^2+\left(c-\chi\tan\phi\right)^2} \tag{B.11}$$

$$\underline{\Phi}\left(\kappa\right)=\left[\chi\left(\kappa\right),c\left(\kappa\right),\tan\phi\left(\kappa\right)\right] \tag{B.12}$$

$$\underline{n}\left(\underline{\sigma},\kappa\right)=\begin{bmatrix}\sigma_1\left(\sigma_1^2+\sigma_2^2+\left(c-\chi\tan\phi\right)^2\right)^{-\frac{1}{2}}\\ \sigma_2\left(\sigma_1^2+\sigma_2^2+\left(c-\chi\tan\phi\right)^2\right)^{-\frac{1}{2}}\\ \tan\phi\end{bmatrix} \tag{B.13}$$

$$g\left(\underline{\sigma},\kappa\right)=g\left(\underline{\sigma},\underline{\Psi}\right)=-\left(c_g-\sigma_3\tan\phi_g\right)+\sqrt{\sigma_1^2+\sigma_2^2+\left(c_g-\chi\tan\phi_g\right)^2} \tag{B.14}$$

$$\underline{\Psi}=\left[\chi\left(\kappa\right),c_g\left(\kappa\right),\tan\phi_g\left(\kappa\right)\right] \tag{B.15}$$

$$\underline{m}\left(\underline{\sigma},\underline{\Psi}\right)=\begin{bmatrix}\sigma_1\left(\sigma_1^2+\sigma_2^2+\left(c_g-\chi\tan\phi_g\right)^2\right)^{-\frac{1}{2}}\\ \sigma_2\left(\sigma_1^2+\sigma_2^2+\left(c_g-\chi\tan\phi_g\right)^2\right)^{-\frac{1}{2}}\\ \tan\phi_g\end{bmatrix} \tag{B.16}$$

$$\Delta\kappa=\begin{cases}\sigma_1\Delta\lambda m_1+\sigma_2\Delta\lambda m_2+\sigma_3\Delta\lambda m_3 \text{ if } \sigma_3\geq 0\\ \left(\sqrt{\sigma_1^2+\sigma_2^2}+\sigma_3\tan\phi\right)\sqrt{\left(\Delta\lambda m_1\right)^2+\left(\Delta\lambda m_2\right)^2} \text{ if } \sigma_3<0\end{cases} \tag{B.17}$$